

Customized Carbon Nanomaterials and MEMs Development for Neurochemical Detection

He Zhao

Cangzhou, Hebei, China

Bachelor of Science,

American University

Washington DC, United States, 2019

A Dissertation Presented to the Graduate Faculty of the University of Virginia in Candidacy for
the Degree of Doctor of Philosophy

Department of Chemistry

University of Virginia

2025

Abstract

Carbon fiber microelectrodes (CFMEs), with fast-scan cyclic voltammetry (FSCV), are commonly used for the real-time tracking of neurotransmitters *in vivo*. CFs can detect multiple electroactive analytes, such as dopamine, but they are limited in the trapping of analytes and the prevention of fouling and biofouling. This dissertation aims to overcome the limitations of CFs by investigating different carbon-based electrode sensors, including the growth of carbon nanomaterials and graphitization of polymer via rapid thermal processor (RTP) and laser, and their applications for *in vivo* recording of neurochemicals.

Chapter 1 covers the fundamental theories and recent developments of electrochemically neurochemical detection, nanofabrication methods, and laser-induced graphene with MEMs. Chapter 2 studies the surfaces of carbon nanospike-modified electrodes (CNSMEs). Rich surface defect sites and oxygen functional groups promote neurochemical adsorption and prevent fouling and biofouling. Chapter 3 explores the fabricated nanolayers of graphite from a commercial polymer, parylene. Induced graphite from parylene via rapid thermal processor (RTP) possesses good electrical conductivity and enables electrochemical detection of neurochemicals and *in vivo* tracking of dopamine and adenosine. Chapter 4 describes the method to graphitize parylene with the Nanoscribe laser, which is commonly used for the fabrication of 3D-printed structures. A single-channel Microelectromechanical systems (MEMs) chip was developed and combined with laser-induced graphene from parylene for dopamine detection. Finally, challenges and future directions using multiple-channel MEMs chips and nanofabrication techniques for electrode sensor fabrication are addressed in Chapter 5.

Overall, my dissertation focuses on various fabrication methods of carbon sensors and MEMs development for neurotransmitter detection. The fundamental studies indicate that rich defect sites and oxygen functional groups benefit the prevention of fouling and biofouling. This work may benefit the further investigation of multiple-channel MEMs, with various electrode nanomaterials, for the co-detection of neurotransmitters.

Table of Contents

Chapter 1

Introduction

1.1 Neurochemical Detection with Fast-Scan Cyclic Voltammetry

1.1.1 Neurochemical detection

1.1.2 Fast-scan cyclic voltammetry fundamentals

1.1.3 Neurochemical detection with carbon fiber microelectrodes

1.2 Fabrication of Carbon-Based Electrodes

1.2.1 Plasma-enhanced chemical vapor deposition

1.2.2 Chemical vapor deposition

1.2.3 Photolithography

1.2.4 Direct Laser Writing

1.2.5 Oxygen-plasma treatment

1.2.6 Surface chemical and surface structures

1.3 Laser-induced-graphene for MEMs development

1.3.1 Laser-induced-graphene originated from polyimide

1.3.2 MEMs development with laser-induced-graphene with parylene-N

1.4 Overview of Dissertation

1.5 References

Chapter 2

Carbon nanospikes have improved sensitivity and anti-fouling properties for adenosine, hydrogen peroxide, and histamine

2.1 Introduction

2.2 Experiment section

2.2.1 Construction of CNSMEs

2.2.2 Construction of CFMEs

2.2.3 Brain slice preparation

2.3 Results

2.3.1 Surface characterization

2.3.2 Background-current normalization

2.3.3 CNSMEs enhanced neurochemical adsorption

2.3.4 Histamine short-term and long-term fouling tests

2.3.5 Neurochemical detection in the brain slice

2.4 Discussion

2.5 Conclusions

2.6 References

Chapter 3

Pyrolyzed Parylene-N for *In Vivo* Electrochemical Detection of Neurotransmitters

3.1 Introduction

3.2 Experimental section

3.2.1 Construction of PPNMEs

3.2.2 Construction of CFMEs

3.3 Results

3.3.1 PN coating thickness measurements

3.3.2 Electric conductivity tests

3.3.3 Surface characterizations

3.3.4 PPNMEs promoted analyte adsorption

3.3.5 Serotonin short-term and long-term fouling tests

3.3.6 Stimulated dopamine and transient adenosine

3.4 Discussions

3.5 Conclusions

3.6 References

Chapter 4

Laser-Induced-Graphene Electrodes from Parylene-N: Use of Nanoscribe 3D Printer to Fabricate Carbon Electrodes for Neurotransmitters

4.1 Introduction

4.2 Experimental section

4.2.1 Construction LIG-PNMEs

4.2.2 Construction of MEMs

4.2.3 Construction of CFMEs

4.3 Results

4.3.1 PN thickness measurement

4.3.2 PN light-adsorption test

4.3.3 Surface characteristics

4.3.4 Conductivity test

4.3.5 Electrochemical Detection

4.3.6 Single-channel MEMs development

4.4 Conclusion

4.5 References

Chapter 5

5.1 Contribution to the Dissertation to the Field

5.1.1 Customizable Micro/nano Carbon Sensors

5.1.2 Single-channel MEMs with LIG-PN

5.2 Challenges and Future Directions

5.2.1 Synaptic recording with 3D-Printing

5.2.2 Shrunk 3D-Printing with Oxygen Plasma

5.2.3 Co-detection of Dopamine and Glutamate

5.3 Final Remarks

5.4 References

Appendix

List of publications of this dissertation

Chapter 1

Introduction

1.1 Neurochemical Detection with Fast-Scan Cyclic Voltammetry

1.1.1 Neurochemical Detection

Information is transferred between neurons through a process known as neurotransmission. Neurotransmitters are generated by neurons and then released via exocytosis.¹ However, when the neurons are degraded, a lack of neurotransmitters could lead to cognitive dysfunctions, such as Parkinson's disease and Alzheimer's disease.^{2,3} Released neurotransmitter concentrations in the brain are about 0.1 – 1 μM and neurochemicals are rapidly cleared through cell reuptake.^{4,5} Therefore, it is an extreme challenge to monitor neurochemicals. It is necessary to have techniques that can fast, sensitively, and selectively monitor the released neurotransmitters in the extracellular space.

Two categories of neurochemicals can be electrochemically detected, low- and high-potential analytes. Low-potential analytes can be oxidized within a potential range, of -0.4 V to 1.3 V, such as dopamine (DA) and serotonin (5-HT).⁶⁻⁸ Dopamine, a catecholamine, serves as a neurotransmitter involved in the regulation of human body movement and cognitive behavior. The formal dopamine potential is + 0.2 V vs. Ag/AgCl. When the applied voltage exceeds dopamine formal potential, two-electron and two-proton transfers will happen to dopamine and oxidize to dopamine-o-quinone, which can be reduced back to dopamine when applying negative potential. Typically, the switching potential of the triangular waveform is much higher than the dopamine formal potential, but no polymerization usually takes place for dopamine. A higher potential range, -0.4 V to 1.45 V, is needed to induce the oxidation of high-potential analytes, such as adenosine (AD) and histamine (HA).^{9,10} Adenosine is a derivative of adenosine triphosphate (ATP), which provides energy for body movement. Adenosine is involved in the regulation of vasodilation and sleep and the synthesis of AMP, ADP, and ATP.¹¹⁻¹³ Adenosine undergoes three oxidation processes although the tertiary oxidation peak is

usually not visible during electrochemical detection. The primary and secondary oxidation potentials are about 1.40 V and 1.0 V.¹⁴

Serotonin and histamine are involved in mood and depression regulation and brain and immune system regulations. Serotonin undergoes a single oxidation step, with an oxidation potential similar to dopamine. Histamine undergoes two oxidation processes, located at 0.8 V and 1.4 V, taking place on histamine molecules.^{10,15,16} Both of these two neurochemicals are polymerized during electrochemical detection. Polymerized molecules can attach to the electrode surface and block active sites. Therefore, detection sensitivity will correspondingly decrease.^{8,14,17} In long-term animal model testing, biofouling originates from protein covering and can dramatically reduce the electrochemical performance.¹⁸

Rapid adenosine release occurs in the prefrontal cortex, striatum, caudate-putamen, and hippocampus and can regulate neurotransmission or blood flow.¹⁹ There are two types of rapid adenosine release observed in mice, spontaneous release and mechanical stimulation. A₁ receptors modulate transient adenosine release, which is more frequent in the caudate putamen, than in the prefrontal cortex.¹² When adenosine is spontaneously released in the brain, the event frequencies in the striatum and hippocampus are higher than the ones in the prefrontal cortex. However, the magnitude of released adenosine concentration per event is greater in the striatum compared to the prefrontal cortex.¹³ In general, the concentration induced by mechanical stimulation and the frequency of spontaneous release in the hippocampus is high and the cortex behaves adversely to the hippocampus. Mechanically stimulated adenosine release is typically higher than spontaneous release, and additional adenosine receptors can be activated to provide neuroprotection.¹⁹

Carbon electrodes are commonly used for *in vivo* neurotransmitter detection. On the electrode surface, neurochemicals will undergo realignment and adsorb to the electrode surface.²⁰ To enhance the detection sensitivity, promoting analyte adsorption is essential. Also, carbon sensors should be designed to minimize fouling and biofouling issues, ensuring long-

term and sensitive *in vivo* tracking. Fig.1.1 illustrates methods to fabricate carbon sensors, including plasma-enhanced chemical vapor deposition (PECVD), pyrolysis through rapid thermal processing (RTP), and laser-induced-graphitization.^{21,22}

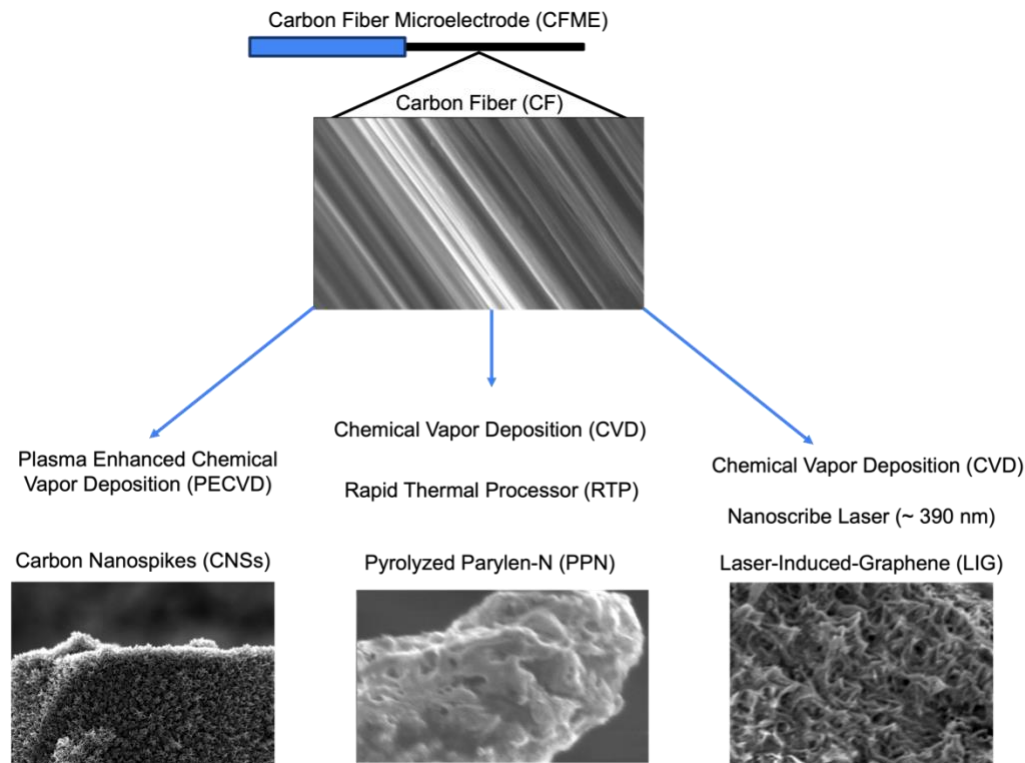


Figure 1.1 Fabrication methods for carbon electrode sensors.^{21,22} - Published by *Analytical and Bioanalytical Chemistry* and *ACS Electrochemistry*.

1.1.2 Fast-scan cyclic voltammetry fundamentals

Fast-scan cyclic voltammetry (FSCV) is an electrochemical method that originates from traditional cyclic voltammetry (CV) and provides a high temporal resolution.^{1,23,24} FSCV commonly uses a scan rate of 400 V/s to monitor the real-time release of neurotransmitters. A key feature distinguishing FSCV from traditional CV is background current subtraction, due to its higher scan rate.²³ On the electrode surface, positively and negatively charged ions are separately aligned, forming an electric double-layer. Background current magnitude is proportional to the active surface area. In phosphate-buffered saline (PBS) buffer, commonly used for FSCV detection, there is a solution resistance (R_s) caused by the resistance to ion

movement. The potential applied on the electrode surface increases with the application of scan rate (v) according to $E = vt$. The solution resistance (R_s) and electrode surface capacitance (C_d) make up an R_sC_d circuit, where the potential follows the charge equation, $vt = R_s(dq/dt) + q/C_d$, with the time. The equation, $i = vC_d [1 - \exp(-t/R_sC_d)]$ when $q = 0$, $t = 0$, is used to calculate the current change.²⁰ The involvement of two factors, large scan rate, and surface area, contributes to the large magnitude of background current, which originates from the electrical double layer.²⁰ The induced Faradaic current from neurochemical oxidation is much less than the background current, meaning the Faradaic current is often difficult to detect when combined with the background current. To obtain a CV graph of neurotransmitters, background-current subtraction is usually performed.

There are some differences between traditional CV and FSCV. Firstly, the analyte oxidation potential detected in FSCV is usually higher than in CV, as FSCV uses a higher scan rate. Therefore, within the same period, FSCV provides a higher potential to oxidize all accumulated neurotransmitters on the electrode surface and generate a Gaussian oxidation peak. FSCV possesses a higher ΔE_p , the difference between oxidation and reduction potentials, than CV.²⁵ In traditional CV, neurotransmitters are not fully consumed after switching potential, as diffusion brings more analyte to the surface of the electrode. Therefore, neurochemical oxidation and reduction peaks are duck-shaped.²⁰ Thirdly, the ratio of reduction and oxidation peaks is 1.0 in traditional CV as there is enough time for oxidized and reduced neurotransmitters to be detected on the electrode surface. In FSCV, for neurochemicals that can be oxidized and reduced, the ratio of reduction and oxidation peaks is less than 1.0 as the affinity of oxidized analytes is usually lower than reduced neurotransmitters as much less time is allowed for them to be adsorbed on the electrode surface.

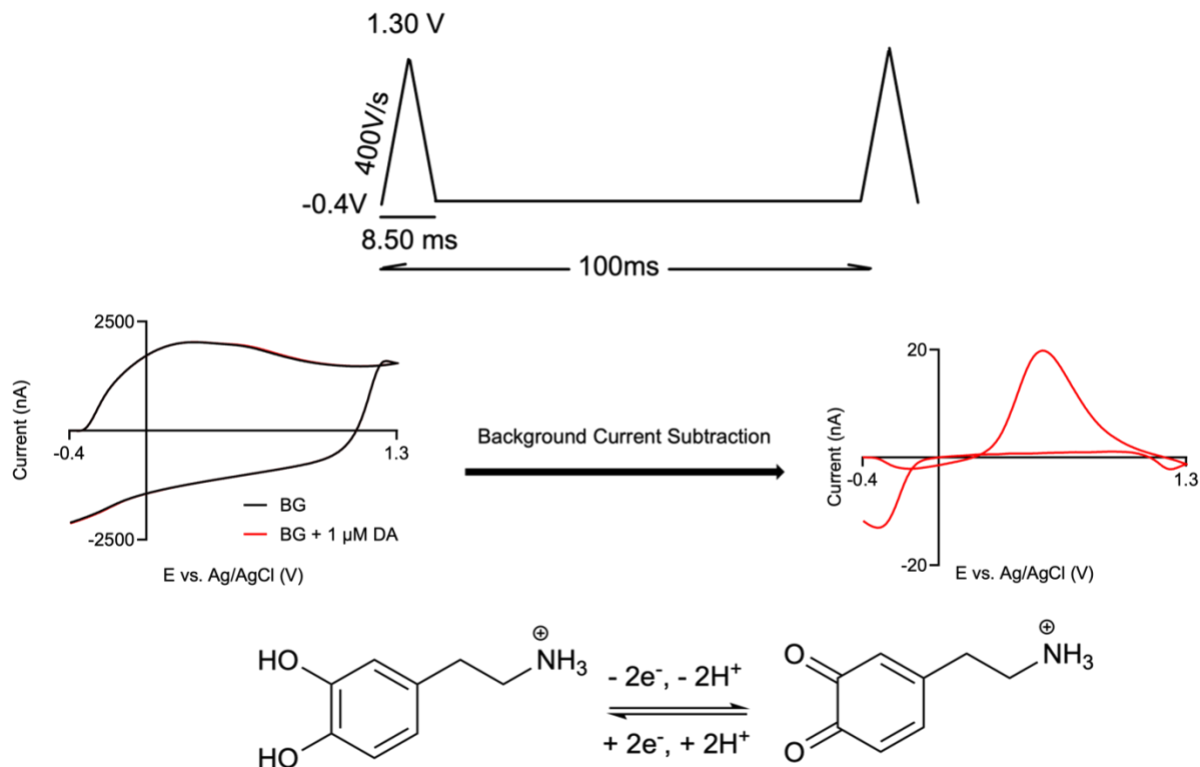


Figure 1.2 FSCV detection of DA (A) Dopamine waveform at 10 Hz. Potential ranges from -0.4 V to 1.30 V. (B) CV graph of background and 1 μM DA and CV graph of 1 μM background-subtracted DA (C) DA oxidation mechanism

Two common types of triangular waveforms are used in electrochemical detection: (1) the dopamine waveform (-0.4 V to 1.3 V) and (2) the adenosine (AD) waveform (-0.4 V to 1.45 V). The dopamine waveform, at 10 Hz, is shown in Fig. 1.2. When holding the potential at -0.4 V, analytes start accumulating on the electrode surface via adsorption in 91.5 ms as most of them are positively charged at physiological pH, 7.40. Each electrochemical scan takes 8.50 ms to induce the oxidation and reduction of neurochemicals. Since the scan rate of FSCV is much higher than CV, the background current, which originates from double-layer charging, is significantly larger than the Faradaic current when oxidizing analytes. Consequently, dopamine Faradaic current is hard to distinguish when combined with the background current. To get a visible adenosine CV graph, background subtraction is necessary, as shown in Fig. 1.2. The dopamine waveform can continuously activate the electrode surface by breaking chemical bonds and provide a more reactive surface, which helps resist fouling and biofouling.^{18,26,27}

1.1.3 Neurochemical detection with carbon fiber microelectrodes

Carbon fibers (CFs) are made from polyacrylonitrile (PAN) by spinning the polymer into a fiber.^{6,28,29} CFs are usually shaped into needle electrodes with a vertical puller and the length of CF is controlled around 10-50 μm for electrochemical detection. CFs exhibit good electrochemical performance and are used for neurochemical tracking in animal testing, such as mice, rats, and fruit flies (*Drosophila*). The diameter of CFs, approximately about 7 μm , allows them to prevent major damage to the brain tissue.³⁰⁻³² There are rich defect sites on the CF surface, and they help partially trap the analytes. Additionally, CFs also possess more oxygen functional groups compared to glassy carbon. These functional groups promote the adsorption of neurotransmitters- particularly catecholamines, which are positively charged at a physiological pH, of 7.40.^{25,33-35} Due to the electrostatic force between oxygen functional groups and catecholamines, the detection sensitivities can be enhanced.^{27,36} However, a limitation of CFs is that their smooth surface does not favor the trapping of analytes.³⁷ Besides, the CF surface cannot resist the polymer and protein attachments due to π - π stacking.^{14,18}

CFs can be modified by physically depositing various types of carbon nanomaterial onto the surface via dip-coating and drop-casting. One example of such a modification is the deposition of nanodiamonds (NDs). ND-modified CFMEs present anti-fouling properties and enhanced detection sensitivities.^{34,38} However, these methods cannot guarantee uniform and complete deposition of ND, limiting the improvement in electrochemical performance. Other carbon nanomaterials have also been explored for electrochemical applications to figure out their unique properties. For example, carbon nanotubes (CNTs) with higher surface roughness are particularly effective in trapping neurochemicals, leading to a 1:1 ratio of oxidation and reduction currents – a phenomenon known as the thin-layer effect.³⁹⁻⁴¹ Carbon nanomaterials, such as carbon nanospikes (CNSs), can be deposited on etched metal wires via chemical vapor

deposition (CVD) to reduce the electrode size substantially and guarantee a uniformly and completely coated surface, making them more suitable for animal studies.³³

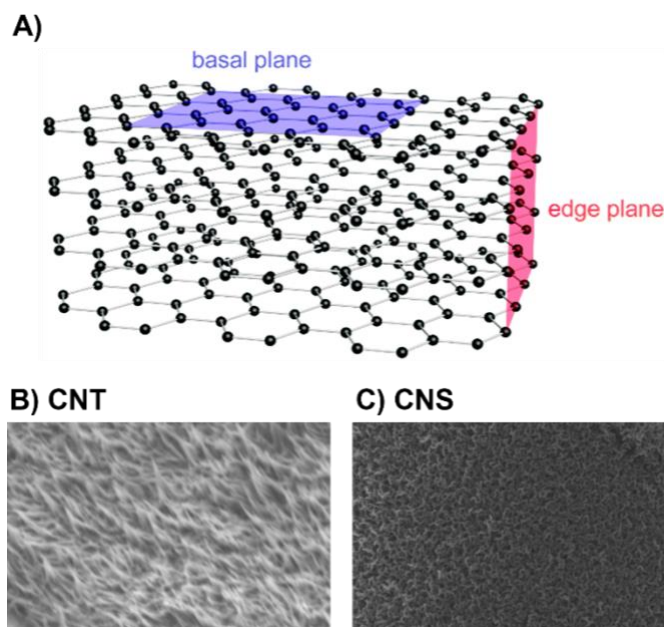


Figure 1.3. (A) Basal and edge planes of graphitic materials (B) Carbon nanotube (CNT) (C) Carbon nanospike (CNS)

1.2 Fabrication and Characterization of Carbon-Based Electrodes

1.2.1 Plasma-enhanced chemical vapor deposition

PECVD technique can be used for coating development, such as the temperature-sensitive substrates, as it allows for deposition at temperatures ranging from 400-2000 °C down to room temperature.⁴²⁻⁴⁴ Electric fields are commonly used to generate plasma – reactive species are created by breaking the bonds in organic gaseous molecules with direct current between two electrodes. Unlike thermal CVD, PECVD operates at lower temperatures for nanomaterial fabrication, such as carbon nanodiamonds and carbon nanotubes (CNTs). PECVD also offers a catalyst-free method for carbon nanomaterial growth, such as carbon nanospikes, which are sp^2 -hybridized and defect-rich.^{25,33} In the synthesis of carbon nanospikes, metal wires aligned on a stainless-steel stage are used as cathodes. 100 sccm ammonia and 80 sccm acetylene at 6 Torr pressure and 650 °C are injected for 6 min into a custom-built DC

PECVD chamber. 500 mA, 0.23 kW, and 480-550 V are set as the DC plasma discharge parameters.

1.2.2 Chemical vapor deposition

Chemical vapor deposition (CVD) encompasses many types, including low-pressure, ultra-high vacuum, and microwave-assisted CVD.^{38,45-47} CVD is widely used for carbon material synthesis and utilizes gaseous or vapor precursors that react at the substrate interface form a deposited layer. CVD employs bottom-up or top-down approaches to synthesize nanomaterials, like CNTs.⁴⁸⁻⁵⁰ This method is known for its ability to produce uniform and high-purity products. Polymer coating, such as parylene, can be deposited on various substrates with the CVD technique. The parylene coating occurs in a parylene coater. Under vacuum conditions, the coater heats [2, 2] paracyclophane powder, the precursor, to 150 °C for obtaining gaseous dimer. The temperature is then increased to 650 °C to break dimers into a monomer state, parylene. Gaseous monomers will deposit on the substrate when the temperature is reduced to room temperature, 25 °C. The application of gaseous monomer can guarantee the uniformity of parylene coating.⁵¹⁻⁵³ Various amounts of precursor can be loaded in the parylene chamber to achieve coating ranges from nanoscale to microscale. Niobium wires can be used as the substrate for parylene coating and further annealed with RTP for carbonization and fabrication of carbon sensors.

Poly(p-xylene), which is known as parylene, is a benzene-rich polymer and possesses chemical inertness, flexibility, and transparency. Parylene is frequently used to coat electronics to insulate their surfaces.^{54,55} Previously, parylene was also applied to 3D-printed structures for nanoelectrode fabrication. Parylene coating has been compared to PDMS, glass, and optically clear virgin polystyrene for the analysis of protein adsorption and cell adhesion.⁵⁶ Generally, parylene resists cell adhesion, but after the treatment of oxygen plasma, microscale features and patterns can be created on the thin film. The modified parylene is suitable for cellular co-culture and tissue barrier models with its biocompatibility.⁵⁷ Parylene's flexibility also makes it a

promising material for the microfabrication of flexible devices. There are several parylene derivatives – N, C, D, VT4, HT, and AF4.⁵⁸ Among these, parylene-N and C are the most commonly used for microelectronic and medical coating applications.

Parylene Type	Mass (g)	Deposited Thickness (nm)	Thickness after Hot plate (nm)	Thickness after Pyrolysis μ (nm)
N	1	286	117	86
N	6	1800	650	191
N	12	3500	750	489

Table 1. Parylene-N coating thicknesses with different loaded amounts.

RTP is used to anneal parylene coatings and induce pyrolysis through various temperature profiles. Different annealing recipes can be applied, such as (1) 350 °C in an air atmosphere for 10 min (2) 600 °C in an argon atmosphere at 9 Torr for 15 min (3) 950 °C in an argon atmosphere at 1 Torr for 15 min.⁵⁹ Heating parylene at 350 °C in an air atmosphere results in the coating shrinkage and the incorporation of oxygen into the parylene structure while breaking polymer bonds in the meantime. The subsequent RTP steps will continuously shrink parylene thicknesses, as shown in Table 1, and ultimately pyrolyze polymer coating step.^{55,60} Pyrolyzed parylene on Nb wires can then be fabricated into microelectrodes for electrochemical detection.

1.2.3 Photolithography

Photolithography (optical lithography) is a microfabrication technique that creates a pattern, designed on an optical mask, onto a substrate coated with a photoresist. There are two main types of photoresists – positive- and negative-photoresist. They react differently when reacting with light: (1) positive photoresist does not crosslink with the contact of light (2) negative photoresist will get crosslinked when light covers the coating.^{61,62} One commonly used negative photoresist is SU-8, and the process of C-MEMs patterning is illustrated in Fig. 1.4. SU-8 can be uniformly spin-coated on the substrate, usually Si chips. When the optical mask is

aligned with the coated substrate, UV light is applied to crosslink exposed photoresist. Unexposed photoresist remains soluble and the developer will rinse the residue away.⁶²⁻⁶⁴ Crosslinked photoresist will be kept on the substrate and can be used for further processing, including pyrolysis. Therefore, the fabrication of integrated chips and microfluidic chips can be finished with photolithography. However, the diffraction limit of light is the controlling factor for photolithography. Another limitation of photolithography is the shadow effect when utilizing a curved surface.^{62,63}

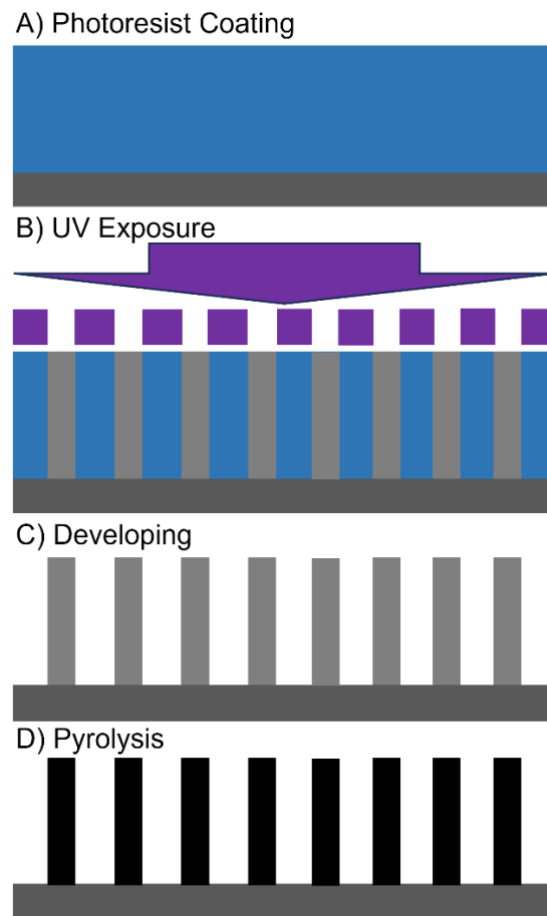


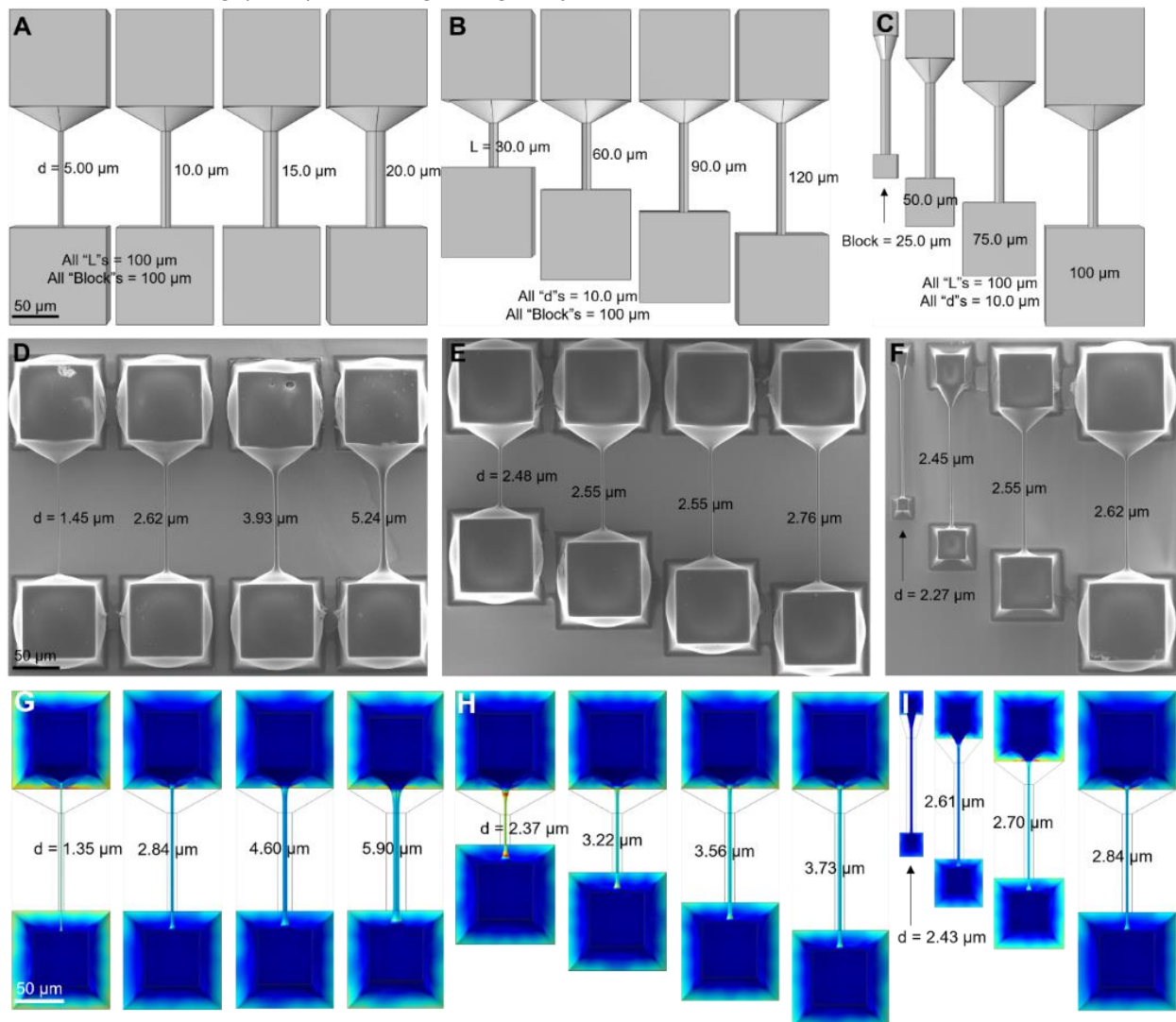
Figure 1.4. Illustration of C-MEMs for 3D carbon array structure fabrication

1.2.4 Direct Laser Writing

Different complicated structures, which are designed with COMSOL software, can be fabricated with 3D printing techniques. Traditional 3D printing is not suited for the tracking of

neurotransmitters released in the brain as the resolution is too large (usually in the tens of microns to millimeters). Oversized structures can cause significant damage to the brain tissue. In contrast, the 3D nanoprinting technique of direct laser writing can achieve a much higher resolution, down to 100 nm.⁶⁵ Another advantage of 3D nanoprinting is that metal wires can be utilized as substrates to develop implantable sensors.⁶⁶

This technique allows precise polymerization of IP-DIP or IP-S photoresist.⁶⁷⁻⁶⁹ When the photoresist is crosslinked using a focused laser, the printed structure remains intact on the substrate. The residual, unpolymerized photoresist is then removed by rinsing with the SU-8 developer. Following the printing process, 3D structures are subjected to pyrolysis through rapid thermal processing (RTP), resulting in a glassy-carbon-like surface.⁷⁰ The development of



microelectrodes and nanoelectrodes using 3D nanoprinting has been successful, with most structures maintaining their original form. However, the limitation of these electrodes is that the electrode tip is usually blunt and short. Further designs and optimizations, which are shown in Figure 1.5, are needed for the fabrication of nanoelectrodes with long and thin tips for neurochemical detection in small organisms, like *Drosophila* (fruit fly). Figure 1.5 shows designed structures with the application of pulling force generated on the bridge between two printed blocks when annealing with RTP. This optimization test provides a set of parameters for the generation of carbon nanoelectrodes that possess long and thin tips in the nanoscale and successfully induce dopamine detection in the ventral nerve cord (VNC) of fruit flies.⁷⁰

Figure 1.5 Block and bridge structures printed on a silicon wafer with varying bridge diameters, bridge lengths, and block sizes.⁷⁰ – Published by *Angewandte Chemie*

1.2.5 Oxygen-plasma treatment

Oxygen plasma treatment achieves the introduction of oxygen functional groups onto the surface of carbon-based materials when exposing them to a charged oxygen as flow.^{71,72} These functional groups, particularly oxygen-related defect sites, promote the adsorption of neurotransmitters, thereby enhancing detection sensitivities. Additionally, increasing the density of states (DOS) can facilitate electron transfer on the electrode surface, which is observed as a reduction in the oxidation-reduction potential difference, ΔE_p .^{25,73} Various carbon nanomaterials have been treated with oxygen plasma to enhance neurochemical detection. The oxygen functional groups also prevent the attachment of analyte polymer and protein in the brain tissue, which are known as fouling and biofouling, respectively. Instead of adding oxygen functional groups, oxygen plasma can also be applied for etching oxygen functional groups away from the material surface. For example, carbon nanodiamond is a sp^3 -rich carbon material that is usually utilized for neutron acceleration.^{34,38} However, the application of carbon nanodiamonds in electrochemical detection is not appropriate as the conductivity of this nanomaterial is not as

great as glassy carbon, which is sp^2 -rich. To recover the conductivity, carbon nanodiamond is etched by oxygen plasma to remove a layer of oxygen functional groups to expose sp^2 carbon.

Furthermore, oxygen plasma treatment is effective for cleaning contamination from material surfaces. For example, oxygen plasma can clean Nb wires for the construction of 3D-printed structures with surface etching. Therefore, this etching technique can be applied to shrink the size of carbon materials. Previously, we designed a method for the generation of 3D-printed nanoelectrodes with the application of pulling force.⁷⁰ However, this method requires a complicated structure is time-consuming, and the overall electrode size is still about 800 nm. To reach the nano size for neurochemical recording in the cell or synapse, oxygen plasma can be used to etch 3D printed structures to guarantee nanoelectrode generation while retaining long and thin tips.

1.2.6 Surface functional groups and surface structures

Graphitic materials consist of basal and edge planes, where sp^2 -carbon and sp^3 -carbon atoms are respectively located. The basal planes are known for their good electrical conductivity, which is beneficial during FSCV detection. Multiple layers of graphene are included in the carbon materials. This structural information can be characterized by Raman spectra, which is shown as D ($\sim 1340\text{ cm}^{-1}$) and G ($\sim 1580\text{ cm}^{-1}$) bands.⁷⁴ With peak calculations of 2D peak ($\sim 2800\text{ cm}^{-1}$) area, graphene layers can be quantified as well. Defect sites on the electrode surface are important for improving electrochemical detection by facilitating neurochemical adsorption and increasing surface roughness. The roughness can be visualized by atomic force microscopy (AFM) with a nanoneedle to scan the surface.⁷⁵ The surface elemental composition of carbon materials can be quantified by X-ray photoelectron spectroscopy (XPS) and energy dispersive spectroscopy (EDS).^{76,77} XPS is especially useful for identifying the functional groups to which carbon atoms are bonded and can provide quantitative data on the abundance of each group.

Carbon nanomaterials, such as carbon nanospikes, carbon nanotubes, and carbon nanodiamonds, possess higher roughness and oxygen functional groups on the surface. These characteristics benefit the prevention of fouling and biofouling. Furthermore, the reduced number of basal planes decreases the available sites for neurotransmitter polymers, limiting π - π stacking.^{14,25} The rich defect sites on nanomaterials also enhance their hydrophilicity, minimizing protein attachment due to the hydrophobic effect, which is commonly present on basal planes.¹⁴

1.3 Laser-induced-graphene for MEMs development

1.3.1 Laser-induced-graphene originated from polyimide

The synthesis of graphene-based nanomaterials typically requires high temperatures. However, polyimide (PI), a commercially available polymer, can be converted into graphene using laser treatment, a process known as laser-induced graphene (LIG).⁷⁸⁻⁸¹ There are two primary forms of LIG produced from PI: (1) PI sheet for flexible sensor or supercapacitor and (2) spin coating of Kapton PI on the substrate. Carbonization of PI using a CO₂ infrared laser with pulsed laser irradiation, results in the transformation of sp³-carbon to sp²-carbon atoms via photothermal conversion.^{82,83} LIG has excellent electrical conductivity and can be used for in-plane supercapacitors and energy-storage devices. The Tour Group has explored various CO₂ infrared laser powers and their corresponding Raman spectra to optimize the graphene properties.⁸⁴⁻⁸⁶ To guarantee the best conductivity, a laser power of 4.8 W, which yields the highest G/D ratio has been selected for microsupercapacitor development.

1.3.2 MEMs development with laser-induced-graphene with parylene-N

LIG from PN possesses good electric conductivity and electrochemical performance. LIG-PN is expected to be coupled with MEMs devices to perform neurochemical tracking. Silicon-based materials, like single-crystal silicon, silicon dioxide, and silicon nitride, are commonly used for the fabrication of MEMs devices and systems.^{54,55} The development of

MEMs with silicon-based materials is usually time-consuming and costly. To reduce these costs, paper-based MEMs, such as piezoresistive force sensors, have been developed.^{87–89} Micro-electromechanical systems (MEMs) have been widely used for supercapacitors, where LIG enhances performance.^{67,90,91}

A well-established processing sequence combines wafer-level photolithographic patterning and thin film deposition and is utilized to fabricate LIG-MEMs sensors. On 4'' diameter fused silica wafers; metal electrode patterns are created. At 250 °C, the first processing step is to dehydrate silica wafers on the hotplate for 30 min and this step is followed by 2 min oxygen plasma treatment. Dehydrated silica wafers are coated with a double layer of resistor by using spin coating at 3000 RMP. Then 180 °C is applied on the coated silica wafers for 2 min when placed on the hotplate. Using 3000 RMP, the second layer of resistor, SPR 955CM-0.5 will be coated on the silica wafers by spin coating and then baked at 90 °C for 90 s. The contact aligner with the mask containing metal electrode patterns is used to treat wafers coated with double-layer resistors. The wafers are developed in CD26 developer for 60 s, rinsed with deionized water, and then dried with filtered nitrogen. The chamber of a DC sputter deposition tool is used to achieve the coating of 100 nm Nb on the wafers. Finally, deposited wafers are metal lift-off in acetone and soaked in N-methylpyrrolidone for removing remained LOR3A resistor. After rinsing and drying the wafers, they are diced into chips for further treatment. Diced MEMs chips are chemically vapor deposited with parylene-N. Coated MEMs chips are heated with microhotplate at 350 °C for 10 min to change the light adsorption property for successful adsorption of the Nanoscribe laser for carbonization. The scanning pattern can be various and designed with COMSOL software. For the successful development of LIG-MEMs and dopamine recording, shown in Fig. 1.6, Raman spectra of LIG originating from PN should also present the highest D/G ratio to ensure the electrical conductivity of LIG-PN is appropriate for FSCV detection of neurotransmitters. LIG-PN is applied to the carbon detection area of dual-channel biosensor design to achieve co-detection of dopamine and glutamate.

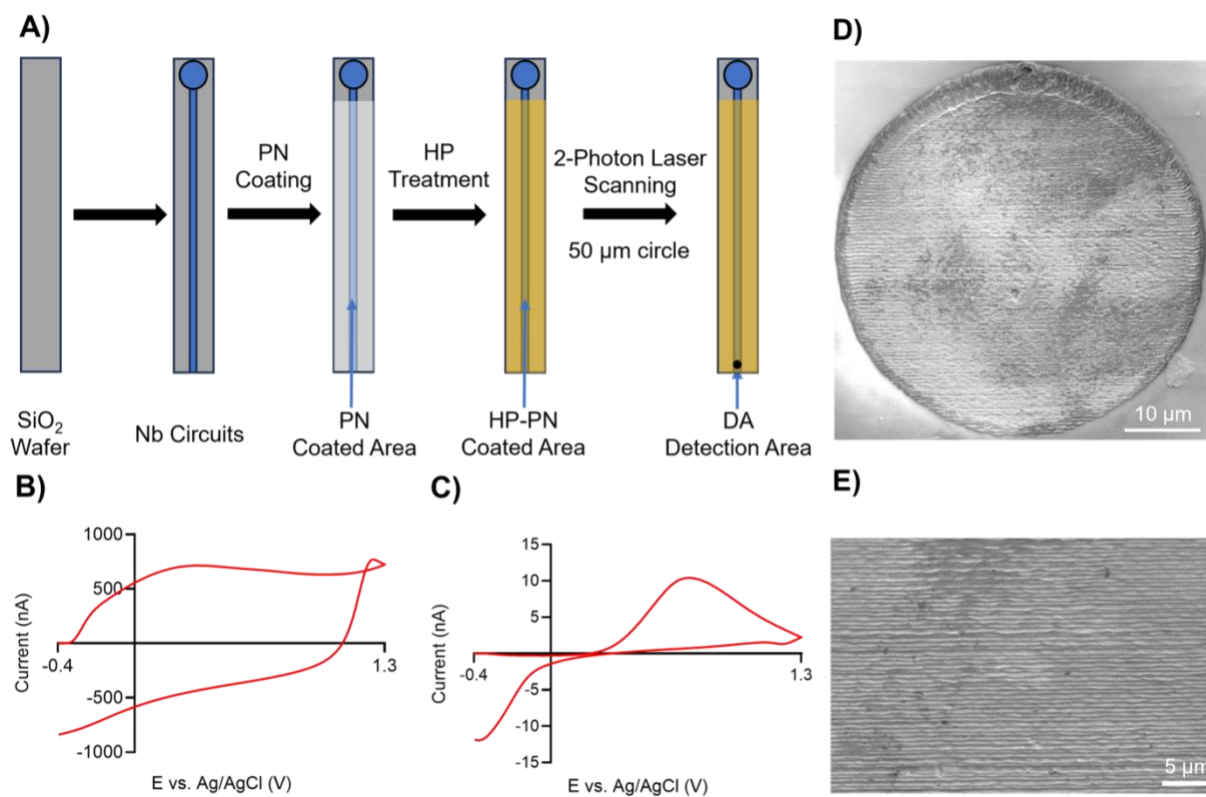


Figure 1.6. Illustration of fabrication process of single-channel LIG-MEMs

1.4 Overview of Dissertation

Carbon electrodes, which are pivotal for neurotransmitter recording, can be customized with different designs. These techniques include the deposition of carbon nanomaterials, pyrolyzed nanoscale polymer, and laser-induced nanoscale pyrolyzed polymer. This dissertation explores techniques to fabricate carbon micro/nano electrode sensors, focusing on their behavior in electrochemical detection and potential for *in vivo* tracking. This research also examines their impact on sensing neurotransmitters, with a specific focus on preventing neurochemical fouling and biofouling from brain tissue or protein attachment. Beyond traditional carbon-fiber (CF) sensors, customizable electrode fabrication methods are considered for their potential to enhance sensor performance.

Chapter 2 presents studies of the surfaces of electrodes that promote the adsorption of high-potential analytes, adenosine (AD), histamine (HA), and hydrogen peroxide (H_2O_2), while also resisting fouling and biofouling. Carbon nanospike modified electrodes (CNSMEs) and carbon fiber microelectrodes (CFMEs) were systemically compared. CNS electrodes, with higher surface roughness and richer defect sites, exhibited enhanced electrostatic interactions and surface trapping, which increased the adsorption of analytes. Additionally, the oxygen functional groups and reduced basal planes contribute to a more hydrophilic surface, minimizing fouling from polymerized neurochemicals and brain tissue or protein attachment. Therefore, CNSMEs are useful for preventing fouling and biofouling and are appropriately applied for stable and long-term *in vivo* neurochemical tracking in the future.

Chapter 3 examines the feasibility of using pyrolyzed parylene-N, a polymer commonly used for insulating electronics, in conjunction with fast-scan cyclic voltammetry (FSCV) for neurotransmitter sensing. Various PN coating thicknesses are explored, with shrinkage induced by a microhotplate at 350 °C and further enhanced by a rapid thermal processor (RTP) at 600-950 °C in an argon atmosphere. The RTP process pyrolyzed PN, which possesses good electric

conductivity. The resulting pyrolyzed parylene-N modified electrodes have a nanolayer of pyrolyzed graphite, 194 nm. PPNMEs were applied for dopamine (DA), serotonin (5-HT), and adenosine (AD) characterizations with FSCV and presented superior sensitivity compared to CFMEs. PPNMEs can resist fouling because of their rich defect sites and oxygen functional groups. Modified electrodes successfully sensed stimulated DA and spontaneous AD. This new type of fabricated electrodes can be further tested for other neurochemicals or neuropeptides.

Chapter 4 explores the synthesis of laser-induced graphene (LIG) from parylene-N using a commercially available Nanoscribe laser, which is typically employed in 3D printing. In addition, microelectromechanical systems (MEMs) devices were developed to integrate with LIG. In Chapter 4, the Nanoscribe laser successfully graphitized PN, creating LIG that exhibited extremely high surface roughness, which induced significant trapping of analytes. This trapping effect led to a frequency-independent reduction-to-oxidation current ratio of 1 for dopamine detection. The biocompatibility of LIG-PN enables its use *in vivo*, where it successfully tracked dopamine release. The LIG-PN was incorporated into a single-channel MEMs chip and achieved dopamine sensing. There could be a multiple-channel MEMs chip developed and then utilizing LIG to induce co-detection of neurotransmitters. Chapter 5 illustrates the contribution to the field and the remaining challenges for electrochemical synaptic recording with 3D-printed nanoelectrodes.

In summary, the dissertation utilizes multiple nanofabrication approaches to generate customizable sensors that enhance the electrochemical detection of neurochemicals. It also addresses the challenges and future directions in the application of carbon-based sensors for neurotransmitter detection and co-detection.

1.5 References

- (1) *Psychoanalytical Electrochemistry: Dopamine and Behavior*.
<https://doi.org/10.1021/ac031421c>.
- (2) Holmes, S. E.; Honhar, P.; Tinaz, S.; Naganawa, M.; Hilmer, A. T.; Gallezot, J.-D.; Dias, M.; Yang, Y.; Toyonaga, T.; Esterlis, I.; Mecca, A.; Van Dyck, C.; Henry, S.; Ropchan, J.; Nabulsi, N.; Louis, E. D.; Comley, R.; Finnema, S. J.; Carson, R. E.; Matuskey, D. Synaptic Loss and Its Association with Symptom Severity in Parkinson's Disease. *Npj Park. Dis.* **2024**, *10* (1), 1–9.
<https://doi.org/10.1038/s41531-024-00655-9>.
- (3) Tzioras, M.; McGeachan, R. I.; Durrant, C. S.; Spires-Jones, T. L. Synaptic Degeneration in Alzheimer Disease. *Nat. Rev. Neurol.* **2023**, *19* (1), 19–38. <https://doi.org/10.1038/s41582-022-00749-z>.
- (4) Robinson, D. L.; Phillips, P. E. M.; Budygin, E. A.; Trafton, B. J.; Garris, P. A.; Wightman, R. M. Sub-Second Changes in Accumbal Dopamine during Sexual Behavior in Male Rats. *NeuroReport* **2001**, *12* (11), 2549.
- (5) Robinson, D. L.; Venton, B. J.; Heien, M. L. A. V.; Wightman, R. M. Detecting Subsecond Dopamine Release with Fast-Scan Cyclic Voltammetry in Vivo. *Clin. Chem.* **2003**, *49* (10), 1763–1773. <https://doi.org/10.1373/49.10.1763>.
- (6) Bath, B. D.; Michael, D. J.; Trafton, B. J.; Joseph, J. D.; Runnels, P. L.; Wightman, R. M. Subsecond Adsorption and Desorption of Dopamine at Carbon-Fiber Microelectrodes. *Anal. Chem.* **2000**, *72* (24), 5994–6002. <https://doi.org/10.1021/ac000849y>.
- (7) Jacobs, C. B.; Ivanov, I. N.; Nguyen, M. D.; Zestos, A. G.; Venton, B. J. High Temporal Resolution Measurements of Dopamine with Carbon Nanotube Yarn Microelectrodes. *Anal. Chem.* **2014**, *86* (12), 5721–5727. <https://doi.org/10.1021/ac404050t>.
- (8) Dunham, K. E.; Venton, B. J. Improving Serotonin Fast-Scan Cyclic Voltammetry Detection: New Waveforms to Reduce Electrode Fouling. *Analyst* **2020**, *145* (22), 7437–7446. <https://doi.org/10.1039/D0AN01406K>.
- (9) Basheer, R.; Strecker, R. E.; Thakkar, M. M.; McCarley, R. W. Adenosine and Sleep–Wake Regulation. *Prog. Neurobiol.* **2004**, *73* (6), 379–396.
<https://doi.org/10.1016/j.pneurobio.2004.06.004>.
- (10) Sarada, B. V.; Rao, T. N.; Tryk, D. A.; Fujishima, A. Electrochemical Oxidation of Histamine and Serotonin at Highly Boron-Doped Diamond Electrodes. *Anal. Chem.* **2000**, *72* (7), 1632–1638. <https://doi.org/10.1021/ac9908748>.
- (11) Bjorness, T. E.; Greene, R. W. Adenosine and Sleep. *Curr. Neuropharmacol.* **2009**, *7* (3), 238–245. <https://doi.org/10.2174/157015909789152182>.
- (12) Nguyen, M. D.; Lee, S. T.; Ross, A. E.; Ryals, M.; Choudhry, V. I.; Venton, B. J. Characterization of Spontaneous, Transient Adenosine Release in the Caudate-Putamen and Prefrontal Cortex. *PLoS ONE* **2014**, *9* (1), e87165.
<https://doi.org/10.1371/journal.pone.0087165>.

- (13) Nguyen, M. D.; Venton, B. J. Fast-Scan Cyclic Voltammetry for the Characterization of Rapid Adenosine Release. *Comput. Struct. Biotechnol. J.* **2015**, *13*, 47–54. <https://doi.org/10.1016/j.csbj.2014.12.006>.
- (14) Zhao, H.; Shrestha, K.; Hensley, D. K.; Venton, B. J. Carbon Nanospikes Have Improved Sensitivity and Antifouling Properties for Adenosine, Hydrogen Peroxide, and Histamine. *Anal. Bioanal. Chem.* **2023**, *415* (24), 6039–6050. <https://doi.org/10.1007/s00216-023-04875-5>.
- (15) Khot, G.; Shirtcliffe, N.; Celikel, T. *Simultaneous Detection of Dopamine and Serotonin with Carbon-Based Electrodes*; preprint; Biochemistry, 2021. <https://doi.org/10.1101/2021.08.31.458352>.
- (16) Puthongkham, P.; Lee, S. T.; Venton, B. J. Mechanism of Histamine Oxidation and Electropolymerization at Carbon Electrodes. *Anal. Chem.* **2019**, *91* (13), 8366–8373. <https://doi.org/10.1021/acs.analchem.9b01178>.
- (17) Liu, J.; Cao, Y. An Electrochemical Sensor Based on an Anti-Fouling Membrane for the Determination of Histamine in Fish Samples. *Anal. Methods* **2021**, *13* (5), 685–694. <https://doi.org/10.1039/D0AY01901A>.
- (18) Weese, M. E.; Krevh, R. A.; Li, Y.; Alvarez, N. T.; Ross, A. E. Defect Sites Modulate Fouling Resistance on Carbon-Nanotube Fiber Electrodes. *ACS Sens.* **2019**, *4* (4), 1001–1007. <https://doi.org/10.1021/acssensors.9b00161>.
- (19) Wang, Y.; Venton, B. J. Comparison of Spontaneous and Mechanically-Stimulated Adenosine Release in Mice. *Neurochem. Int.* **2019**, *124*, 46–50. <https://doi.org/10.1016/j.neuint.2018.12.007>.
- (20) Bard, A. J.; Faulkner, L. R. *Electrochemical Methods: Fundamentals and Applications*, 2nd ed.; Wiley: New York, 2001.
- (21) Zhao, H.; Markow, O.; Olaitan, G.; Donarski, E. D.; Lester, K. C.; Lavrik, N. V.; Venton, B. J. Pyrolyzed Parylene-N for in Vivo Electrochemical Detection of Neurotransmitters. *ACS Electrochem.* **2025**. <https://doi.org/10.1021/acselectrochem.4c00180>.
- (22) Zhao, H.; Shrestha, K.; Hensley, D. K.; Venton, B. J. Carbon Nanospikes Have Improved Sensitivity and Antifouling Properties for Adenosine, Hydrogen Peroxide, and Histamine. *Anal. Bioanal. Chem.* **2023**, *415* (24), 6039–6050. <https://doi.org/10.1007/s00216-023-04875-5>.
- (23) Robinson, D. L.; Hermans, A.; Seipel, A. T.; Wightman, R. M. Monitoring Rapid Chemical Communication in the Brain. *Chem. Rev.* **2008**, *108* (7), 2554–2584. <https://doi.org/10.1021/cr068081q>.
- (24) Roberts, J. G.; Sombers, L. A. Fast Scan Cyclic Voltammetry: Chemical Sensing in the Brain and Beyond. *Anal. Chem.* **2018**, *90* (1), 490–504. <https://doi.org/10.1021/acs.analchem.7b04732>.

- (25) Cao, Q.; Hensley, D. K.; Lavrik, N. V.; Venton, B. J. Carbon Nanospikes Have Better Electrochemical Properties than Carbon Nanotubes Due to Greater Surface Roughness and Defect Sites. *Carbon* **2019**, *155*, 250–257. <https://doi.org/10.1016/j.carbon.2019.08.064>.
- (26) *Fundamentals of fast-scan cyclic voltammetry for dopamine detection - Analyst (RSC Publishing) DOI:10.1039/C9AN01586H*.
<https://pubs.rsc.org/en/content/articlehtml/2020/an/c9an01586h> (accessed 2022-09-18).
- (27) Cao, Q.; Lucktong, J.; Shao, Z.; Chang, Y.; Venton, B. J. Electrochemical Treatment in KOH Renews and Activates Carbon Fiber Microelectrode Surfaces. *Anal. Bioanal. Chem.* **2021**, *413* (27), 6737–6746. <https://doi.org/10.1007/s00216-021-03539-6>.
- (28) Huffman, M. L.; Venton, B. J. Carbon-Fiber Microelectrodes for in Vivo Applications. *The Analyst* **2009**, *134* (1), 18–24. <https://doi.org/10.1039/B807563H>.
- (29) Frank, E.; Hermanutz, F.; Buchmeiser, M. R. Carbon Fibers: Precursors, Manufacturing, and Properties. *Macromol. Mater. Eng.* **2012**, *297* (6), 493–501.
<https://doi.org/10.1002/mame.201100406>.
- (30) Privman, E.; Venton, B. J. Comparison of Dopamine Kinetics in the Larval *Drosophila* Ventral Nerve Cord and Protocerebrum with Improved Optogenetic Stimulation. *J. Neurochem.* **2015**, *135* (4), 695–704. <https://doi.org/10.1111/jnc.13286>.
- (31) Shin, M.; Copeland, J. M.; Venton, B. J. Real-Time Measurement of Stimulated Dopamine Release in Compartments of the Adult *Drosophila Melanogaster* Mushroom Body. *bioRxiv* June 29, 2020, p 2020.06.29.177675. <https://doi.org/10.1101/2020.06.29.177675>.
- (32) Cao, Q.; Shin, M.; Lavrik, N. V.; Venton, B. J. 3D-Printed Carbon Nanoelectrodes for In Vivo Neurotransmitter Sensing. *Nano Lett.* **2020**, *20* (9), 6831–6836.
<https://doi.org/10.1021/acs.nanolett.0c02844>.
- (33) G. Zestos, A.; Yang, C.; B. Jacobs, C.; Hensley, D.; Jill Venton, B. Carbon Nanospikes Grown on Metal Wires as Microelectrode Sensors for Dopamine. *Analyst* **2015**, *140* (21), 7283–7292. <https://doi.org/10.1039/C5AN01467K>.
- (34) Puthongkham, P.; Venton, B. J. Nanodiamond Coating Improves the Sensitivity and Antifouling Properties of Carbon Fiber Microelectrodes. *ACS Sens.* **2019**, *4* (9), 2403–2411.
<https://doi.org/10.1021/acssensors.9b00994>.
- (35) Puthongkham, P.; Yang, C.; Venton, B. J. Carbon Nanohorn-Modified Carbon Fiber Microelectrodes for Dopamine Detection. *Electroanalysis* **2018**, *30* (6), 1073–1081.
<https://doi.org/10.1002/elan.201700667>.
- (36) Hanser, S. M.; Shao, Z.; Zhao, H.; Venton, B. J. Electrochemical Treatment in KOH Improves Carbon Nanomaterial Performance to Multiple Neurochemicals. *The Analyst* **2024**, *149* (2), 457–466. <https://doi.org/10.1039/D3AN01710A>.
- (37) Shao, Z.; Puthongkham, P.; Hu, K.; Jia, R.; Mirkin, M. V.; Venton, B. J. Thin Layer Cell Behavior of CNT Yarn and Cavity Carbon Nanopipette Electrodes: Effect on Catecholamine

Detection. *Electrochimica Acta* **2020**, *361*, 137032.
<https://doi.org/10.1016/j.electacta.2020.137032>.

- (38) Shao, Z.; Wilson, L.; Chang, Y.; Venton, B. J. MPCVD-Grown Nanodiamond Microelectrodes with Oxygen Plasma Activation for Neurochemical Applications. *ACS Sens.* **2022**, *7* (10), 3192–3200. <https://doi.org/10.1021/acssensors.2c01803>.
- (39) Alvarez, N. T.; Buschbeck, E.; Miller, S.; Le, A. D.; Gupta, V. K.; Ruhunage, C.; Vilinsky, I.; Ma, Y. Carbon Nanotube Fibers for Neural Recording and Stimulation. *ACS Appl. Bio Mater.* **2020**, *3* (9), 6478–6487. <https://doi.org/10.1021/acsabm.0c00861>.
- (40) Avouris, P.; Appenzeller, J.; Martel, R.; Wind, S. J. Carbon Nanotube Electronics. *Proc. IEEE* **2003**, *91* (11), 1772–1784. <https://doi.org/10.1109/JPROC.2003.818338>.
- (41) Zestos, A. G.; Venton, B. J. (Invited) Carbon Nanotube-Based Microelectrodes for Enhanced Neurochemical Detection. *ECS Trans.* **2017**, *80* (10), 1497–1509. <https://doi.org/10.1149/08010.1497ecst>.
- (42) Bo, Z.; Yang, Y.; Chen, J.; Yu, K.; Yan, J.; Cen, K. Plasma-Enhanced Chemical Vapor Deposition Synthesis of Vertically Oriented Graphene Nanosheets. *Nanoscale* **2013**, *5* (12), 5180. <https://doi.org/10.1039/c3nr33449j>.
- (43) Lucovsky, G.; Tsu, D. V. Plasma Enhanced Chemical Vapor Deposition: Differences between Direct and Remote Plasma Excitation. *J. Vac. Sci. Technol. Vac. Surf. Films* **1987**, *5* (4), 2231–2238. <https://doi.org/10.1116/1.574963>.
- (44) Yi, K.; Liu, D.; Chen, X.; Yang, J.; Wei, D.; Liu, Y.; Wei, D. Plasma-Enhanced Chemical Vapor Deposition of Two-Dimensional Materials for Applications. *Acc. Chem. Res.* **2021**, *54* (4), 1011–1022. <https://doi.org/10.1021/acs.accounts.0c00757>.
- (45) Aljumaily, M. M.; Alsaadi, M. A.; Das, R.; Hamid, S. B. A.; Hashim, N. A.; AlOmar, M. K.; Alayan, H. M.; Novikov, M.; Alsalhy, Q. F.; Hashim, M. A. Optimization of the Synthesis of Superhydrophobic Carbon Nanomaterials by Chemical Vapor Deposition. *Sci. Rep.* **2018**, *8* (1), 2778. <https://doi.org/10.1038/s41598-018-21051-3>.
- (46) He, C. N.; Zhao, N. Q.; Shi, C. S.; Song, S. Z. Fabrication of Carbon Nanomaterials by Chemical Vapor Deposition. *J. Alloys Compd.* **2009**, *484* (1), 6–11. <https://doi.org/10.1016/j.jallcom.2009.04.088>.
- (47) Manawi, Y. M.; Ihsanullah; Samara, A.; Al-Ansari, T.; Atieh, M. A. A Review of Carbon Nanomaterials' Synthesis via the Chemical Vapor Deposition (CVD) Method. *Materials* **2018**, *11* (5), 822. <https://doi.org/10.3390/ma11050822>.
- (48) Sinnott, S. B.; Andrews, R.; Qian, D.; Rao, A. M.; Mao, Z.; Dickey, E. C.; Derbyshire, F. Model of Carbon Nanotube Growth through Chemical Vapor Deposition. *Chem. Phys. Lett.* **1999**, *315* (1–2), 25–30. [https://doi.org/10.1016/S0009-2614\(99\)01216-6](https://doi.org/10.1016/S0009-2614(99)01216-6).

- (49) Nessim, G. D. Properties, Synthesis, and Growth Mechanisms of Carbon Nanotubes with Special Focus on Thermal Chemical Vapor Deposition. *Nanoscale* **2010**, 2 (8), 1306. <https://doi.org/10.1039/b9nr00427k>.
- (50) Kumar, M.; Ando, Y. Chemical Vapor Deposition of Carbon Nanotubes: A Review on Growth Mechanism and Mass Production. *J. Nanosci. Nanotechnol.* **2010**, 10 (6), 3739–3758. <https://doi.org/10.1166/jnn.2010.2939>.
- (51) Naddaka, M.; Asen, F.; Freza, S.; Bobrowski, M.; Skurski, P.; Laux, E.; Charmet, J.; Keppner, H.; Bauer, M.; Lellouche, J.-P. Functionalization of Parylene during Its Chemical Vapor Deposition. *J. Polym. Sci. Part Polym. Chem.* **2011**, 49 (13), 2952–2958. <https://doi.org/10.1002/pola.24731>.
- (52) Vaeth, K. M.; Jensen, K. F. Transition Metals for Selective Chemical Vapor Deposition of Parylene-Based Polymers. *Chem. Mater.* **2000**, 12 (5), 1305–1313. <https://doi.org/10.1021/cm990642p>.
- (53) Fortin, J. B.; Lu, T.-M. A Model for the Chemical Vapor Deposition of Poly(*Para* - Xylylene) (Parylene) Thin Films. *Chem. Mater.* **2002**, 14 (5), 1945–1949. <https://doi.org/10.1021/cm010454a>.
- (54) Kim, B. J.; Meng, E. Micromachining of Parylene C for bioMEMS. *Polym. Adv. Technol.* **2016**, 27 (5), 564–576. <https://doi.org/10.1002/pat.3729>.
- (55) Liger, M.; Harder, T. A.; Tai, Y.-C.; Konishi, S. Parylene-Pyrolyzed Carbon for MEMS Applications. In *17th IEEE International Conference on Micro Electro Mechanical Systems. Maastricht MEMS 2004 Technical Digest*; 2004; pp 161–164. <https://doi.org/10.1109/MEMS.2004.1290547>.
- (56) Pruden, K. G.; Sinclair, K.; Beaudoin, S. Characterization of Parylene-N and Parylene-C Photooxidation. *J. Polym. Sci. Part Polym. Chem.* **2003**, 41 (10), 1486–1496. <https://doi.org/10.1002/pola.10681>.
- (57) Chang, T. Y.; Yadav, V. G.; De Leo, S.; Mohedas, A.; Rajalingam, B.; Chen, C.-L.; Selvarasah, S.; Dokmeci, M. R.; Khademhosseini, A. Cell and Protein Compatibility of Parylene-C Surfaces. *Langmuir* **2007**, 23 (23), 11718–11725. <https://doi.org/10.1021/la7017049>.
- (58) Chun, W.; Chou, N.; Cho, S.; Yang, S.; Kim, S. Evaluation of Sub-Micrometer Parylene C Films as an Insulation Layer Using Electrochemical Impedance Spectroscopy. *Prog. Org. Coat.* **2014**, 77 (2), 537–547. <https://doi.org/10.1016/j.porgcoat.2013.11.020>.
- (59) Morton, K. C.; Morris, C. A.; Derylo, M. A.; Thakar, R.; Baker, L. A. Carbon Electrode Fabrication from Pyrolyzed Parylene c. *Anal. Chem.* **2011**, 83 (13), 5447–5452. <https://doi.org/10.1021/ac200885w>.
- (60) Song, Z.; Park, J.-H.; Kim, H.-R.; Lee, G.-Y.; Kang, M.-J.; Kim, M.-H.; Pyun, J.-C. Carbon Electrode Obtained via Pyrolysis of Plasma-Deposited Parylene-C for Electrochemical Immunoassays. *Analyst* **2022**, 147 (16), 3783–3794. <https://doi.org/10.1039/D2AN00854H>.

- (61) Gorzolnik, B.; Mela, P.; Moeller, M. Nano-Structured Micropatterns by Combination of Block Copolymer Self-Assembly and UV Photolithography. *Nanotechnology* **2006**, *17* (19), 5027–5032. <https://doi.org/10.1088/0957-4484/17/19/042>.
- (62) Dun, G.-H.; Zhang, H.; Qin, K.; Tan, X.; Zhao, R.; Chen, M.; Huang, Y.; Geng, X.-S.; Li, Y.-Y.; Li, Y.; Wan, P.; Gou, G.-Y.; Feng, Q.-X.; Zheng, X.-R.; Liang, R.; Xie, D.; Zhou, Y.; Wang, X.; Tian, H.; Yang, Y.; Ren, T.-L. Wafer-Scale Photolithography-Pixeled Pb-Free Perovskite X-Ray Detectors. *ACS Nano* **2022**, *16* (7), 10199–10208. <https://doi.org/10.1021/acsnano.2c01074>.
- (63) Weineck, G.; Zastera, D.; Dallas, A. J. AMC Control in Photolithography: The Past Decade in Review. In *Metrology, Inspection, and Process Control for Microlithography XXIV*; SPIE, 2010; Vol. 7638, pp 1091–1099. <https://doi.org/10.1117/12.847258>.
- (64) Zachek, M. K.; Park, J.; Takmakov, P.; Wightman, R. M.; McCarty, G. S. Microfabricated FSCV-Compatible Microelectrode Array for Real-Time Monitoring of Heterogeneous Dopamine Release. *The Analyst* **2010**, *135* (7), 1556. <https://doi.org/10.1039/c0an00114g>.
- (65) Anscombe, N. Direct Laser Writing. *Nat. Photonics* **2010**, *4* (1), 22–23. <https://doi.org/10.1038/nphoton.2009.250>.
- (66) Yang, C.; Cao, Q.; Puthongkham, P.; Lee, S. T.; Ganesana, M.; Lavrik, N. V.; Venton, B. J. 3D-Printed Carbon Electrodes for Neurotransmitter Detection. *Angew. Chem. Int. Ed.* **2018**, *57* (43), 14255–14259. <https://doi.org/10.1002/anie.201809992>.
- (67) Beidaghi, M.; Wang, C. Micro-Supercapacitors Based on Three Dimensional Interdigital Polypyrrole/C-MEMS Electrodes. *Electrochimica Acta* **2011**, *56* (25), 9508–9514. <https://doi.org/10.1016/j.electacta.2011.08.054>.
- (68) Weber, K.; Werdehausen, D.; König, P.; Thiele, S.; Schmid, M.; Decker, M.; De Oliveira, P. W.; Herkommer, A.; Giessen, H. Tailored Nanocomposites for 3D Printed Micro-Optics. *Opt. Mater. Express* **2020**, *10* (10), 2345. <https://doi.org/10.1364/OME.399392>.
- (69) Li, Y.; Park, S.; McLamb, M.; Lata, M.; Schöche, S.; Childers, D.; Aggarwal, I. D.; Poutous, M. K.; Boreman, G.; Hofmann, T. UV to NIR Optical Properties of IP-Dip, IP-L, and IP-S after Two-Photon Polymerization Determined by Spectroscopic Ellipsometry. *Opt. Mater. Express* **2019**, *9* (11), 4318. <https://doi.org/10.1364/OME.9.004318>.
- (70) Shao, Z.; Zhao, H.; Dunham, K. E.; Cao, Q.; Lavrik, N. V.; Venton, B. J. 3D-Printed Carbon Nanoneedle Electrodes for Dopamine Detection in *Drosophila*. *Angew. Chem.* **2024**, *136* (30), e202405634. <https://doi.org/10.1002/ange.202405634>.
- (71) Xiao, N.; Dong, X.; Song, L.; Liu, D.; Tay, Y.; Wu, S.; Li, L.-J.; Zhao, Y.; Yu, T.; Zhang, H.; Huang, W.; Hng, H. H.; Ajayan, P. M.; Yan, Q. Enhanced Thermopower of Graphene Films with Oxygen Plasma Treatment. *ACS Nano* **2011**, *5* (4), 2749–2755. <https://doi.org/10.1021/nn2001849>.

- (72) Hartney, M. A.; Hess, D. W.; Soane, D. S. Oxygen Plasma Etching for Resist Stripping and Multilayer Lithography. *J. Vac. Sci. Technol. B Microelectron. Process. Phenom.* **1989**, *7* (1), 1–13. <https://doi.org/10.1116/1.584440>.
- (73) Yang, C.; Wang, Y.; Jacobs, C. B.; Ivanov, I. N.; Venton, B. J. O₂ Plasma Etching and Antistatic Gun Surface Modifications for CNT Yarn Microelectrode Improve Sensitivity and Antifouling Properties. *Anal. Chem.* **2017**, *89* (10), 5605–5611. <https://doi.org/10.1021/acs.analchem.7b00785>.
- (74) Escribano, R.; Sloan, J. J.; Siddique, N.; Sze, N.; Dudev, T. Raman Spectroscopy of Carbon-Containing Particles. *Vib. Spectrosc.* **2001**, *26* (2), 179–186. [https://doi.org/10.1016/S0924-2031\(01\)00106-0](https://doi.org/10.1016/S0924-2031(01)00106-0).
- (75) Oliveira, R. R. L.; Albuquerque, D. A. C.; Cruz, T.; Yamaji, F.; Leite, F. Measurement of the Nanoscale Roughness by Atomic Force Microscopy: Basic Principles and Applications. In *Atomic Force Microscopy - Imaging, Measuring and Manipulating Surfaces at the Atomic Scale*; 2012. <https://doi.org/10.5772/37583>.
- (76) Mattevi, C.; Wirth, C. T.; Hofmann, S.; Blume, R.; Cantoro, M.; Ducati, C.; Cepek, C.; Knop-Gericke, A.; Milne, S.; Castellarin-Cudia, C.; Dolafi, S.; Goldoni, A.; Schloegl, R.; Robertson, J. In-Situ X-Ray Photoelectron Spectroscopy Study of Catalyst–Support Interactions and Growth of Carbon Nanotube Forests. *J. Phys. Chem. C* **2008**, *112* (32), 12207–12213. <https://doi.org/10.1021/jp802474g>.
- (77) Arepalli, S.; Nikolaev, P.; Gorelik, O.; Hadjiev, V.; Holmes, W.; Files, B.; Yowell, L. Protocol for the Characterization of Single-Wall Carbon Nanotube Material Quality. *Carbon* **2004**, *42*, 1783–1791. <https://doi.org/10.1016/j.carbon.2004.03.038>.
- (78) Carvalho, A. F.; Fernandes, A. J. S.; Leitão, C.; Deuermeier, J.; Marques, A. C.; Martins, R.; Fortunato, E.; Costa, F. M. Laser-Induced Graphene Strain Sensors Produced by Ultraviolet Irradiation of Polyimide. *Adv. Funct. Mater.* **2018**, *28* (52), 1805271. <https://doi.org/10.1002/adfm.201805271>.
- (79) Gu, X. J. Raman Spectroscopy and the Effects of Ultraviolet Irradiation on Polyimide Film. *Appl. Phys. Lett.* **1993**, *62* (13), 1568–1570. <https://doi.org/10.1063/1.108643>.
- (80) Ha, Y.; Choi, M.-C.; Jo, N.; Kim, I.; Ha, C.-S.; Han, D.; Han, S.; Han, M. Polyimide Multilayer Thin Films Prepared via Spin Coating from Poly(Amic Acid) and Poly(Amic Acid) Ammonium Salt. *Macromol Res* **2008**, *16* (8), 9.
- (81) Jenekhe, S. A. The Rheology and Spin Coating of Polyimide Solutions. *Polym. Eng. Sci.* **1983**, *23* (15), 830–834. <https://doi.org/10.1002/pen.760231508>.
- (82) Getachew, B. A.; Bergsman, D. S.; Grossman, J. C. Laser-Induced Graphene from Polyimide and Polyethersulfone Precursors as a Sensing Electrode in Anodic Stripping Voltammetry. *ACS Appl. Mater. Interfaces* **2020**, *12* (43), 48511–48517. <https://doi.org/10.1021/acsami.0c11725>.

- (83) Beckham, J. L.; Li, J. T.; Stanford, M. G.; Chen, W.; McHugh, E. A.; Advincula, P. A.; Wyss, K. M.; Chyan, Y.; Boldman, W. L.; Rack, P. D.; Tour, J. M. High-Resolution Laser-Induced Graphene from Photoresist. *ACS Nano* **2021**, *15* (5), 8976–8983. <https://doi.org/10.1021/acsnano.1c01843>.
- (84) Lin, J.; Peng, Z.; Liu, Y.; Ruiz-Zepeda, F.; Ye, R.; Samuel, E. L. G.; Yacaman, M. J.; Yakobson, B. I.; Tour, J. M. Laser-Induced Porous Graphene Films from Commercial Polymers. *Nat. Commun.* **2014**, *5* (1), 5714. <https://doi.org/10.1038/ncomms6714>.
- (85) Peng, Z.; Lin, J.; Ye, R.; Samuel, E. L. G.; Tour, J. M. Flexible and Stackable Laser-Induced Graphene Supercapacitors. *ACS Appl. Mater. Interfaces* **2015**, *7* (5), 3414–3419. <https://doi.org/10.1021/am509065d>.
- (86) Rathinam, K.; Singh, S. P.; Li, Y.; Kasher, R.; Tour, J. M.; Arnusch, C. J. Polyimide Derived Laser-Induced Graphene as Adsorbent for Cationic and Anionic Dyes. *Carbon* **2017**, *124*, 515–524. <https://doi.org/10.1016/j.carbon.2017.08.079>.
- (87) Liana, D. D.; Raguse, B.; Gooding, J. J.; Chow, E. Recent Advances in Paper-Based Sensors. *Sensors* **2012**, *12* (9), 11505–11526. <https://doi.org/10.3390/s120911505>.
- (88) Wang, Y.-H.; Song, P.; Li, X.; Ru, C.; Ferrari, G.; Balasubramanian, P.; Amabili, M.; Sun, Y.; Liu, X. A Paper-Based Piezoelectric Accelerometer. *Micromachines* **2018**, *9* (1), 19. <https://doi.org/10.3390/mi9010019>.
- (89) Liu, X. Y.; O'Brien, M.; Mwangi, M.; Li, X. J.; Whitesides, G. M. Paper-Based Piezoresistive MEMS Force Sensors. In *2011 IEEE 24th International Conference on Micro Electro Mechanical Systems*; 2011; pp 133–136. <https://doi.org/10.1109/MEMSYS.2011.5734379>.
- (90) Jiang, Y. Q.; Zhou, Q.; Lin, L. Planar MEMS Supercapacitor Using Carbon Nanotube Forests. In *2009 IEEE 22nd International Conference on Micro Electro Mechanical Systems*; 2009; pp 587–590. <https://doi.org/10.1109/MEMSYS.2009.4805450>.
- (91) Chen, W.; Beidaghi, M.; Penmatsa, V.; Bechtold, K.; Kumari, L.; Li, W. Z.; Wang, C. Integration of Carbon Nanotubes to C-MEMS for On-Chip Supercapacitors. *IEEE Trans. Nanotechnol.* **2010**, *9* (6), 734–740. <https://doi.org/10.1109/TNANO.2010.2049500>.

Chapter 2

Carbon nanospikes have improved sensitivity and anti-fouling properties for adenosine, hydrogen peroxide, and histamine

Abstract

Carbon nanospikes (CNSs) are a new nanomaterial that have enhanced surface roughness and surface oxide concentration, increasing the sensitivity for dopamine detection. However, CNS-modified electrodes (CNSMEs) have not been characterized for other neurochemicals, particularly those with higher oxidation potentials. The purpose of this study was to evaluate CNSMEs for the detection of adenosine, hydrogen peroxide (H_2O_2), and histamine. The sensitivity increased with CNSs, and signals at CNSMEs were about 3.3 times higher than CFMEs. Normalizing for surface area differences using background currents, CNSMEs show an increased signal of 4.8 times for adenosine, 1.5 times for H_2O_2 , and 2 times for histamine. CNSMEs promoted the formation of secondary products for adenosine and histamine, which enables differentiation from other analytes with similar oxidation potentials. CNSs also selectively enhance the sensitivity for adenosine and histamine compared to H_2O_2 . A scan-rate test reveals that adenosine is more adsorption-controlled at CNS electrodes than CFMEs. CNSMEs are anti-fouling for histamine, with less fouling because the polymers formed after histamine electrooxidation do not adsorb due to an elevated number of edge planes. CNSMEs were useful for detecting each analyte applied in brain slices. Because of the hydrophilic surface compared to CFMEs, CNSMEs also have reduced biofouling when used in tissue. Therefore, CNSMEs are useful for tissue measurements of adenosine, histamine, and hydrogen peroxide with high selectivity and low fouling.

2.1 Introduction

Carbon-fiber microelectrodes (CFMEs) are traditionally used for the detection of neurotransmitters with fast-scan cyclic voltammetry (FSCV) because carbon is good at adsorbing monoamine neurotransmitters [1-4]. Carbon nanomaterials have been added to electrodes to enhance the neurotransmitter detection, increasing electron transfer and enhancing sensitivity. For example, carbon nanotubes (CNTs) can be coated onto electrodes or made into fibers, like CNT yarns (CNTY), that are made into electrodes [7-10]. However, the synthesis of CNTs requires a metal catalyst for growth and they are hard to grow on cylindrical electrodes [11-13]. Carbon nanospikes (CNSs) are another type of carbon nanomaterial with many edge planes that are easier to coat on cylindrical electrodes, as they are grown using plasma-enhanced chemical vapor deposition (PE-CVD) without a catalyst [14, 15]. CNSs are sp² hybridized and spike-like, so they increase surface roughness [15-17]. CNSs enhanced the sensitivity for dopamine and had better electrochemical performance than CNTs and carbon fibers (CFs) due to both increased surface roughness and oxide groups [17, 18]. The oxide groups accelerate the electron transfer rate by increasing the density of states (DOS) and enhance the signal by promoting adsorption of neurotransmitters [8, 18-21]. However, dopamine is relatively easy to oxidize, and CNS-modified electrodes have not been used to examine analytes that have higher oxidation potentials.

Electrochemical studies of neurotransmitters traditionally concentrate on monoamines such dopamine or serotonin [22]. However, electrochemical detection is expanding into other compounds with higher oxidation potentials, including adenosine, hydrogen peroxide, and histamine [23-26]. Adenosine is a neuromodulator involved in vasodilation and sleep regulation and an essential precursor for generation of AMP, ADP, and ATP [27-29]. Adenosine is identified by its primary and secondary oxidation potentials, located around 1.45 V and 1.15 V, respectively [23, 30-32]. Detection of the secondary oxidation peak for adenosine aids in selectivity of its detection from other analytes [30, 33]. Hydrogen peroxide, a strong oxidant,

functions as an important signaling agent between neuronal and glial cells, but intermediate hydroxyl radicals formed by the interaction with iron and copper also damage the structures of lipids, nucleic acid, and proteins [34]. Additionally, H_2O_2 is also involved in the regulation of dopamine release [35, 36]. Excessive amounts of H_2O_2 can be extremely harmful to the brain. While hydrogen peroxide is traditionally detected at platinum coated electrodes [37-39], the Sombers group showed that CFMEs oxidize H_2O_2 because of defect sites and the oxidation potential occurs at 1.2 V with FSCV [39]. Since CNSs possess a higher level of oxide groups, H_2O_2 should adsorb to the surface more compared to CFMEs. Histamine is a neuromodulator in the brain and immune system and a molecule that is released during stress [40, 41]. Histamine has a primary oxidation potential around 1.4 V and a secondary peak at 0.8 V [26]. Histamine forms a polymer during electrooxidation that covers the electrode surface by π - π stacking, decreasing electrode sensitivity through fouling [25, 26, 42]. The increased number of oxide groups of CNSs should promote adsorption by electrostatic forces but the decrease in basal planes due to the surface roughness may decrease the polymer attachment and lead to less fouling [14, 18, 43, 44]. CNS electrodes have potential advantages for adenosine, histamine, and hydrogen peroxide, but their electrochemistry has not been detected at CNSMEs.

The goal of this study was to explore the electrochemistry of adenosine, hydrogen peroxide (H_2O_2), and histamine at CNSMEs. CNSMEs had a good performance for adenosine with increased adsorption and sensitivity compared to CFMEs. Surface oxide groups favor the strong attraction of adenosine and promote the detection of the secondary oxidation peak. Currents for hydrogen peroxide were also enhanced at CNSMEs and detection was a hybrid of diffusion- and adsorption-controlled process. Histamine currents increased at CNSMEs, and histamine fouling decreased because there are more edge planes on CNSs that prevent fouling. Therefore, CNS modified electrodes are useful for precise measurements of neuromodulators

with high oxidation potentials and will contribute to understanding of rapid neuromodulation in the brain.

2.2 Methods and Materials

2.2.1 Chemicals and materials

Adenosine and histamine were purchased from ThermoFisher Scientific (Waltham, WA) and hydrogen peroxide (H_2O_2) was from Thomas Scientific (Swedesboro, NJ). Stock solutions (10 mM) were made in perchloric acid (0.1 M). Phosphate-buffered saline (PBS) buffer (131.5 mM NaCl, 3.25 mM KCl, 1.2 mM CaCl_2 , 1.25 mM NaH_2PO_4 , 1.2 mM MgCl_2) was used to dilute stock solutions to 1.0 μM . De-ionized water (EMD Millipore, Billerica, MA) was used to prepare all aqueous solutions.

2.2.3 Construction of CNSMEs

Plasma-enhanced chemical vapor deposition (PECVD) was used to grow CNSs directly on Nb wires (diameter 25 μm , ESPI Metals, Ashland, OR). A stainless-steel stage was used to hold niobium wires, which are treated as cathodes. CNSs are grown in a custom-built DC PECVD chamber which is flowing with 100 sccm ammonia and 80 sccm acetylene at 6 Torr pressure, 650°C for 6 min. The DC plasma discharge parameters were: 500 mA, 0.230 kW, and 480-550 V. Glass capillaries were utilized to contain Nb wires coated with CNSs and sealed by using 5-min epoxy (J-B weld, Sulphur Springs, TX).

2.2.4 Construction of CF microelectrodes

Glass capillaries were used to contain carbon fibers with a diameter of 7 μm (T650-35, Cytec, Woodland Park, NJ). PE-21 pipette puller (**Setagaya-ku, Tokyo, Japan**) was used to pull glass capillaries that contained CF into two identical needle-shaped microelectrodes by applying heat to the center of the glass capillary. CFs in needle-shaped microelectrodes were cut to 50-100 μm . Microelectrodes were sealed by dipping the tips in a solution of Epon Resin 828 (Danbury, CT) with 14% (w/w) m-phenylenediamine (Acros Organics, Morris Plains, NJ) for 30 s. Acetone was used to rinse the electrodes for 5 s. Sealed electrodes were placed at room

temperature overnight and then the oven at 100°C for was utilized to harden epoxy in the electrodes for 2 h and at 150°C overnight.

2.2.5 Instrumentation

Scanning electron microscopy images were collected by Merlin field emission SEM (Zeiss, Thornwood, NY) and FEI Quanta 650 SEM (ThermoFisher Scientific, Waltham, MA). 5.0 kV was performed on secondary electron detector as the accelerating voltage. An X-ray photoelectron spectrometer (Physical Electronics, Chanhassen, MN) was utilized to characterize the surface functional groups of CNSs.

FSCV data was collected with a ChemCam potentiostat (Dagan, Minneapolis, MN) with a headstage with 1 M Ω resistance. The triangular waveform was applied from -0.4 V to 1.45 V, at a scan rate of 400 V*s⁻¹ and a frequency of 10 Hz. Data analysis was performed using HDCV Analysis Software (Department of Chemistry, University of North Carolina at Chapel Hill). The reference electrode was a silver/silver chloride wire. A six-port, stainless steel HPLC loop injector with an air actuator (VICI Valco Instruments, Houston, TX) was used to inject samples through a flow cell at 2 mL/min. Four M KCl was filled in the glass capillary to connect with a silver wire in the electrode holder (Warner Instruments, Holliston, MA).

2.2.6 Brain Slice Preparation

All animal experiments were performed following the approved protocols by the Animal Care and Use Committee (ACUC) of the University of Virginia. 5-8 weeks old wild-type C57BL/6 mice (Jackson Lab) were anesthetized using isoflurane and decapitation quickly. Gently the brain was removed and transferred rapidly into 0–5 °C oxygenated aCSF (95% O₂, 5% CO₂) for recovery. After 2 minutes, the brain was mounted on the slicing stage and coronal section slices (400 μ m) prepared via a vibratome (Leica VT1000S, Bannockburn, IL, USA). Slices with caudate putamen were transferred and equilibrated for 30-45 minutes into oxygenated aCSF (34°C) in a water bath. Once the slice was moved to the recording chamber, the CNSME was inserted approximately 75 μ m deep into the caudate tissue and equilibrated for 10-15 minutes.

Oxygenated aCSF was continuously perfused over the slice at a flow rate of 2 mL/min. A glass capillary holding the respective analyte was placed close to the working electrode. A precise amount of adenosine was microinjected into the tissue using a nanoliter injector (Nanoliter2020, World Precision Instrument, FL) and recorded using HDCV software. A similar approach was used to analyze histamine and H₂O₂ in the brain slice.

2.3 Results

2.3.1 Scanning electron microscopy (SEM)

First, we characterized the surface of CNSs and CF with scanning electron microscopy. Fig.1A and B show the morphology of the CF microelectrode, both overall and close up. The surface of CFMEs is relatively smooth, with some striations. Fig. 1C and D show CNS modified Nb wire and the CNSs have a dense nanostructure with features less than 100 nm. The thickness of the coating is around 1 μm . CNS electrodes have a larger surface roughness than CF electrodes which increases sensitivity.

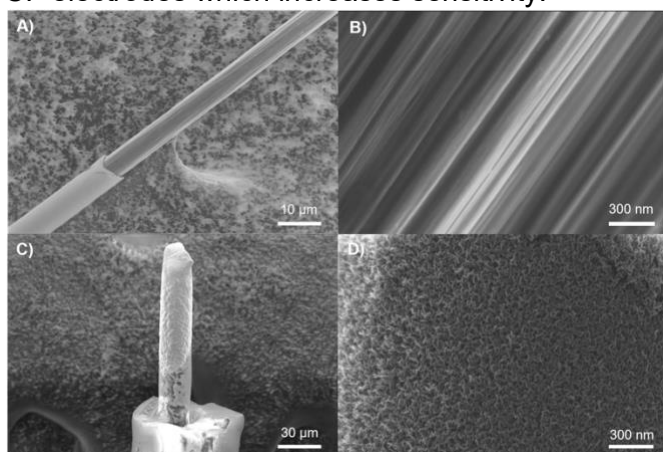


Figure 1. Scanning electron microscopy images of (A) CFME (B) zoomed in surface of CFME (C) CNSME and (D) zoomed in surface of CNSs.

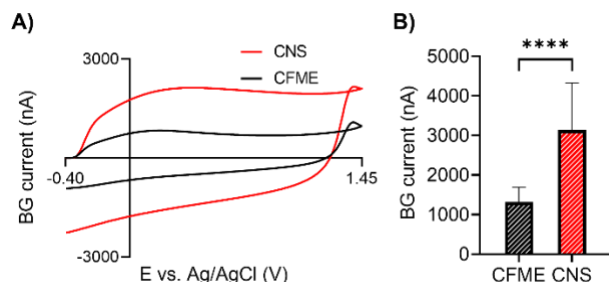


Figure 2. Background currents of CFMEs and CNSMEs. (A) CV graphs of background currents (B) Bar graphs of background currents on multiple electrodes (unpaired t-test, $n=6$, $**p<0.01$, $***p<0.001$, $****p<0.0001$)

Next, we compared the relative size of CFs and CNSs backgrounds to examine differences in surface area. In Fig. 2A, background charging currents were plotted for CFs and CNSs. Because the diameter of the CNS-coated Nb wires (25 μm) is larger than CFs (7 μm), surface area and background currents are also larger, about 2.5 times. The bar graphs in Fig.

2B compare the average background currents of CFs and CNSs, and CNSs have significantly higher currents than CFs (unpaired t-test, $p < 0.0001$, $n = 17$). The larger surface area provides more active sites for neurochemicals to be detected.

2.3.2 CNSs Increase Sensitivity for Adenosine

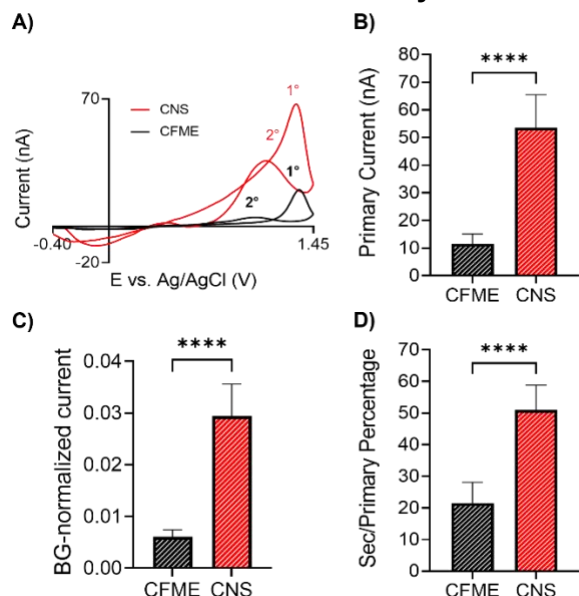
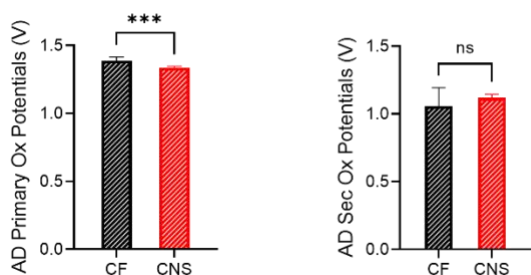


Figure 3. Adenosine detection on CFMEs and CNSMEs. (A) CVs of 1 μM adenosine (B) Bar graph of 1 μM adenosine currents (unpaired t-test, $n = 6$) (C) Bar graphs of background-normalized currents of 1 μM adenosine, where the Faradaic current was divided by the background current with multiple electrodes (unpaired t-test, $n = 6$) (D) Bar graph of secondary/primary oxidation current ratio (unpaired t-test, $n = 6$, **** $p < 0.0001$).

FSCV was used for real-time electrochemical detection of adenosine by applying the adenosine waveform, which scans from -0.4V to 1.45 V and at 400 V/s at 10 Hz. Fig. 3A compares CVs of CFMEs and CNSMEs in 1 μM adenosine. Adenosine has two oxidation peaks, a primary peak, whose oxidation potential is about 1.35 V on the back scan of the adenosine waveform, and a secondary peak, which has an oxidation potential of 1.15V, is on the forward scan [22-25]. Both oxidation peaks are larger at CNS electrodes, with the secondary peak becoming particularly prominent. The average oxidation potential, 1.34 V, for adenosine at CNSMEs is slightly lower than 1.39 V for CFMEs (Fig. 4A). As they are located on the back scan of the waveform, the lower value means slower electron transfer kinetics. Therefore, CNSMEs show increased signals but not accelerated electron transfer for adenosine [18].

A) AD Primary Ox Potential B) AD Secondary Ox Potential



C) H₂O₂ Primary Ox Potential D) HA Primary Ox Potential

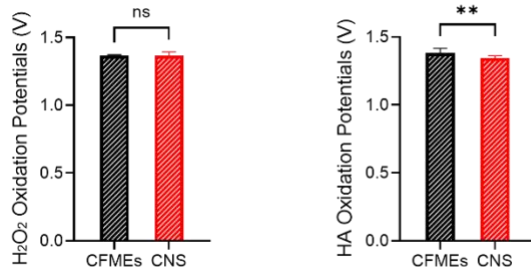


Figure 4. Oxidation potentials of adenosine, H₂O₂, and histamine on CFMEs and CNSMEs (A) Bar graphs of adenosine primary oxidation potentials (unpaired t-test, n=6) B) Bar graphs of adenosine secondary oxidation potentials (unpaired t-test, n=6) (C) Bar graphs of H₂O₂ oxidation potentials (unpaired t-test, n=6) (D) Bar graphs of histamine primary oxidation potentials (** $p < 0.01$, *** $p < 0.001$, **** $p < 0.0001$, by unpaired t-test, n=6)

Fig. 3B compares the primary currents and shows that CNS modified electrode have about 5.3 times higher primary oxidation currents than CFMEs (unpaired t-test, $p < 0.0001$, n=6). CNSMEs have larger surface areas and therefore will have larger Faradaic currents, but in order to see if CNSMEs were more electroactive, the Faradaic currents were normalized for the area by taking the ratio of oxidation currents to background currents (Fig. 4C). CNS electrodes had higher increases in the oxidation current than backgrounds, so their normalized currents are 4.8 times higher than CFMEs, a significant difference (unpaired t-test, $p < 0.0001$, n=6). Because the normalized currents are larger, this implies that the increased Faradaic currents are not just due to surface area. X-ray photoelectron (XPS) spectra in Fig. 5 showed that CNSs possess more oxygen functional groups than CFMEs, particularly carboxylic acids. Surface oxide groups are likely driving adenosine detection by electrostatic forces or hydrogen bonds formed between surface oxide groups and lone pairs of electrons in the nitrogen atom of adenosine [45, 46]. In Fig. 3D, the ratio of the secondary oxidation peak to primary oxidation peak is plotted. The CNS

electrodes have a significantly larger ratio of secondary current (unpaired t-test, $p < 0.0001$, $n = 6$), which suggests that CNSs adsorb or trap the adenosine oxidation product strongly, facilitating the secondary oxidation process. Although CNSMEs did not have enhanced electron transfer than CFMEs, more adsorption of the secondary product likely contributed to a higher secondary oxidation peak.

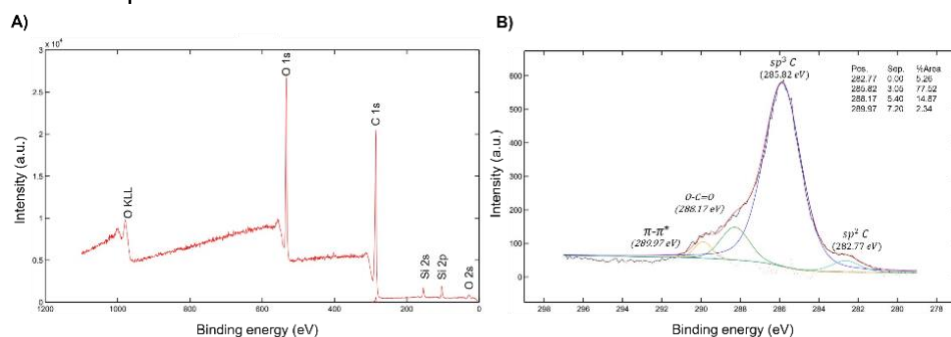


Figure 5. X-ray photoelectron (XPS) spectra of CNSs (A) survey scan (B) XPS C 1s peak composed of sp^2 C (285.82 eV), sp^3 C (282.77 eV), O-C=O (288.17 eV), and π - π^* bonds (289.97 eV)

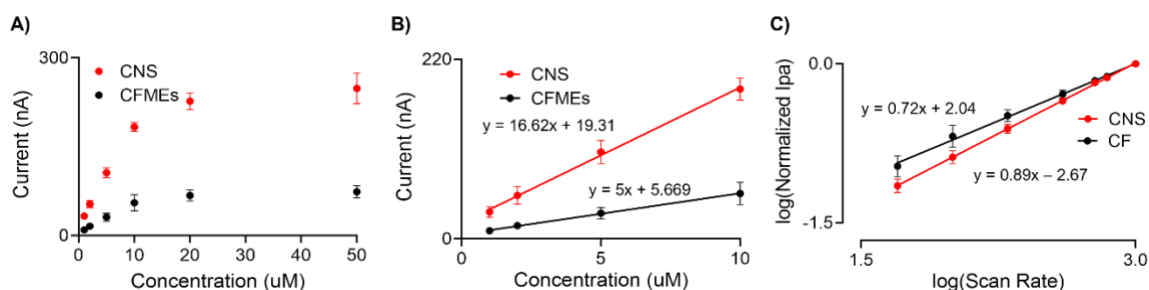


Figure 6. Electrochemical performance of adenosine on CFMEs and CNSMEs. (A) Adenosine concentration tests (1 – 50 μ M) (B) Adenosine sensitivity in linear range (1 – 10 μ M) and (C) Adenosine scan rate tests (50 – 1000 V/s) ($n = 3$ electrodes).

Next, we tested CNS electrodes for detecting adenosine with different concentrations and scan rates to study adsorption. In Figure 6A, the variation of adenosine primary oxidation peak currents is plotted against concentration. The magnitude of oxidation current for CNSMEs is larger than CFMEs. The linear relationship between current and concentration is lost over 10 μ M because the surface is saturated with analyte and adsorption sites are limited. Therefore, the linear range was plotted from 1–10 μ M (Fig. 6B). The slope of the line for CNSMEs is 3.3 times higher than for CFMEs, showing they have higher sensitivity. In Fig. 6C, a scan rate experiment was performed to examine the extent to which the detection of adenosine is diffusion or adsorption controlled. When the slope of log normalized peak current vs. log scan

rate is 0.5, the primary current is diffusion controlled. If the slope is equal to 1, the detection is adsorption controlled. Both slopes of CFMEs and CNSMEs are between 0.5 and 1.0, which means that the detections are hybrids of diffusion and adsorption. CNSMEs have a higher slope, 0.89, than CFMEs, 0.72, meaning the surface of CNSs promotes adsorption of adenosine and increases the sensitivity.

2.3.3 CNSs Increase Sensitivity for Hydrogen Peroxide

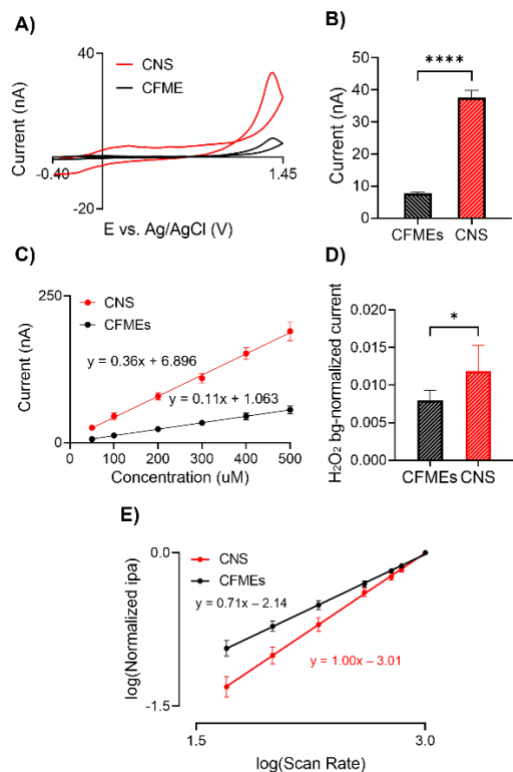


Figure 7. Electrochemical performance of H₂O₂ on at CFMEs and CNSMEs. A) CVs of 50 μM H₂O₂ B) Bar graphs of average current for detection of 50 μM H₂O₂, (unpaired t-test, n=6) (C) H₂O₂ sensitivity tests (50 – 500 μM) (D) Bar graphs of background-normalized currents of 50 μM H₂O₂ (unpaired t-test, n=6) (E) Hydrogen peroxide scan-rate tests (50-1000 V/s) (n=3) (*p<0.05, **** p<0.0001)

Detection of H₂O₂ is difficult at CFMEs because of electrochemical impedance and surface chemistry [47-49]. CNSMEs were compared with CFMEs to examine sensitivity and electron transfer. Fig. 7A shows the detection of 50 μM H₂O₂ at a CFME and CNSME using the adenosine waveform. H₂O₂ undergoes one oxidation, and the peak is located on the back-scan. The oxidation potentials are 1.365 V for CFMEs and 1.366 V for CNSMEs, so there is not a significant electrocatalytic effect (Fig. 4). CNSMEs have significantly higher currents for H₂O₂

than CFMEs (Fig. 7B, unpaired t-test, $p=0.0095$, $n=6$). Fig. 7C shows the response to increasing H_2O_2 concentrations, 50-500 μM . Fig. 7C plots primary currents vs concentration and the slope of CNSs (0.36) is about 3.3 times higher than CFMEs (0.11). Fig. 7D shows the background normalized currents are 1.5 times higher for CNSMEs than for CFMEs (unpaired t-test, $p<0.0001$, $n=6$), implying that the surface is more active for hydrogen peroxide detection and the enhancement is not all due to area. Hydrogen peroxide forms hydrogen bonds with small molecules, such as urea and sodium carbonate, to promote the interaction with oxygen-containing groups [47-49]. Rich surface oxide groups, like carboxylic acids, would benefit the adsorption of H_2O_2 during detection [50-52]. The scan rate test in Fig. 7E for H_2O_2 shows CNSMEs have a higher slope, 1.003 than CFMEs, 0.707, which means that CNSMEs are more adsorption-controlled for H_2O_2 detection.

2.3.4 CNSMEs have high sensitivity and antifouling properties for histamine detection

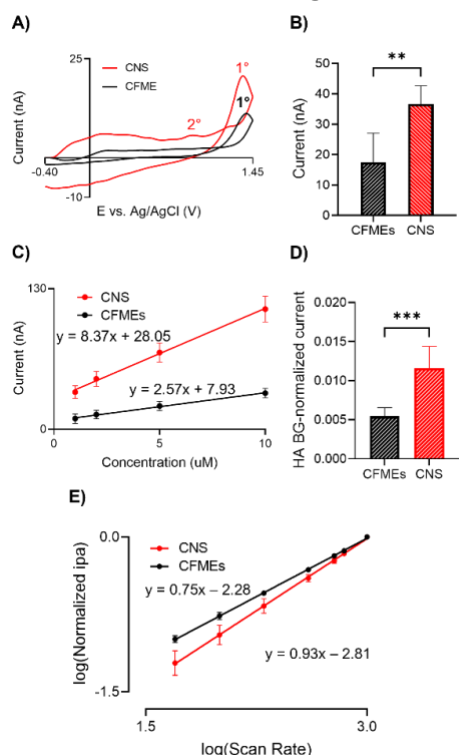
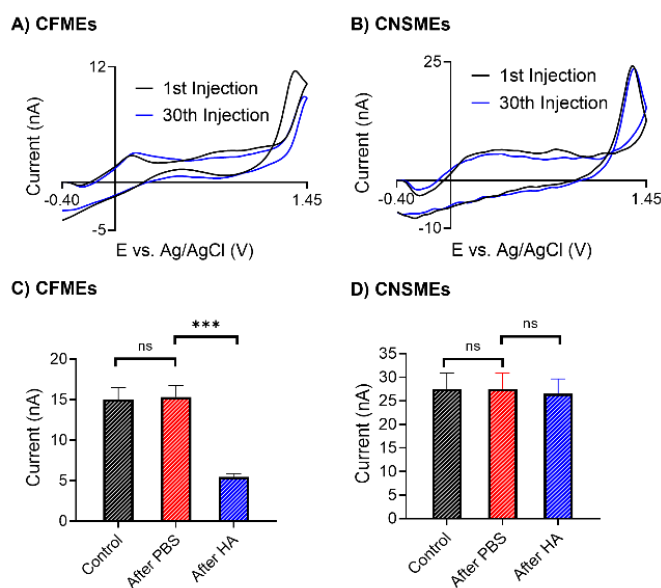


Figure 8. Electrochemical performance of histamine on CFMEs and CNSMEs. (A) CVs of 1 μM histamine. (B) Performance Currents for of 1 μM histamine detection on multiple electrodes (unpaired t-test, $n=6$). (C) Sensitivity test (1–10 μM). (D) Bar graphs of background-normalized currents of 1 μM histamine, (unpaired t-test, $n=6$). (E) Histamine scan-rate tests (50-1000 V/s) ($n=3$) (** $p < 0.01$, *** $p < 0.001$)

Histamine was detected using the adenosine waveform and primary oxidation and secondary potentials are about 1.4 V and 0.8 V on CFMEs (Fig 8A). The magnitude of the secondary oxidation peak for 1 μ M histamine at CNSMEs is slightly higher than CFMEs (Fig. 8A). The oxidation potential is located on the forward scan of adenosine waveform, at 1.344 V, which is lower than CFMEs, 1.382 V (Fig. 4D). Therefore, the oxidization of histamine has faster electron transfer at the CNS surface than CFMEs. Primary oxidation currents for histamine are significantly higher for CNSMEs than CFMEs (Fig. 8B, unpaired t-test, $p=0.0053$, $n=6$). For sensitivity, the slope for CNS electrodes is 8.4 $\text{nA}/\mu\text{M}$ and for CFMEs is 2.6 $\text{nA}/\mu\text{M}$ (Fig. 8C). Therefore, CNSMEs are about 3.2 times more sensitive than CFMEs without background-current normalization. With more adsorbed analyte on the electrode surface, the formation of secondary products was enhanced, shown as higher secondary oxidation peak. Fig. 8D compares background-normalized currents for CFMEs and CNSMEs and CNSMEs have a significantly higher normalized current (unpaired t-test, $p=0.0005$, $n=6$). The scan rate graphs in Fig. 8E show a higher slope of CNSMEs, 0.94, than CFMEs, 0.75, which indicates more adsorption-controlled detection of histamine on CNS. X-ray photoelectron (XPS) spectra in Fig. 5 showed that CNSs possess a more oxygen surface than CFMEs, especially for carboxylic groups, which benefit the attraction of positively charged analytes. All scan-rate tests show that



CNSs promote the adsorption of neurochemicals, likely because the increased oxygen groups strengthen electrostatic force onto the surface.

Figure 9. Multi-injections and long-term histamine fouling tests on CFMEs and CNSMEs. (A) CV graphs of 1st and 30th injection on CFMEs. (B) CV graphs of 1st and 30th injection of 1 μ M histamine on CNSMEs. (C) Peak currents of CFMEs before soaking in PBS buffer, after soaking in PBS buffer, after soaking in 1 μ M histamine (One-way ANOVA, Main effect $p < 0.0001$, Bonferroni post-test *** $p < 0.001$, $n = 4$). Error bars are SEM. (D) Peak currents of CNSMEs before soaking in PBS buffer and after soaking in 1 μ M histamine separately with the adenosine waveform applied (One-way ANOVA $p < 0.001$, $n = 4$, with Bonferroni post-test). Error bars are SEM.

Histamine polymerizes after being oxidized, and then sticks to the electrode, reducing sensitivity [32, 33]. We hypothesized that fouling would decrease at CNS electrodes because there is less basal plane for π - π interactions with polymers. Multiple injections of histamine were performed to test for fouling (Fig. 9), with 1 μ M histamine injected 30 times. In Fig. 9A, the current for histamine at the CFME dropped about 20% after 30 injections of histamine, which means that a polymer covers some of the CF surface. The oxidation potential for histamine at the CFME shifted from 1.36 V to 1.44 V, showing electron transfer slows. For CNSMEs, there was no difference between CVs of 1st and 30th injection of histamine (Fig. 9B). There also is no shift of the histamine oxidation potential. Thus, there is less fouling at CNSMEs and therefore likely less histamine polymer attachment to CNS surface.

To further test for long-term antifouling properties, electrodes were soaked in 1 μ M histamine (or PBS buffer for control) with the electrochemical waveform applied for an hour. In Fig. 9C, for CFMEs, the histamine dramatically fouled the CFMEs, with a drop from 15 nA to 5 nA, a decrease of about 67%. There is a significant difference between oxidation currents before and after cycling in histamine (one-way ANOVA, Bonferroni post-test, $p = 0.0003$, $n = 4$). Fig. 9D shows histamine fouling at CNS electrodes, and the peak for histamine drops only 7% after 1 hour of the waveform being applied, which is not significant (one-way ANOVA, Bonferroni post-test, $p = 0.9696$, $n = 3$). Consequently, both fouling tests demonstrate that CNSs have antifouling properties. CNSMEs have been used up to 4 hours and their performance

stayed the same, which shows stability. CNSMEs have been tested for 10 days previously and currents were consistent [14].

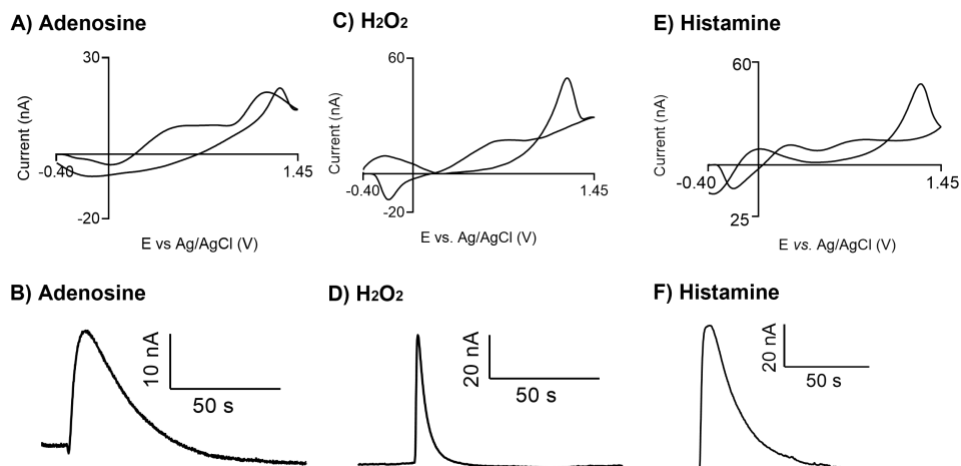


Figure 10. Detection of microinjected adenosine, H₂O₂, and histamine in the brain slice using CNSME. (A) CV graph of 100 pmol of adenosine, (B) i vs t curve for adenosine detection, (C) CV graph of 100 pmol H₂O₂, (D) i vs t curve for H₂O₂ detection (E) CV of 100 pmol of histamine (F) i vs t curve for histamine detection

CNSMEs were tested in the mouse brain slice (caudate-putamen) to test if different analytes can be measured in biological tissue. The electrode was inserted approximately 75 μm deep into the tissue, and analytes were microinjected close to the working electrode via a nanoliter injector. The background-subtracted CVs were used to identify analytes with oxidation peaks representing the corresponding analytes and the i vs t curve shows the electrode response towards these analytes. Adenosine (100 pmol) was puffed via a nanoliter injector near the working electrode. The background-subtracted CV has a characteristic primary peak (+1.3) and secondary peak for the adenosine at the CNSME (Fig. 10A). The secondary peak for adenosine is enhanced, a trend observed also at carbon fibers, likely because tissue traps the secondary product near the surface of the electrode, where it can be detected rather than diffuse away [53]. The i vs t curve (Fig. 10B) shows CNSME has a good response toward adenosine. Fig. 10C and D show the detection of 100 pmol of H₂O₂, and the response is similar *in vivo* to *in vitro*. Figure 10E and F show the detection of 100 pmol histamine. The primary and secondary oxidation peaks at 1.3V and 0.70V were observed for histamine. Slight changes in CV shape are observed *in vivo* and this is typically due to protein adsorption in the brain, which

may slightly slow electron transfer. These observations show that CNSEs can detect adenosine, histamine, and H_2O_2 in tissue.

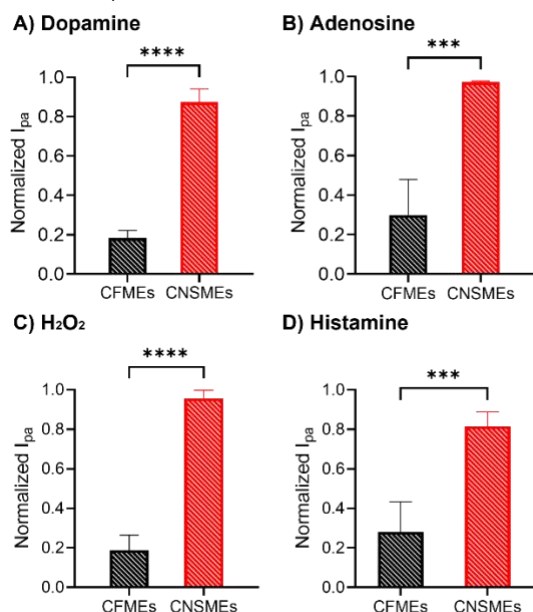


Figure 11. Biofouling experiments with rat brain tissue. (A) Bar graphs of normalized 1 μ M dopamine currents for CFMEs and CNSMEs. Data are normalized by dividing the signal after one hour by the signal before biofouling in each slice before and after being placed in the brain for 1 hour (unpaired t-test, n=4 slices) (B) Bar graphs of normalized 1 μ M adenosine currents of CFMEs and CNSMEs before and after being placed in the brain (unpaired t-test, n=4) (C) Bar graphs of normalized 20 μ M H_2O_2 currents of CFMEs and CNSMEs before and after being placed in the brain (unpaired t-test, n=4) (D) Bar graphs of normalized 1 μ M histamine currents of CFMEs and CNSMEs before and after being placed in the brain (unpaired t-test, (n=4) * p <0.05, ** p <0.01, *** p <0.001, **** p <0.0001) Error bars are SEM.

To study CNSMEs biofouling, sensitivity was tested with flow injection analysis before and after insertion in a piece of fresh brain tissue, with the adenosine waveform applied for 1 hour. CNSMEs have larger currents after biofouling, as the current was 87 % of the pre-tissue current for dopamine (Fig. 11A), 97 % for adenosine (Fig. 11B), 96 % for H_2O_2 (Fig. 11C), and 82 % for histamine (Fig. 11D). CFMEs, on the other hand, had over 50% signal reduction due to biofouling. Thus, CNSMEs have better performance for neurotransmitters in the brain, both for sensitivity and for anti-fouling properties. Defect sites on CNSMEs likely prevented proteins and polymers from being absorbed to the electrode surface and reducing sensitivity. This characteristic also makes them suitable for future *in vivo* experiments without being severely affected by biofouling.

2.4 Discussion

Previous studies found CNSs were a better material than CFs for electrochemical detection of dopamine [13]. Here, CNS microelectrodes increase the sensitivity for adenosine, hydrogen peroxide, and histamine about 3-fold. After normalizing currents for surface area, there is still better electrochemical performance for CNSMEs than CFMEs, indicating the surface changes are not only due to surface area [13, 36]. There are two factors that increase sensitivity. The first is increased surface roughness, and increased edge planes. Compared to the smooth texture of CFs, increased surface roughness of CNSs provides more sites for surface binding and favors the adsorption, particularly of cationic analytes, to the surface. The second factor that increases sensitivity is an increase in surface oxide groups, as evidenced by XPS, and particularly carboxylic acid groups. These groups also promote adsorption, particularly of adenosine and histamine, which are more adsorption controlled to the CNS surface than CFME surfaces [39-43]. CNSMEs also promote the detection of secondary products for adenosine, and thus the ratio for the secondary oxidation peaks is larger at CNSMEs. Interestingly, histamine detection is also more sensitive at CNSMEs, but the secondary peak is not as enhanced, so the adsorption strength may not be increased for its secondary products.

Antifouling properties are also important for biological experiments. Previous studies have shown that nanoscale surface engineering can prevent biofouling, particularly by bacteria and cells that adhere to smooth surfaces [54]. Ross' group showed that rough surfaces, such as CNT yarns, have less serotonin fouling than smoother surfaces, such as CFMEs, and defect sites lead to less biofouling [44]. Histamine fouls electrode surfaces by forming dimers and then polymers through a free radical polymerization, which will attach to the electrode via π - π stacking between benzene rings in the neurochemicals and basal planes of graphene [26]. CNSs have less basal planes than CFs [18], as shown by Raman spectroscopy, which would

reduce the basal plane area for histamine polymers to attach to the surface by π - π stacking [25, 26, 42, 55]. In addition, the application of the adenosine waveform breaks carbon bonds, reduces fouling of polymers by breaking their bonds, and makes a more reactive surface [1, 4, 44, 56]. Wightman's group showed that breaking carbon bonds by scanning to higher potentials increased adsorption of cation neurotransmitters while reducing polymer fouling by renewing the surface [57]. While polymers would have less basal planes to stack on, individual cationic neurochemical adsorption is favored at edge planes and oxygen defect sites, and so edge planes increase the sensitivity for the small molecules while reducing polymer fouling [44].

CNSMEs are also resistant to biofouling. The more hydrophilic nature of the CNSs interferes with the hydrophobic effect, which contributes to the biofouling from protein [44]. Here we demonstrate less biofouling by tissue proteins at CNS electrodes scanned to high potentials, consistent with other studies that found that treatments that increase surface roughness or increase surface oxygen groups of carbon nanomaterials also reduce tissue fouling [58]. While we used 25 μ m diameter electrodes here, wires can be etched to a micron and coated with CNSs [17], and so CNS electrodes could be good for measurements in small organisms with limited tissue damage. CNSs could also be grown on smaller diameter carbon-fiber microelectrodes for in vivo applications. Thus, these studies prove CNS electrodes are useful for more analytes than just dopamine and catecholamines and should be used to reduce biofouling and increase selectivity in monitoring of high oxidation potential analytes.

2.5 Conclusions

CNS electrodes are beneficial for detection of high oxidation potential analytes, including adenosine, hydrogen peroxide, and histamine. The surface characteristics of CNSs are beneficial for the electrochemical performance, as increased surface roughness and abundant oxide groups on defect sites improve adsorption. CNSMEs showed promising enhancement of detection sensitivities for cationic analytes such as adenosine and histamine, and even an

improvement for the small molecule hydrogen peroxide. CNSMEs are also useful because they had less fouling for histamine and less biofouling after being implanted in tissue. Thus, future studies could use CNSMEs *in vivo* to track neuromodulator changes during potential neurodegenerative diseases.

2.6 References

- (1) Huffman, M. L.; Venton, B. J. Electrochemical Properties of Different Carbon-Fiber Microelectrodes Using Fast-Scan Cyclic Voltammetry. *Electroanalysis* **2008**, *20* (22), 2422–2428. <https://doi.org/10.1002/elan.200804343>.
- (2) Ganesana, M.; Lee, S. T.; Wang, Y.; Venton, B. J. Analytical Techniques in Neuroscience: Recent Advances in Imaging, Separation, and Electrochemical Methods. *Anal. Chem.* **2017**, *89* (1), 314–341. <https://doi.org/10.1021/acs.analchem.6b04278>.
- (3) Huffman, M. L.; Venton, B. J. Carbon-Fiber Microelectrodes for in Vivo Applications. *The Analyst* **2009**, *134* (1), 18–24. <https://doi.org/10.1039/B807563H>.
- (4) Venton, B. J.; Cao, Q. Fundamentals of Fast-Scan Cyclic Voltammetry for Dopamine Detection. *Analyst* **2020**, *145*, 1158–1168. <https://doi.org/10.1039/C9AN01586H>.
- (5) Yang, C.; Denno, M. E.; Pyakurel, P.; Venton, B. J. Recent Trends in Carbon Nanomaterial-Based Electrochemical Sensors for Biomolecules: A Review. *Anal. Chim. Acta* **2015**, *887*, 17–37. <https://doi.org/10.1016/j.aca.2015.05.049>.
- (6) Cao, Q.; Puthongkham, P.; Venton, B. J. Review: New Insights into Optimizing Chemical and 3D Surface Structures of Carbon Electrodes for Neurotransmitter Detection. *Anal. Methods* **2019**, *11* (3), 247–261. <https://doi.org/10.1039/c8ay02472c>.
- (7) Yang, C.; Wang, Y.; Jacobs, C. B.; Ivanov, I. N.; Venton, B. J. O₂ Plasma Etching and Antistatic Gun Surface Modifications for CNT Yarn Microelectrode Improve Sensitivity and Antifouling Properties. *Anal. Chem.* **2017**, *89* (10), 5605–5611. <https://doi.org/10.1021/acs.analchem.7b00785>.
- (8) Jacobs, C. B.; Ivanov, I. N.; Nguyen, M. D.; Zestos, A. G.; Venton, B. J. High Temporal Resolution Measurements of Dopamine with Carbon Nanotube Yarn Microelectrodes. *Anal. Chem.* **2014**, *86* (12), 5721–5727. <https://doi.org/10.1021/ac404050t>.
- (9) Schmidt, A. C.; Wang, X.; Zhu, Y.; Sombers, L. A. Carbon Nanotube Yarn Electrodes for Enhanced Detection of Neurotransmitter Dynamics in Live Brain Tissue. *ACS Nano* **2013**, *7* (9), 7864–7873. <https://doi.org/10.1021/nn402857u>.
- (10) Wang, J. Carbon-Nanotube Based Electrochemical Biosensors: A Review. *Electroanalysis* **2005**, *17* (1), 7–14. <https://doi.org/10.1002/elan.200403113>.
- (11) Wang, J.; Deo, R. P.; Poulin, P.; Mangey, M. Carbon Nanotube Fiber Microelectrodes. *J. Am. Chem. Soc.* **2003**, *125* (48), 14706–14707. <https://doi.org/10.1021/ja037737j>.
- (12) Zhang, X.; Li, Q.; Tu, Y.; Li, Y.; Coulter, J. Y.; Zheng, L.; Zhao, Y.; Jia, Q.; Peterson, D. E.; Zhu, Y. Strong Carbon-Nanotube Fibers Spun from Long Carbon-Nanotube Arrays. *Small* **2007**, *3* (2), 244–248. <https://doi.org/10.1002/sml.200600368>.
- (13) Yang, C.; Jacobs, C. B.; Nguyen, M. D.; Ganesana, M.; Zestos, A. G.; Ivanov, I. N.; Puretzky, A. A.; Rouleau, C. M.; Geohegan, D. B.; Venton, B. J. Carbon Nanotubes Grown on Metal Microelectrodes for the Detection of Dopamine. *Anal. Chem.* **2016**, *88* (1), 645–652. <https://doi.org/10.1021/acs.analchem.5b01257>.
- (14) G. Zestos, A.; Yang, C.; B. Jacobs, C.; Hensley, D.; Jill Venton, B. Carbon Nanospikes Grown on Metal Wires as Microelectrode Sensors for Dopamine. *Analyst* **2015**, *140* (21), 7283–7292. <https://doi.org/10.1039/C5AN01467K>.

- (15) Sheridan, L. B.; Hensley, D. K.; Lavrik, N. V.; Smith, S. C.; Schwartz, V.; Liang, C.; Wu, Z.; Meyer, H. M.; Rondinone, A. J. Growth and Electrochemical Characterization of Carbon Nanospire Thin Film Electrodes. *J. Electrochem. Soc.* **2014**, *161* (9), H558. <https://doi.org/10.1149/2.0891409jes>.
- (16) Song, Y.; Peng, R.; Hensley, D. K.; Bonnesen, P. V.; Liang, L.; Wu, Z.; Meyer III, H. M.; Chi, M.; Ma, C.; Sumpter, B. G.; Rondinone, A. J. High-Selectivity Electrochemical Conversion of CO₂ to Ethanol Using a Copper Nanoparticle/N-Doped Graphene Electrode. *ChemistrySelect* **2016**, *1* (19), 6055–6061. <https://doi.org/10.1002/slct.201601169>.
- (17) Cao, Q.; Shao, Z.; Hensley, D.; Jill Venton, B. Carbon Nanospire Coated Nanoelectrodes for Measurements of Neurotransmitters. *Faraday Discuss.* **2022**, *233* (0), 303–314. <https://doi.org/10.1039/D1FD00053E>.
- (18) Cao, Q.; Hensley, D. K.; Lavrik, N. V.; Venton, B. J. Carbon Nanospikes Have Better Electrochemical Properties than Carbon Nanotubes Due to Greater Surface Roughness and Defect Sites. *Carbon* **2019**, *155*, 250–257. <https://doi.org/10.1016/j.carbon.2019.08.064>.
- (19) Jacobs, C. B.; Vickrey, T. L.; Venton, B. J. Functional Groups Modulate the Sensitivity and Electron Transfer Kinetics of Neurochemicals at Carbon Nanotube Modified Microelectrodes. *The Analyst* **2011**, *136* (17), 3557. <https://doi.org/10.1039/c0an00854k>.
- (20) Unwin, P. R.; Güell, A. G.; Zhang, G. Nanoscale Electrochemistry of Sp² Carbon Materials: From Graphite and Graphene to Carbon Nanotubes. *Acc. Chem. Res.* **2016**, *49* (9), 2041–2048. <https://doi.org/10.1021/acs.accounts.6b00301>.
- (21) Puthongkham, P.; Yang, C.; Venton, B. J. Carbon Nanohorn-Modified Carbon Fiber Microelectrodes for Dopamine Detection. *Electroanalysis* **2018**, *30* (6), 1073–1081. <https://doi.org/10.1002/elan.201700667>.
- (22) Puthongkham, P.; Venton, B. J. Recent Advances in Fast-Scan Cyclic Voltammetry. *Analyst* **2020**, *145*, 1087–1102. <https://doi.org/10.1039/C9AN01925A>.
- (23) Swamy, B. E. K.; Venton, B. J. Subsecond Detection of Physiological Adenosine Concentrations Using Fast-Scan Cyclic Voltammetry. *Anal. Chem.* **2007**, *79* (2), 744–750. <https://doi.org/10.1021/ac061820i>.
- (24) Sanford, A. L.; Morton, S. W.; Whitehouse, K. L.; Oara, H. M.; Lugo-Morales, L. Z.; Roberts, J. G.; Sombers, L. A. Voltammetric Detection of Hydrogen Peroxide at Carbon Fiber Microelectrodes. *Anal. Chem.* **2010**, *82* (12), 5205–5210. <https://doi.org/10.1021/ac100536s>.
- (25) Sarada, B. V.; Rao, T. N.; Tryk, D. A.; Fujishima, A. Electrochemical Oxidation of Histamine and Serotonin at Highly Boron-Doped Diamond Electrodes. *Anal. Chem.* **2000**, *72* (7), 1632–1638. <https://doi.org/10.1021/ac9908748>.
- (26) Puthongkham, P.; Lee, S. T.; Venton, B. J. Mechanism of Histamine Oxidation and Electropolymerization at Carbon Electrodes. *Anal. Chem.* **2019**, *91* (13), 8366–8373. <https://doi.org/10.1021/acs.analchem.9b01178>.
- (27) Manjunath, S.; Sakhare, P. M. Adenosine and Adenosine Receptors: Newer Therapeutic Perspective. *Indian J. Pharmacol.* **2009**, *41* (3), 97–105. <https://doi.org/10.4103/0253-7613.55202>.
- (28) Bjorness, T. E.; Greene, R. W. Adenosine and Sleep. *Curr. Neuropharmacol.* **2009**, *7* (3), 238–245. <https://doi.org/10.2174/157015909789152182>.

- (29) Cunha, R. A. Adenosine as a Neuromodulator and as a Homeostatic Regulator in the Nervous System: Different Roles, Different Sources and Different Receptors. *Neurochem. Int.* **2001**, *38* (2), 107–125. [https://doi.org/10.1016/S0197-0186\(00\)00034-6](https://doi.org/10.1016/S0197-0186(00)00034-6).
- (30) Ross, A. E.; Venton, B. J. Nafion–CNT Coated Carbon-Fiber Microelectrodes for Enhanced Detection of Adenosine. *The Analyst* **2012**, *137* (13), 3045. <https://doi.org/10.1039/c2an35297d>.
- (31) Pajski, M. L.; Venton, B. J. Adenosine Release Evoked by Short Electrical Stimulations in Striatal Brain Slices Is Primarily Activity Dependent. *ACS Chem. Neurosci.* **2010**, *1* (12), 775–787. <https://doi.org/10.1021/cn100037d>.
- (32) Nguyen, M. D.; Venton, B. J. Fast-Scan Cyclic Voltammetry for the Characterization of Rapid Adenosine Release. *Comput. Struct. Biotechnol. J.* **2015**, *13*, 47–54. <https://doi.org/10.1016/j.csbj.2014.12.006>.
- (33) Pajski, M. L.; Venton, B. J. The Mechanism of Electrically Stimulated Adenosine Release Varies by Brain Region. *Purinergic Signal.* **2013**, *9* (2), 167–174. <https://doi.org/10.1007/s11302-012-9343-2>.
- (34) Roberts, J. G.; Voinov, M. A.; Schmidt, A. C.; Smirnova, T. I.; Sombers, L. A. The Hydroxyl Radical Is a Critical Intermediate in the Voltammetric Detection of Hydrogen Peroxide. *J. Am. Chem. Soc.* **2016**, *138* (8), 2516–2519. <https://doi.org/10.1021/jacs.5b13376>.
- (35) Halliwell, B. Oxidative Stress and Neurodegeneration: Where Are We Now? *J. Neurochem.* **2006**, *97* (6), 1634–1658. <https://doi.org/10.1111/j.1471-4159.2006.03907.x>.
- (36) Avshalumov, M. V.; Chen, B. T.; Koós, T.; Tepper, J. M.; Rice, M. E. Endogenous Hydrogen Peroxide Regulates the Excitability of Midbrain Dopamine Neurons via ATP-Sensitive Potassium Channels. *J. Neurosci.* **2005**, *25* (17), 4222–4231. <https://doi.org/10.1523/JNEUROSCI.4701-04.2005>.
- (37) Hall, S. B.; Khudaish, E. A.; Hart, A. L. Electrochemical Oxidation of Hydrogen Peroxide at Platinum Electrodes. Part 1. An Adsorption-Controlled Mechanism. *Electrochimica Acta* **1998**, *43* (5), 579–588. [https://doi.org/10.1016/S0013-4686\(97\)00125-4](https://doi.org/10.1016/S0013-4686(97)00125-4).
- (38) Han, J.-H.; Boo, H.; Park, S.; Chung, T. D. Electrochemical Oxidation of Hydrogen Peroxide at Nanoporous Platinum Electrodes and the Application to Glutamate Microsensor. *Electrochimica Acta* **2006**, *52* (4), 1788–1791. <https://doi.org/10.1016/j.electacta.2005.12.060>.
- (39) Sanford, A. L.; Morton, S. W.; Whitehouse, K. L.; Oara, H. M.; Lugo-Morales, L. Z.; Roberts, J. G.; Sombers, L. A. Voltammetric Detection of Hydrogen Peroxide at Carbon Fiber Microelectrodes. *Anal. Chem.* **2010**, *82* (12), 5205–5210. <https://doi.org/10.1021/ac100536s>.
- (40) Hashemi, P.; Dankoski, E. C.; Wood, K. M.; Ambrose, R. E.; Wightman, R. M. In Vivo Electrochemical Evidence for Simultaneous 5-HT and Histamine Release in the Rat Substantia Nigra Pars Reticulata Following Medial Forebrain Bundle Stimulation. *J. Neurochem.* **2011**, *118* (5), 749–759. <https://doi.org/10.1111/j.1471-4159.2011.07352.x>.
- (41) Pihel, K.; Hsieh, S.; Jorgenson, J. W.; Wightman, R. M. Quantal Corelease of Histamine and 5-Hydroxytryptamine from Mast Cells and the Effects of Prior Incubation. *Biochemistry* **1998**, *37* (4), 1046–1052. <https://doi.org/10.1021/bi9714868>.
- (42) Liu, J.; Cao, Y. An Electrochemical Sensor Based on an Anti-Fouling Membrane for the Determination of Histamine in Fish Samples. *Anal. Methods* **2021**, *13* (5), 685–694. <https://doi.org/10.1039/D0AY01901A>.

- (43) Eivazzadeh-Keihan, R.; Bahojb Noruzi, E.; Chidar, E.; Jafari, M.; Davoodi, F.; Kashtiaray, A.; Ghafori Gorab, M.; Masoud Hashemi, S.; Javanshir, S.; Ahangari Cohan, R.; Maleki, A.; Mahdavi, M. Applications of Carbon-Based Conductive Nanomaterials in Biosensors. *Chem. Eng. J.* **2022**, *442*, 136183. <https://doi.org/10.1016/j.cej.2022.136183>.
- (44) Weese, M. E.; Krevh, R. A.; Li, Y.; Alvarez, N. T.; Ross, A. E. Defect Sites Modulate Fouling Resistance on Carbon-Nanotube Fiber Electrodes. *ACS Sens.* **2019**, *4* (4), 1001–1007. <https://doi.org/10.1021/acssensors.9b00161>.
- (45) Ulyanov, N. B.; James, T. L. RNA Structural Motifs That Entail Hydrogen Bonds Involving Sugar–Phosphate Backbone Atoms of RNA. *New J. Chem.* **2010**, *34* (5), 910. <https://doi.org/10.1039/b9nj00754g>.
- (46) Li, Y.; Weese, M. E.; Cryan, M. T.; Ross, A. E. Amine-Functionalized Carbon-Fiber Microelectrodes for Enhanced ATP Detection with Fast-Scan Cyclic Voltammetry. *Anal. Methods* **2021**, *13* (20), 2320–2330. <https://doi.org/10.1039/D1AY00089F>.
- (47) Żeglin´ski, J.; Piotrowski, G. P.; Piękos´, R. A Study of Interaction between Hydrogen Peroxide and Silica Gel by FTIR Spectroscopy and Quantum Chemistry. *J. Mol. Struct.* **2006**, *794* (1–3), 83–91. <https://doi.org/10.1016/j.molstruc.2006.01.043>.
- (48) Engdahl, A.; Nelander, B. The Structure of the Water–Hydrogen Peroxide Complex. A Matrix Isolation Study. *Phys. Chem. Chem. Phys.* **2000**, *2* (18), 3967–3970. <https://doi.org/10.1039/B005861K>.
- (49) Lewandowski, D.; Bajerlein, D.; Schroeder, G. Adsorption of Hydrogen Peroxide on Functionalized Mesoporous Silica Surfaces. *Struct. Chem.* **2014**, *25* (5), 1505–1512. <https://doi.org/10.1007/s11224-014-0428-0>.
- (50) Luque, G. L.; Rojas, M. I.; Rivas, G. A.; Leiva, E. P. M. The Origin of the Catalysis of Hydrogen Peroxide Reduction by Functionalized Graphene Surfaces: A Density Functional Theory Study. *Electrochimica Acta* **2010**, *56* (1), 523–530. <https://doi.org/10.1016/j.electacta.2010.09.016>.
- (51) Majidi, R.; Karami, A. R. Detection of Hydrogen Peroxide with Graphyne. *Physica E-low-dimensional Systems & Nanostructures* **2013**, *54*, 177–180. <https://doi.org/10.1016/j.physe.2013.06.029>.
- (52) Omid, M. H.; Soleymanabadi, H.; Bagheri, Z. Adsorption and Dissociation of Hydrogen Peroxide on the Defected Carbon Nanotubes. *Struct. Chem.* **2015**, *26* (2), 485–490. <https://doi.org/10.1007/s11224-014-0513-4>.
- (53) Nguyen, M. D.; Lee, S. T.; Ross, A. E.; Ryals, M.; Choudhry, V. I.; Venton, B. J. Characterization of Spontaneous, Transient Adenosine Release in the Caudate-Putamen and Prefrontal Cortex. *PLOS ONE* **2014**, *9* (1), e87165. <https://doi.org/10.1371/journal.pone.0087165>.
- (54) Graham, M. V.; Cady, N. C. Nano and Microscale Topographies for the Prevention of Bacterial Surface Fouling. *Coatings* **2014**, *4* (1), 37–59. <https://doi.org/10.3390/coatings4010037>.
- (55) Khot, G.; Shirtcliffe, N.; Celikel, T. *Simultaneous Detection of Dopamine and Serotonin with Carbon-Based Electrodes*; preprint; Biochemistry, 2021. <https://doi.org/10.1101/2021.08.31.458352>.

(56) Cao, Q.; Lucktong, J.; Shao, Z.; Chang, Y.-Y.; B. Jill Venton. Electrochemical Treatment in KOH Renews and Activates Carbon Fiber Microelectrode Surfaces. *Analytical and Bioanalytical Chemistry* **2021**, 413 (27), 6737–6746.

<https://doi.org/10.1007/s00216-021-03539-6>.

(57) Takmakov, P.; Zachek, M. K.; Keithley, R. B.; Walsh, P. L.; Donley, C.; McCarty, G. S.; Wightman, R. M. Carbon Microelectrodes with a Renewable Surface. *Anal. Chem.* **2010**, 82 (5), 2020–2028. <https://doi.org/10.1021/ac902753x>.

(58) Yang, C.; Wang, Y.; Jacobs, C. B.; Ivanov, I. N.; Venton, B. J. O₂ Plasma Etching and Antistatic Gun Surface Modifications for CNT Yarn Microelectrode Improve Sensitivity and Antifouling Properties. *Anal. Chem.* **2017**, 89 (10), 5605–5611. <https://doi.org/10.1021/acs.analchem.7b00785>.

Chapter 3

Pyrolyzed Parylene-N for *In Vivo* Electrochemical Detection of Neurotransmitters

Abstract

Carbon electrodes are typically used for *in vivo* dopamine detection, and new types of electrodes and customized fabrication methods will facilitate new applications. Parylene is an insulator that can be deposited in a thin layer on a substrate, and then pyrolyzed to carbon to enable its use as an electrode. However, pyrolyzed parylene has not been used for the real-time detection of neurochemicals with fast-scan cyclic voltammetry. In this work, we deposited thin layers of parylene-N (PN) on metal wires, and then pyrolyzed them to carbon with high temperatures in a rapid thermal processor (RTP). Different masses of PN, 1 g, 6 g, and 12 g, were deposited to vary the thickness. RTP-PN (6 g) produced 194 nm layer carbon thickness and had optimal electrochemical stability. Pyrolyzed parylene-N modified electrodes (PPNMEs) were characterized for electrochemical detection of dopamine, serotonin, and adenosine. Background-normalized currents at PPNMEs were about 2 times larger than carbon-fiber microelectrodes (CFMEs). Rich defect sites and oxygen functional groups promoted neurochemical adsorption for cationic neurotransmitters. PPNMEs resisted fouling from serotonin polymer formation. PPNMEs were used *in vivo* to detect stimulated dopamine release and monitor spontaneous adenosine release. Pyrolyzed parylene is a sensitive and fouling-resistant thin-film carbon electrode that could be used in the future for making customized electrodes and devices.

3.1 Introduction

Carbon-fiber microelectrodes (CFMEs) are commonly used for electrochemical detection of monoamine neurotransmitters with fast-scan cyclic voltammetry (FSCV). CFMEs are applied for *in vivo* or *in vitro* tracking of neurochemicals because of the biocompatibility and relatively small diameter (~7 μm). However, different types of carbon electrodes have been developed to enhance electrochemical properties for many applications. For example, carbon nanotubes (CNTs) in CNT yarn microelectrodes efficiently trap neurochemicals because of thin-layer effects.¹⁻³ Carbon nanospikes (CNSs) are deposited on niobium (Nb) wires and utilized to promote analyte adsorption and resist fouling.⁴⁻⁶ Pyrolyzed photoresist electrodes were developed to take advantage of thin polymer films deposited on wires or other substrates to make arrays.⁷ Tour's group demonstrated laser pyrolysis of polymers to make electrode materials.^{8,9} Many pyrolyzed carbon electrodes are made from polyimide, a commercially available polymer, which is usually coated on silicon (Si) wafer via spin coating.¹⁰⁻¹² However, it is difficult to make a uniform coating using spin coating on a cylinder electrode.^{13,14} Here, we developed pyrolyzed carbon electrodes from thin films of parylene, a biocompatible, insulating polymer, and showed they can be used with FSCV for neurotransmitter detection

Parylene, poly(p-xylene), is a benzene-rich polymer with chemical inertness, flexibility, and transparency and is usually used to insulate electronics.¹⁵⁻¹⁷ Parylene can be coated on different substrates via chemical vapor deposition (CVD), which guarantees uniform coating and thin deposition thickness.¹⁸⁻²⁰ Many micro-electromechanical systems (MEMS) are insulated with parylene to form a thin film for cell co-culture and tissue barrier models.^{21,22} Parylene-C, which contains chlorine, and parylene-N, which does not, are the common forms of parylene, and other derivatives include parylene-D, VT4, and AF4.²³⁻²⁵ The Baker group previously fabricated pyrolyzed parylene-C electrodes for electrochemical detection with cyclic voltammetry (CV).²⁶ However, pyrolyzed parylene has not been used with fast-scan cyclic voltammetry (FSCV) or to make electrodes for *in vivo* testing. We deposited parylene-N (PN) on etched Nb

wires via CVD and used rapid thermal processing (RTP) to pyrolyze the parylene into uniformly coated thin film of carbon.

Many monoamine neurochemicals are electroactive, including dopamine (DA), serotonin, and adenosine (AD). Dopamine is a neurotransmitter that regulates movement and is involved in reward pathways.^{27,28} Serotonin is an important neurotransmitter regulating mood and depression, but is difficult to detect electrochemically because it undergoes polymerization after electrooxidation, which can foul the electrode surface via π - π stacking.^{29,30} Adenosine (AD) is a neuromodulator involved in regulating vasodilation and sleep, and spontaneous transients have been measured which are important in diseases such as ischemia.^{6,31–33} Thus, developing new electrodes for neurotransmitters involves optimizing sensitivity for different molecules and reducing fouling to enable sensitive, long-term *in vivo* monitoring.

In this work, we developed a protocol to deposit PN on Nb wires and then pyrolyze it to carbon with RTP for use as an electrode to detect neurotransmitters. Surface characterization shows that defect rich carbon is produced, with a high amount of oxygen functional groups. Pyrolyzed parylene-N modified electrodes (PPNMEs) were characterized for electrochemical detection of neurochemicals DA, serotonin, and AD with FSCV. Oxygen functional groups promote analyte adsorption to electrode surface and prevent serotonin fouling. The pyrolyzed parylene-N electrodes are useful for *in vivo* detection of dopamine and adenosine, showing it is a good carbon material for general detection of neurotransmitters *in vivo*. Thus, pyrolyzed parylene is an excellent method to make a thin-film carbon electrode that is compatible with FSCV and could be used in the future to make customized electrodes and microdevices.

3.2 Experimental Methods

3.2.1 Chemicals and materials

Stock solutions (10 mM) were made for dopamine, serotonin, and adenosine (ThermoFisher Scientific, Waltham, WA) in perchloric acid (0.1 M). Dilute solutions for testing

(1-100 μM) were made in phosphate-buffered saline (PBS) buffer pH 7.4 (131.25 mM NaCl, 3.25 mM KCl, 1.2 mM CaCl_2 , 1.25 mM NaH_2PO_4 , 1.2 mM MgCl_2).

3.2.2 Parylene deposition and pyrolysis

Niobium wires (diameter 50 μm , Advent Research Materials, Eynsham, Oxford) were etched to 600 nm in 4 M NaOH by applying with DC voltage, 2 V for 10 min. After coating, the wires were rinsed with water and isopropanol. PN was coated on etched wires using an SCS parylene coater (PDS 2010, IN). Di-para-xylene powder, as precursor, was vaporized in the parylene coater chamber at 150 $^\circ\text{C}$ under vacuum. Pyrolysis of the dimer was achieved with the application of high temperature, 650 $^\circ\text{C}$, to form para-xylene, the monomer state, and those monomers then form the poly(para-xylene) structure, called parylene. Parylene coating thickness can be adjusted by loading with different masses, 1 g, 6 g, and 12 g, during vapor deposition. Silicon (Si) wafers, platinum (Pt) circuit chips, and Nb wires were parylene coated in an SCS parylene coater (PDS 2010, IN). After parylene coating, wires and silicon wafers were treated for pre-annealing on a microhotplate at 350 $^\circ\text{C}$ for 10 min in air atmosphere. To carbonize the PN coating, a rapid thermal processor (RTP) (First nano, NY) was used with these steps: (1) 600 $^\circ\text{C}$ in argon atmosphere at 9 Torr for 10 min, (2) 950 $^\circ\text{C}$ in argon atmosphere at 1 Torr for 10 min. RTP-PN Si wafers were used for Raman and XPS characterizations because they are flat. The conductivity test was conducted on RTP-PN Pt circuit chips. RTP-PN Nb wires were inserted into glass capillaries for insulation for a final exposed length of 50 μm for dopamine and serotonin and 100 μm for flow cell and *in vivo* adenosine and 5-min epoxy was used to seal the gap (J-B weld, Sulphur Springs, TX).

3.2.3 Construction of CFMEs

7 μm -diameter carbon fibers (CFs) (T650-35, Cytec, Woodland Park, NJ) were inserted into glass capillaries. The capillaries were pulled in a PE-21 pipette puller (Setagaya-ku, Tokyo, Japan) and two needle-shaped microelectrodes were made. Electrodes were cut to an exposed CF length around 50-100 μm . CFs were dipped for 30 s in a mixture of Epon Resin 828

(Danbury, CT) with 14% (w/w) m-phenylenediamine hardener (Acros Organics, Morris Plains, NJ) to seal the gap between glass capillaries. Microelectrodes were rinsed in acetone for 5 s to remove excessive epoxy. CF microelectrodes (CFMEs) were left on the benchtop overnight to air dry the epoxy at room temperature and then cured in an oven at 100 °C for 2 h and 150 °C overnight.

3.2.4 Instrumentation

CVD of PN on Nb wires was accomplished with a parylene coater (SCS, Indianapolis, IN). Collection of scanning electron microscopy images was achieved with Merlin field emission SEM (Zeiss, Thornwood, NY) and FEI Quanta 650 SEM (ThermoFisher Scientific, Waltham, MA) with applied accelerating voltage, 20 kV, on secondary electron detector. Analysis of graphitic features was performed by InVia Confocal Raman microscopy (Renishaw, Gloucestershire, United Kingdom). Surface characterization of elemental and functional group compositions was performed with an X-ray photoelectron spectrometer (Physical Electronics, Chanhassen, MN). Parylene thickness quantification was performed with a profilometer (KLA Tencor P-17, Milpitas, CA).

A ChemClamp potentiostat (Dagan, Minneapolis, MN) with a 1 M Ω -resistance headstage was used to collect FSCV data with a silver/silver chloride reference electrode (Pomona Electronics, Everett, WA). Silver wire was chlorized in concentrated HCl solution with the application of 4 V. Electrochemical data was collected by applying a triangular dopamine waveform, from -0.4 V to 1.3 V, a scan rate of 400 V/s and a frequency of 10 Hz. FSCV data analysis was performed on HDCV software (Department of Chemistry, University of North Carolina at Chapel Hill). Neurochemical solutions were flowed through a flow cell at 2 mL/min with the use of a six-port, stainless steel HPLC loop injector with an air actuator (VICI Valco Instruments, Houston, TX). 1 M KCl was injected into glass capillaries to provide an electrical connection between the potentiostat headstage and the electrodes.

3.2.5 Background-current subtraction

Due to the high scan rate of FSCV, 400 V/s, background currents are usually high, which makes the Faradaic current not visible. Therefore, background-current subtraction was performed while detecting neurochemicals to get final current response. Because of analyte adsorption on the electrode surface, there could be a small background-subtraction error present when obtaining final CV graphs.

3.2.6 *In vivo* Measurements

All animal experiments were performed as approved by the Animal Care and Use Committee (ACUC) of the University of Virginia. Rats (Charles River) were anesthetized with urethane (5% saline solution, 0.3 ml/100 g i.p.) before each experiment. The rectal and core body temperature was maintained at 37 °C using an isothermal pad (Delta Phase Pad; Braintree Scientific, Braintree, MA, USA). Hourly checks (paw pinch) were made of respiration and depth of anesthesia. During surgery, a local anesthetic (bupivacaine) was used on exposed skin and muscle tissue.

The rat was placed in a stereotaxic frame, and holes were drilled precisely in the skull to place the stimulating electrodes, working electrodes, reference electrodes, and according to the atlas of Paxinos and Watson.³⁴ Specifically, the carbon-fiber working electrode was lowered into the NAc core (+1.3 mm anterior-posterior [AP], +2.0 mm medial-lateral [ML], -7.1 mm dorsal-ventral [DV]), and the bipolar stimulating electrode (Plastics One, Roanoke, VA, USA) was lowered to the VTA (-4.7 mm AP, +0.9 mm ML, -8.5 mm DV). The dorsoventral coordinate of the electrodes was adjusted to detect the maximum amount of stimulated dopamine release. An Ag/AgCl wire reference electrode was inserted on the contralateral side of the brain. To electrically stimulate dopamine, a constant biphasic current stimulus at +300 μ A, 2 ms, 24 pulses was delivered to the VTA by a bipolar stimulating electrode (Plastics One, Inc., Roanoke, VA, USA). Spontaneous adenosine release was measured by applying the waveform with no electrical stimulation. After each experiment, animals were euthanized using guillotine (World Precision Instruments, Sarasota, Florida, USA).

3.2.7 Brain Slice Preparation

All animal experiments were performed following the approved protocols by the Animal Care and Use Committee (ACUC) of the University of Virginia. Isoflurane was used to anesthetize 5-8 weeks old wide-type C57BL/6 mouse that was decapitated quickly (Jackson Lab). aCSF was oxygenated (95% O₂, 5% CO₂) and held at 0-5 °C to recover the brain after being removed. The slicing stage held the brain and a vibratome (Leica VT1000S, Bannockburn, IL, USA) was used to prepare coronal section slices (400 μm). Oxygenated aCSF (34 °C) in a water bath was utilized to equilibrate slices with caudate putamen. After transferring slices to the recording chamber, PPNMEs were inserted into approximately 75 μm deep into the tissue and then equilibrated for 10-15 min. 2 mL/min was set as the flow rate to continuously perfuse oxygenated aCSF over the slice. Serotonin was stored in a glass capillary, which is close to the working electrode. A nanoliter injector (Nanoliter2020, World Precision Instrument, FL) was used to microinject a precise amount of serotonin and CV was recorded by HDCV software.

3.3 Results

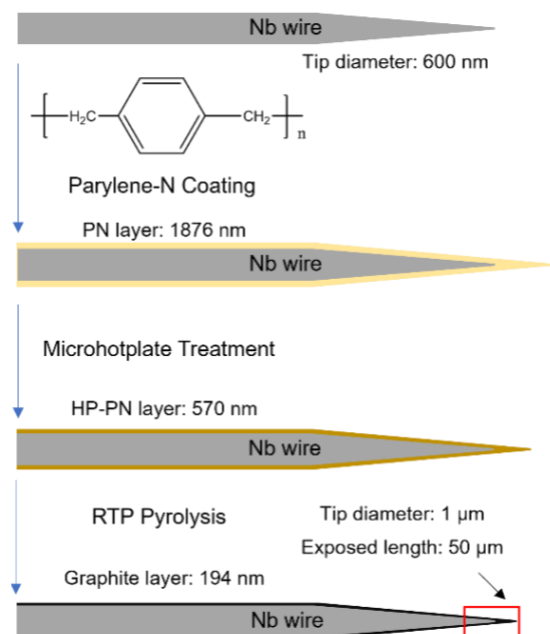


Figure 1. Overview of electrode fabrication. First parylene N is deposited on a wire, then the parylene is treated on a microhotplate, and finally pyrolysis is performed in a rapid thermal processor. The result is a thin film of graphite on the Nb wire. Thicknesses are given for 6 g of precursor.

The overall process of electrode fabrication is shown in Figure 1. PN was deposited on the etched Niobium (Nb) wire (with a tip diameter about 600 nm), by CVD and the coating thickness is about 1876 nm for 6 g of precursor. The PN-coated Nb wire was then heated on a microhotplate at 350°C (HP-PN), which shrinks the coating to 570 nm. Pyrolysis was performed using RTP at 600°C for 10 min and then 950°C for 10 min, parameters that were optimized for pyrolysis of 3D printed electrodes made of photoresist.³⁵ Future studies could examine the effect of pyrolysis parameters on electrochemical performance. The coating after RTP is conductive graphite and the final thickness is about 194 nm. Thus, a thin-film carbon electrode is achieved.

Precursor Mass (g)	Deposited Thickness (nm)	Thickness after Hot plate (nm)	Thickness after Pyrolysis (nm)
1	327 ± 21	122 ± 16	81 ± 10
6	1876 ± 96	570 ± 43	194 ± 20
12	3408 ± 158	867 ± 73	476 ± 35

Table 1. Parylene coating thickness with various masses at different stages of treatment. (Error is SEM, n=3).

We tested using different masses of parylene precursor, 1 g, 6 g, and 12 g, to understand the coating thickness and conductivity at various steps. The deposited parylene thickness on flat silicon wafers was consistent and ranged from 327 nm to 3.4 μm (Table 1) and are linear with the precursor mass (Fig. 2). Thicknesses should be similar on Nb wires, but it is difficult to measure on a wire. After heating on the microhotplate, the thickness of PN shrunk due to weight loss and varies from 122 nm to 867 nm. After pyrolysis of parylene with RTP, the thickness decreased even more and varied from 81 to 476 nm. Thus, this method leads to nanoscale films of carbon on the surface.

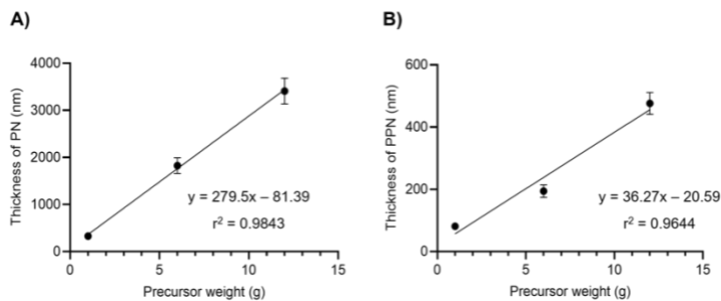


Figure 2. Thicknesses of PN and PPN plotted against PN precursor weight.

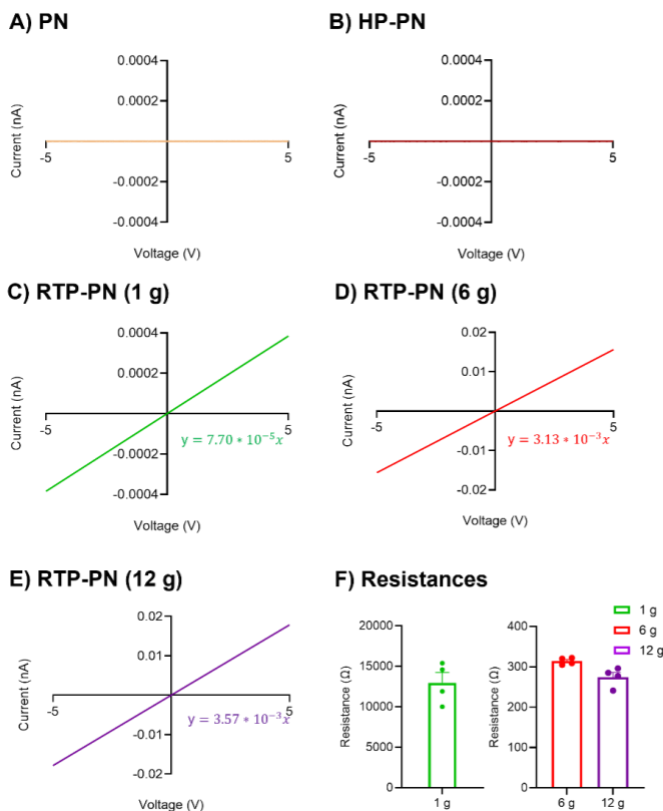


Figure 3. Electrical conductivity tests of (A) PN (yellow line) (B) HP-PN (brown line) (C) RTP-PN (1 g) (D) RTP-PN (6 g), and (E) RTP-PN (12 g) on Pt electric circuits (F) Resistances of RTP-PN (1 g), (6 g), and (12 g) (n=4, Error bars are SEM).

PN was deposited on a printed platinum (Pt) circuit with gaps between the electrodes and conductivity was measured by applying a voltage and measuring current. The slope was used to determine the electrical resistance of different polymers. PN is an insulating polymer that has no electrical conductivity because of the high resistance, and the plot in Fig. 3A confirms this. There is also no conductivity for HP-PN (Fig. 3B), so the polymer was not yet graphitized after hot plate treatment. The RTP-PN samples were conductive because the plots have a slope that corresponds to the resistance (slope=1/R, Fig. 3C, D, E). Thus, it takes a high temperature to carbonize the parylene and make it conductive. Conductivity at RTP-PN samples were measured multiple times (Fig. 4), and their resistances were calculated and shown in Fig. 3F. We simulated the circuit, with an RTP-PN (6 g) thickness, 194 nm, and resistance, 320 Ω , on COMSOL software. The estimated conductivity is about 3000 S/m, which is within the conductivity range of glassy carbon wires, 477-18100 S/m.³⁶ Glassy carbon generated when annealing at 850 °C for 4 hr possesses a conductivity of 3200 S/m, which is similar to RTP-PN (6 g).³⁷

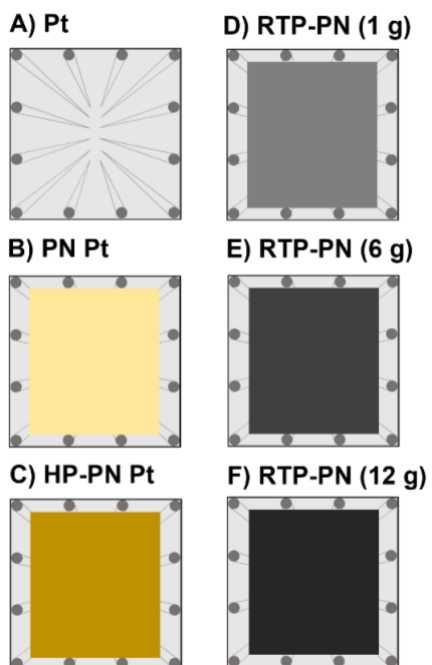


Figure 4 (A) Pt circuits (B) Pt circuits with PN (C) Pt circuits with HP-PN (D) Pt circuits with RTP-PN (1 g) (E) Pt circuits with RTP-PN (6 g) (F) Pt circuits with RTP-PN (12 g)

PN underwent volumetric shrinkage, which is about 89.7 % for PN-coated Nb wires (6 g), and structural reformation into graphite after high temperature annealing.^{26,38,39} The mechanism is likely high temperature breaking of carbon bonds and reaction of benzene rings to form graphite.⁴⁰ Tai's group saw similar changes in parylene-C (PC) coating thickness and resistivity when different temperatures were applied, 0 °C to 900 °C.³⁸ PC's resistivity dramatically decreased with raising temperature, especially above 500 °C, similar to what we observed in the conductivity test where conductivity increased after pyrolysis with RTP-annealing steps, at 600 °C and 950 °C. All RTP-PN with different amounts of precursor have similar conductivities, so we selected the RTP-PN (6 g) for further investigation. FSCV waveforms with switching potentials over 1.3 V are known to break down carbon material, so a slightly thicker film might be more stable over time (Fig. 5).⁴¹

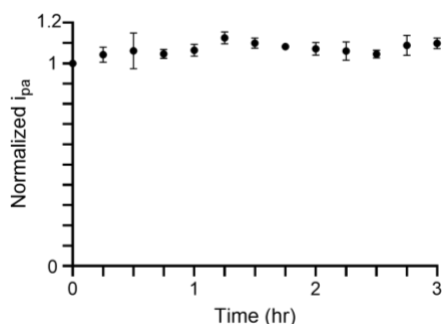


Figure 5. Stability test of PPNMEs.

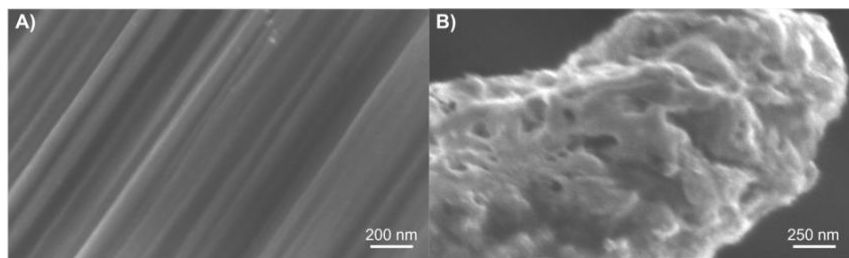


Figure 6. SEM images of (A) surface of CF and (B) surface of RTP-PN (6 g).

We characterized the surfaces by SEM (Fig. 6A and B, respectively). The CF structure is mainly smooth with some grooves. CFs are about 7 μm , and the overall diameter of PPNME on the etched Nb wire is about 1 μm (6 g deposited), which is smaller than CF. Therefore, the PPNME could be localized better in specific brain regions and cause less inflammation in tissue. The nanopores of PPNME are larger and deeper than the grooves on the CFME, which help restrict diffusion of neurochemicals that enter the nanopores.⁴² However, the pores are smaller than those on carbon nanotube yarn microelectrodes (CNTYMEs), and thus the effects of thin layer diffusion in nanopores at PPNMEs are expected to be more limited compared to carbon nanotube yarn microelectrodes (CNTYMEs).⁴²

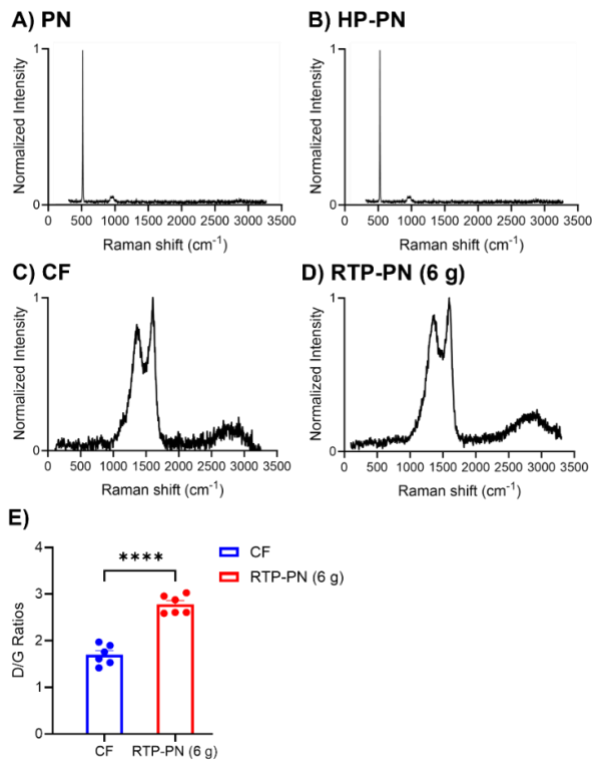


Figure 7. Raman spectra of (A) PN (B) HP-PN (C) CF and (D) RTP-PN (6 g) on Si wafer. The D, G, and 2D peaks are located at 1360 cm^{-1} , 1580 cm^{-1} , and 2860 cm^{-1} respectively (E) Bar graphs of D/G ratios of CF and RTP-PN (6 g) ($n=6$, t test, **** $p<0.0001$, Error bars are SEM).

Raman spectra were analyzed to study the graphitic features of all materials. The defect sites at the boundaries, such as sp^3 carbon, oxygen functional groups, or doping, generate a D band ($\sim 1360 \text{ cm}^{-1}$). Sp^2 graphitic carbons generate a G band ($\sim 1580 \text{ cm}^{-1}$), which is formed from basal planes.^{43–45} The 2D peak (2860 cm^{-1}) helps identify the material as graphene.^{46–48} Fig. 7A

and B show PN before and after heating at 350 °C on the microhotplate for 10 min. Heating on the hotplate does not cause graphitization as there is no obvious difference between Fig. 7A and B, which have only Si peaks from the wafer (522 cm^{-1} and 961 cm^{-1}) originated from Si wafer.⁴⁹ There are no graphitic features on either Raman spectra, which indicates that PN, a polymer, possesses no graphitic structure before RTP. RTP treatment induces full carbonization of PN, with the presence of D, G, and 2D peaks. The high temperature provides energy to change the polymer structure into multilayer graphene, which is confirmed by the presence of the 2D peak. The disorder level of carbon materials was determined by calculating the ratios of D peak and G peak areas, and they were 1.9 for CF and 2.6 for RTP-PN. A higher D/G ratio means that there are more defect sites on RTP-PN, and a decreased number of basal planes

might decrease pi stacking with molecules, which could improve anti-fouling behavior. Average D/G ratios of CF and RTP-PN (6 g) were plotted in a bar graph Fig. 7E.

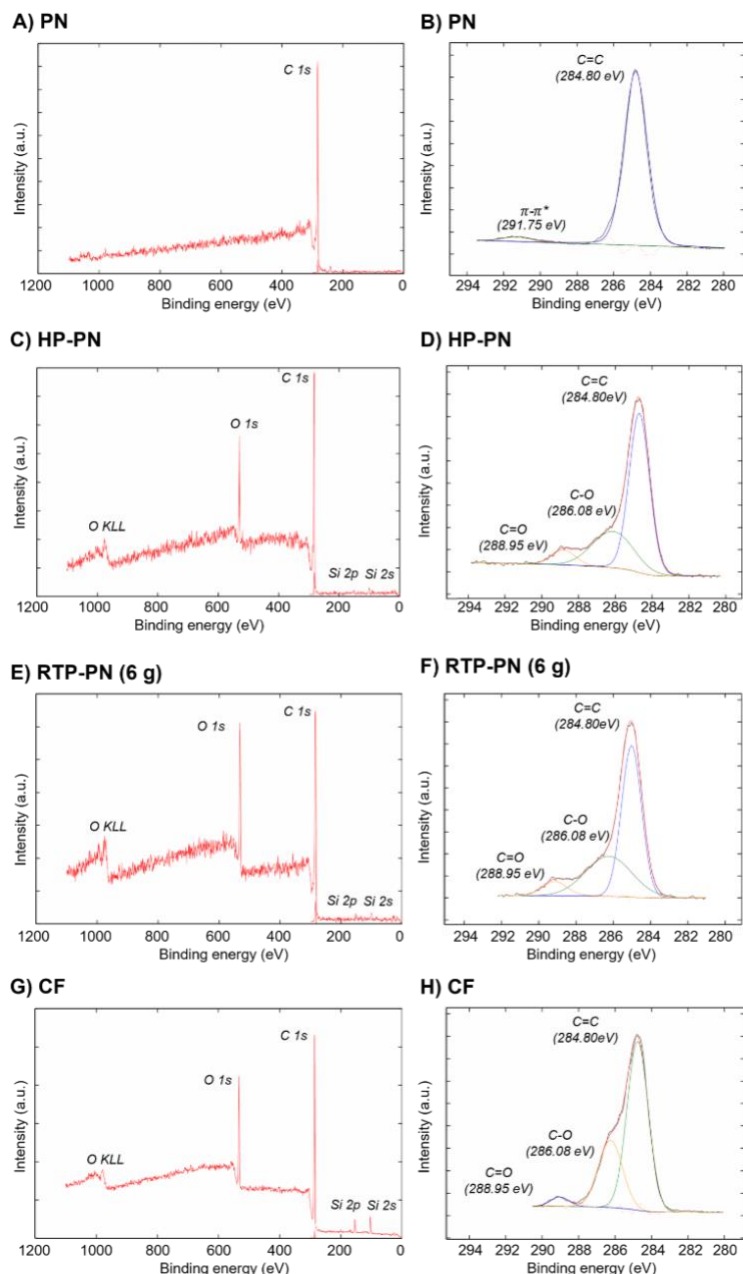


Figure 8. XPS analysis of elemental compositions (A) PN (C) HP-PN (E) RTP-PN (6 g) (G) CF and functional groups (B) PN (D) HP-PN (F) RTP-PN (6 g) (H) CF on Si wafers.

Raman spectroscopy shows that RTP-PN is a defect-rich graphitic material. XPS was utilized to characterize the specific surface elemental compositions and functional groups of pyrolyzed PN. PN is a benzene-rich polymer with no oxygen functional groups and π - π stacking originates from the polymer overlapping (Fig. 8A and B). After pre-annealing PN with

microhotplate in air atmosphere, sp^2 carbon bonds were broken and C-O and C=O bonds were formed, and oxygen was introduced into the PN polymer structure (Fig. 8C and D). However, the insertion of oxygen atoms in PN does not induce conductivity as no graphitic carbon was formed during microhotplate treatment. π - π stacking is absent after pre-annealing as the peak at 292 eV is not present. After RTP-annealing, all carbon-oxygen functional groups are still present (Fig. 8E and F). Scan rate tests confirm adsorption-controlled behavior and surface oxygen groups can contribute to adsorption of dopamine and other neurochemicals on carbon electrodes (Fig. 9).^{8,10}

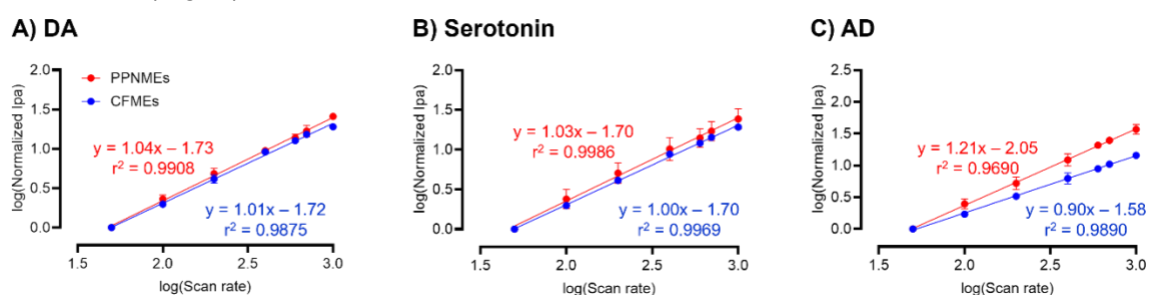


Figure 9. Scan-rate testing (50-1000 V/s) of (A) DA (B) serotonin (C) AD on CFMEs and PPNMEs.

Functional Group	Binding Energy (eV)	PN (Area %)	HP-PN (Area %)	RTP-PN (6 g) (Area %)	CF (Area %)
C=C	284.80	96.7	65.1	57.7	66.9
C-O	286.08	0	28.8	35.3	29.9
C=O	288.95	0	6.0	7.1	3.2
π - π^*	291.80	3.3	0	0	0

Table 2. Functional group percentages of PN, HP-PN, RTP-PN, and CF.

Table 2 shows the atomic percentages of carbon and oxygen on the surfaces of PN, HP-PN, RTP-PN (6 g), and CF. There was no oxygen present on PN surface, which only contains carbon. After pre-annealing on the hotplate, oxygen was involved in PN. After pyrolysis with

RTP, carbon bonds were broken and surface atomic percentage dropped down correspondingly. Compared to RTP-PN (6 g), CF possesses less oxygen content.

Element	PN (Atomic %)	HP-PN (Atomic %)	RTP-PN (6 g) (Atomic %)	CF (Atomic %)
C	100	85.8	79.1	86.6
O	0	14.2	20.9	13.4

Table 3. Functional group analysis of PN, HP-PN, RTP-PN, and CF.

Table 3 displays the area percentages of each functional group on XPS spectra in Fig. 8C, E, G by curve fitting. Carboxyl groups promote neurochemical adsorption.⁴ PN is a benzene-rich polymer with C=C present in the polymer structure.^{50,51} Because of the overlapping of the polymer layers, π - π stacking is shown in the XPS spectra. However, after HP pre-annealing, the stacking structure on PN surface was broken and oxygen-containing functional groups were formed, which resulted in the disappearance of π - π stacking.^{49,50} After application of high temperature with RTP, the π - π stacking decreased while the oxygen-containing groups increased. The XPS analysis, coupled with Raman spectra, shows that the pyrolyzed parylene has increased functional group formation during HP pre-annealing and RTP annealing. Oxygen content and functional groups of RTP-PN (6 g) are more than CF, which should benefit electrochemical detection of more neurotransmitters.

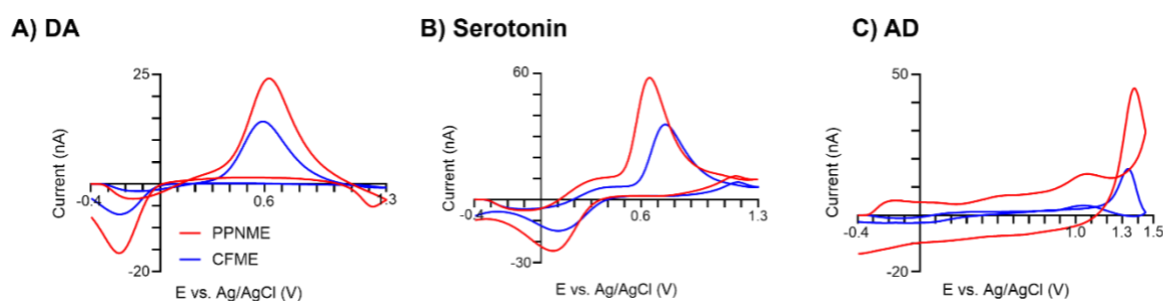


Figure 10. Electrochemical detection (CVs) of dopamine (DA), serotonin, and adenosine (AD) at CFMEs (blue) and PPNMEs (6 g) (red) for (A) 1 μ M DA (B) 1 μ M serotonin (C) 1 μ M AD.

CFMEs and PPNMEs were used to test the electrochemical detection of various neurotransmitters, including 1 μ M DA, serotonin, and AD (Fig. 10). The magnitudes of neurochemical oxidation currents on PPNMEs are higher than CFMEs. The PPNMEs have enhanced oxygen functional groups, which increase the electrostatic force between the

positively-charged analytes and the surface, and thus there is good sensitivity.^{4,6,52} The shapes of the CVs for dopamine and serotonin on PPNMEs were similar to those of CFMEs. The primary peak for adenosine is located on the back scan due to the high scan rate in FSCV.⁵³ The secondary peaks for AD oxidation currents were further enhanced from 20% of the primary current at CFMEs to 33% at PPNMEs.

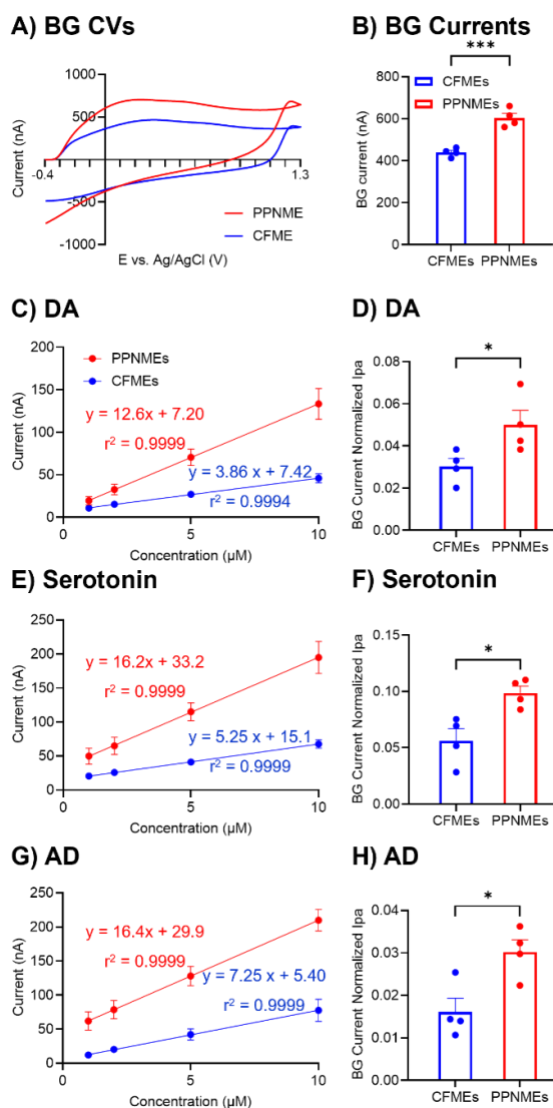


Figure 11. Background currents of electrodes and background-normalized currents and sensitivity tests of DA, serotonin, and AD on CFMEs and PPNMEs. (A) background CVs of CFME and PPNME. (B) Bar graphs comparing background currents. (C) Sensitivity for 1-10 μM DA. (D) Background normalized current comparison for 1 μM DA. (E) Sensitivity for 1-10 μM serotonin (F) Background normalized current comparison for 1 μM Serotonin. (G) Sensitivity for 1-10 μM AD. (G) Background normalized AD currents for 1 μM adenosine (all bar graphs n=4, t tests, *p<0.1, ***p<0.001, Error bars are SEM).

Fig. 11A shows CVs of CFME and PPNME background currents. In Fig. 11B, PPNME surface area is generally about 1.4 times higher than CF background signal, which shows a larger surface area for neurochemical detection. In Fig. 11C, E, and G, Faradaic currents for each analyte were plotted against concentration and the slope in the linear range used to quantify sensitivity (higher concentrations shown in Fig. 12). DA, serotonin, and AD are analytes that are positively charged at physiological pH, 7.4, and can be adsorbed to the electrode surface with the applied potential, -0.4 V. Generally, PPNMEs have higher slopes and higher sensitivities than CFMEs, about 2-3 times, which is larger than the difference in background currents. As PPNMEs have larger surface areas, Faradaic currents were divided by background currents to normalize for surface area. PPNMEs are compared to CFMEs in Fig. 11D, F, and H. Even correcting for background current, which is proportional to surface area, the signal for all 3 neurochemicals is higher for PPNMEs.

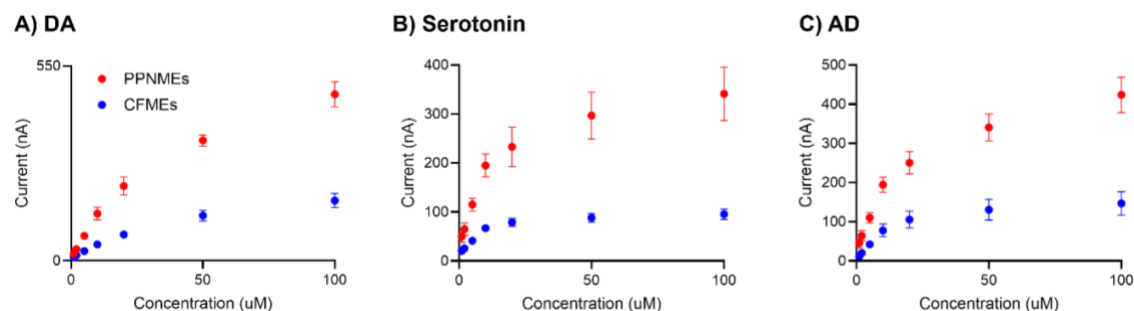
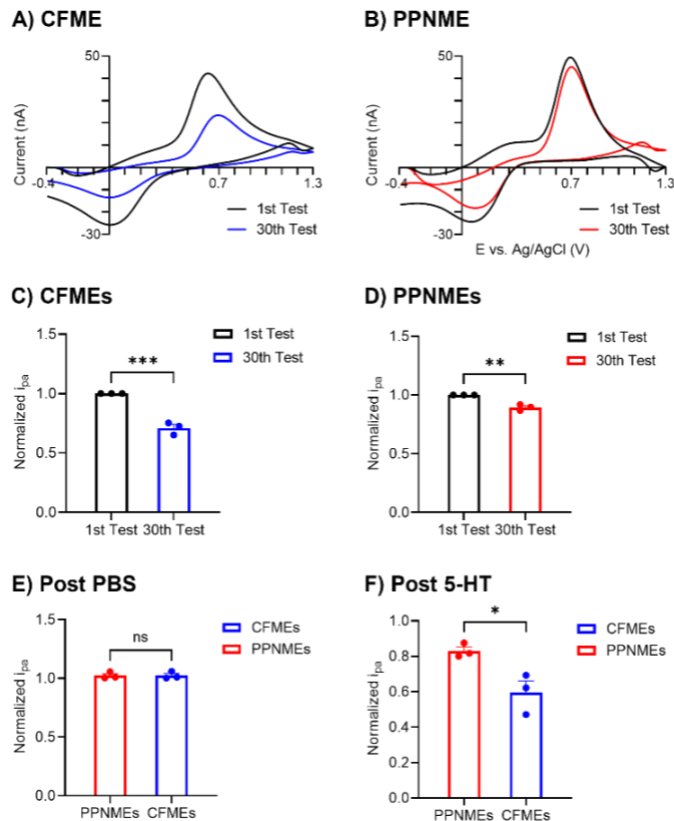


Figure 12. Concentration tests of DA, serotonin, and AD. (A) 1-100 μM DA (B) 1-100 μM serotonin (C) 10-500 μM AD.

Figure 13. Serotonin fouling test on CFMEs and PPNMEs. (A) CVs of 1st and 30th injections of 1 μM Serotonin on CFMEs. (B) CVs of 1st and 30th injections of 1 μM Serotonin on PPNMEs. (C) Bar graph 1st and 30th injections of 1 μM normalized serotonin currents on CFMEs (D) Bar graph 1st and 30th injections of 1 μM normalized serotonin currents on PPNMEs. (E) Bar graph of 1 μM normalized serotonin oxidation signals on CFMEs and PPNMEs after soaking in PBS buffer for 1 hr. (F) Bar graph of 1 μM normalized serotonin oxidation signals on CFMEs and PPNMEs after soaking in 1 μM serotonin for 1 hr. (n=3, t test, *p<0.1, **p<0.01, Error bars are SEM).

Fouling is a serious problem during electrochemical detection of some molecules, particularly serotonin.^{54,55} Serotonin molecules are polymerized with the application of the



dopamine waveform, and the polymer attachment on the electrode surface blocks the active sites for neurochemical adsorption, which will decrease detection sensitivity.^{29,30,54} With a rich amount of defect sites, we hypothesize that less fouling should be present on PPNMEs because of the decreased basal planes which will allow less π - π stacking between serotonin polymer and the electrode surface. One μM serotonin was injected at both electrodes 30 times every 15 s and serotonin currents at CFMEs and PPNMEs dropped about 50% and 5%, respectively (Fig. 13).

To further test if PPNMEs could resist serotonin fouling, longer-term fouling experiments were performed on both electrodes. As a control, electrodes were tested with serotonin before and after the waveform was applied in PBS buffer for 1 hr, and the current does not change (Fig. 13E). However, after applying the dopamine waveform for one hour in 1 μM serotonin, the oxidation currents for CFMEs dropped significantly, about 50%. In contrast, at PPNMEs the current dropped only about 20%, meaning 80% sensitivity was retained (Fig. 13F). The high

density of nanopores and rich defect sites on the PPNME surface will promote anti-fouling properties because there would be reduce π - π stacking between electrode surface and serotonin polymer.^{4,6,30,56}

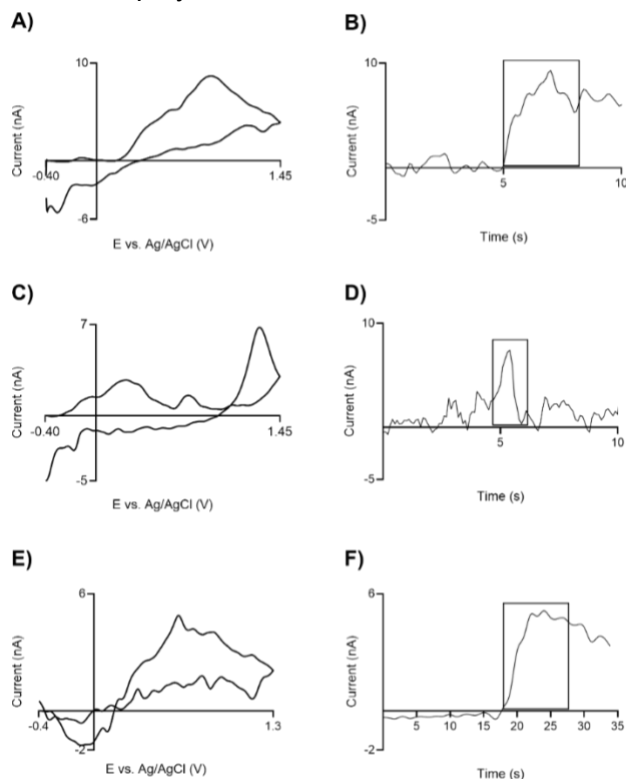


Figure 14. *In vivo* dopamine, adenosine, and serotonin testing with PPNMEs. (A) Stimulated DA CV (B) DA IT curve (C) Transient (unstimulated) AD CV (D) AD IT curve (E) Applied serotonin CV (F) Serotonin IT curve.

PPNMEs were employed *in vivo* to demonstrate their efficacy in detecting neurochemicals. For dopamine testing, stimulated dopamine release was evaluated in the mesolimbic circuit by applying electrical stimulation to the ventral tegmental area (VTA) and measuring dopamine in the nucleus accumbens (NAc) of rats. Fig. 14A illustrates the cyclic voltammogram of dopamine released, about 800 nM, upon electrical stimulation. As shown in the *i* versus *t* curve in Fig. 14B, the peak current increases with electrical stimulation, indicating dopamine release. Peaks in the CV are a bit wider *in vivo*, likely due to biofouling or possible background subtraction errors due to ionic changes that occur, changing the background current. As the testing was performed short-term, about 2 hr, no dramatic fouling happens on

the reference electrode, Ag/AgCl (Fig. 15), which would disturb the neurotransmitter detection. Therefore, no Nafion coating needs to be applied to the reference electrode.^{57,58}

Additionally, we continuously collected data and observed spontaneous adenosine transients with the PPNMEs.^{33,59,60} A representative transient, about 858 nM, is depicted in Fig. 9C (cyclic voltammogram showing adenosine-dopamine co-release) and Fig. 14D (I-versus t curve showing primary oxidation peak). These transients occurred without electrical stimulation and lasted approximately 1-2 seconds. As indicated by the cyclic voltammograms, the PPNMEs successfully measured both dopamine and adenosine, demonstrating their utility for detecting neurochemicals *in vivo*. As the tested region that releases serotonin is too small to perform electrical stimulation, we tested PPNMEs in the mouse brain slice (caudate putamen). The tissue was inserted by PPNMEs, and the depth is about 75 μm . A nanoliter injector was used to microinject serotonin close to the working electrode. Fig. 14E and F present exogenously applied serotonin CV and I-versus T curve and 832 nM serotonin were detected. While much of this data is similar to detection at CFMEs, the future possibility is to use PPN to make different geometries, and so this PPN will prove useful for *in vivo* measurements. For example, since PN is an insulator, if part of it can be masked and then pyrolyzed, perhaps using a laser or focused-ion beam milling, you could fabricate arrays and other geometries that are not possible to fabricate with carbon fibers.

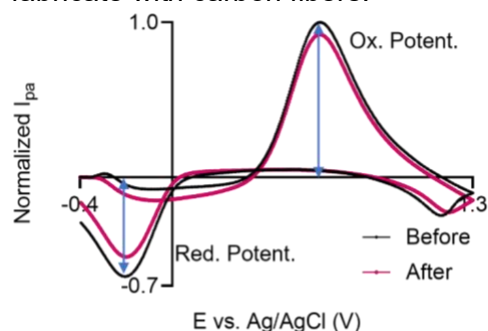


Figure 15. CVs of normalized DA currents before and after Ag/AgCl wire insertion into the brain slice.

3.4 Conclusions

RTP treatment of parylene N provides a method to fabricate microelectrodes with a thin film of carbon to sensitively track neurochemicals. Enhanced defect sites increased detection sensitivity for dopamine, serotonin, and adenosine. PPNMEs possess antifouling property, which make modified electrodes suitable for sensitive and long-term *in vivo* testing. Nb wires deposited with PN were etched to nanoscale, which makes them an attractive option for tissue applications. These electrodes can detect *in vivo* dopamine and adenosine release and thus are suitable for monitoring real-time release of neurotransmitters in tissue. Future work can examine other uses of this thin film electrode technology to customize different electrodes and microdevices.

References

- (1) Yang, C.; Wang, Y.; Jacobs, C. B.; Ivanov, I. N.; Venton, B. J. O₂ Plasma Etching and Antistatic Gun Surface Modifications for CNT Yarn Microelectrode Improve Sensitivity and Antifouling Properties. *Anal. Chem.* **2017**, *89* (10), 5605–5611. <https://doi.org/10.1021/acs.analchem.7b00785>.
- (2) Jacobs, C. B.; Ivanov, I. N.; Nguyen, M. D.; Zestos, A. G.; Venton, B. J. High Temporal Resolution Measurements of Dopamine with Carbon Nanotube Yarn Microelectrodes. *Anal. Chem.* **2014**, *86* (12), 5721–5727. <https://doi.org/10.1021/ac404050t>.
- (3) Schmidt, A. C.; Wang, X.; Zhu, Y.; Sombers, L. A. Carbon Nanotube Yarn Electrodes for Enhanced Detection of Neurotransmitter Dynamics in Live Brain Tissue. *ACS Nano* **2013**, *7* (9), 7864–7873. <https://doi.org/10.1021/nn402857u>.
- (4) Cao, Q.; Hensley, D. K.; Lavrik, N. V.; Venton, B. J. Carbon Nanospikes Have Better Electrochemical Properties than Carbon Nanotubes Due to Greater Surface Roughness and Defect Sites. *Carbon* **2019**, *155*, 250–257. <https://doi.org/10.1016/j.carbon.2019.08.064>.
- (5) G. Zestos, A.; Yang, C.; B. Jacobs, C.; Hensley, D.; Jill Venton, B. Carbon Nanospikes Grown on Metal Wires as Microelectrode Sensors for Dopamine. *Analyst* **2015**, *140* (21), 7283–7292. <https://doi.org/10.1039/C5AN01467K>.
- (6) Zhao, H.; Shrestha, K.; Hensley, D. K.; Venton, B. J. Carbon Nanospikes Have Improved Sensitivity and Antifouling Properties for Adenosine, Hydrogen Peroxide, and Histamine. *Anal. Bioanal. Chem.* **2023**, *415* (24), 6039–6050. <https://doi.org/10.1007/s00216-023-04875-5>.
- (7) Zachek, M. K.; Takmakov, P.; Moody, B.; Wightman, R. M.; McCarty, G. S. Simultaneous Decoupled Detection of Dopamine and Oxygen Using Pyrolyzed Carbon Microarrays and Fast-Scan Cyclic Voltammetry. *Anal. Chem.* **2009**, *81* (15), 6258–6265. <https://doi.org/10.1021/ac900790m>.
- (8) Ye, R.; James, D. K.; Tour, J. M. Laser-Induced Graphene. *Acc. Chem. Res.* **2018**, *51* (7), 1609–1620. <https://doi.org/10.1021/acs.accounts.8b00084>.
- (9) Lin, J.; Peng, Z.; Liu, Y.; Ruiz-Zepeda, F.; Ye, R.; Samuel, E. L. G.; Yacaman, M. J.; Yakobson, B. I.; Tour, J. M. Laser-Induced Porous Graphene Films from Commercial Polymers. *Nat. Commun.* **2014**, *5* (1), 5714. <https://doi.org/10.1038/ncomms6714>.
- (10) Carvalho, A. F.; Fernandes, A. J. S.; Leitão, C.; Deuermeier, J.; Marques, A. C.; Martins, R.; Fortunato, E.; Costa, F. M. Laser-Induced Graphene Strain Sensors Produced by Ultraviolet Irradiation of Polyimide. *Adv. Funct. Mater.* **2018**, *28* (52), 1805271. <https://doi.org/10.1002/adfm.201805271>.
- (11) Gu, X. J. Raman Spectroscopy and the Effects of Ultraviolet Irradiation on Polyimide Film. *Appl. Phys. Lett.* **1993**, *62* (13), 1568–1570. <https://doi.org/10.1063/1.108643>.
- (12) Parmeggiani, M.; Zaccagnini, P.; Stassi, S.; Fontana, M.; Bianco, S.; Nicosia, C.; Pirri, C. F.; Lamberti, A. PDMS/Polyimide Composite as an Elastomeric Substrate for Multifunctional Laser-Induced Graphene Electrodes. *ACS Appl. Mater. Interfaces* **2019**, *11* (36), 33221–33230. <https://doi.org/10.1021/acsami.9b10408>.
- (13) Yonkoski, R. K.; Soane, D. S. Model for Spin Coating in Microelectronic Applications. *J. Appl. Phys.* **1992**, *72* (2), 725–740. <https://doi.org/10.1063/1.351859>.

- (14) Mao, D.; Lv, G.; Gao, G.; Fan, B. Fabrication of Polyimide Films with Imaging Quality Using a Spin-Coating Method for Potential Optical Applications. *J. Polym. Eng.* **2019**, *39* (10), 917–925. <https://doi.org/10.1515/polyeng-2019-0177>.
- (15) Chang, T. Y.; Yadav, V. G.; De Leo, S.; Mohedas, A.; Rajalingam, B.; Chen, C.-L.; Selvarasah, S.; Dokmeci, M. R.; Khademhosseini, A. Cell and Protein Compatibility of Parylene-C Surfaces. *Langmuir* **2007**, *23* (23), 11718–11725. <https://doi.org/10.1021/la7017049>.
- (16) Buchwalder, S.; Borzi, A.; Diaz Leon, J. J.; Bourgeois, F.; Nicolier, C.; Nicolay, S.; Neels, A.; Zywitzki, O.; Hogg, A.; Burger, J. Thermal Analysis of Parylene Thin Films for Barrier Layer Applications. *Polymers* **2022**, *14* (17), 3677. <https://doi.org/10.3390/polym14173677>.
- (17) Gholizadeh, S.; Lincoln, D. M.; Allahyari, Z.; Widom, L. P.; Carter, R. N.; Gaborski, T. R. Optimization of Parylene C and Parylene N Thin Films for Use in Cellular Co-Culture and Tissue Barrier Models. *Sci. Rep.* **2023**, *13* (1), 4262. <https://doi.org/10.1038/s41598-023-31305-4>.
- (18) Rapp, B. E.; Voigt, A.; Dirschka, M.; Länge, K. Deposition of Ultrathin Parylene C Films in the Range of 18 nm to 142 nm: Controlling the Layer Thickness and Assessing the Closeness of the Deposited Films. *Thin Solid Films* **2012**, *520* (15), 4884–4888. <https://doi.org/10.1016/j.tsf.2012.03.035>.
- (19) Chun, W.; Chou, N.; Cho, S.; Yang, S.; Kim, S. Evaluation of Sub-Micrometer Parylene C Films as an Insulation Layer Using Electrochemical Impedance Spectroscopy. *Prog. Org. Coat.* **2014**, *77* (2), 537–547. <https://doi.org/10.1016/j.porgcoat.2013.11.020>.
- (20) Kahouli, A. Effect of Film Thickness on Structural, Morphology, Dielectric and Electrical Properties of Parylene C Films. *J. Appl. Phys.* **2012**, *112* (6), 064103. <https://doi.org/10.1063/1.4752022>.
- (21) Kim, B. J.; Meng, E. Micromachining of Parylene C for bioMEMS. *Polym. Adv. Technol.* **2016**, *27* (5), 564–576. <https://doi.org/10.1002/pat.3729>.
- (22) Liu, J.; Cao, Y. An Electrochemical Sensor Based on an Anti-Fouling Membrane for the Determination of Histamine in Fish Samples. *Anal. Methods* **2021**, *13* (5), 685–694. <https://doi.org/10.1039/D0AY01901A>.
- (23) Gazicki-Lipman, M. Vapor Deposition Polymerization of Para-Xylylene Derivatives-Mechanism and Applications. *Shinku* **2007**, *50* (10), 601–608. <https://doi.org/10.3131/jvsj.50.601>.
- (24) Kramer, P.; Sharma, A. K.; Hennecke, E. E.; Yasuda, H. Polymerization of Para-Xylylene Derivatives (Parylene Polymerization). I. Deposition Kinetics for Parylene N and Parylene C. *J. Polym. Sci. Polym. Chem. Ed.* **1984**, *22* (2), 475–491. <https://doi.org/10.1002/pol.1984.170220218>.
- (25) Kim, M. P.; Lee, G.; Noh, B.; Kim, J.; Kwak, M. S.; Lee, K. J.; Ko, H. Enhancing Energy Harvesting Performance of Bilayered Parylene Triboelectric Nanogenerators through Interfacial Polarization. *Nano Energy* **2024**, *119*, 109087. <https://doi.org/10.1016/j.nanoen.2023.109087>.
- (26) Morton, K. C.; Morris, C. A.; Derylo, M. A.; Thakar, R.; Baker, L. A. Carbon Electrode Fabrication from Pyrolyzed Parylene c. *Anal. Chem.* **2011**, *83* (13), 5447–5452. <https://doi.org/10.1021/ac200885w>.
- (27) Venton, B. J.; Cao, Q. Fundamentals of Fast-Scan Cyclic Voltammetry for Dopamine Detection. *Analyst* **2020**, *145* (4), 1158–1168. <https://doi.org/10.1039/C9AN01586H>.

- (28) Zachek, M. K.; Hermans, A.; Wightman, R. M.; McCarty, G. S. Electrochemical Dopamine Detection: Comparing Gold and Carbon Fiber Microelectrodes Using Background Subtracted Fast Scan Cyclic Voltammetry. *J. Electroanal. Chem.* **2008**, *614* (1), 113–120. <https://doi.org/10.1016/j.jelechem.2007.11.007>.
- (29) Sarada, B. V.; Rao, T. N.; Tryk, D. A.; Fujishima, A. Electrochemical Oxidation of Histamine and Serotonin at Highly Boron-Doped Diamond Electrodes. *Anal. Chem.* **2000**, *72* (7), 1632–1638. <https://doi.org/10.1021/ac9908748>.
- (30) Mendoza, A.; Asrat, T.; Liu, F.; Wonnemberg, P.; Zestos, A. G. Carbon Nanotube Yarn Microelectrodes Promote High Temporal Measurements of Serotonin Using Fast Scan Cyclic Voltammetry. *Sensors* **2020**, *20* (4), 1173. <https://doi.org/10.3390/s20041173>.
- (31) Basheer, R.; Strecker, R. E.; Thakkar, M. M.; McCarley, R. W. Adenosine and Sleep–Wake Regulation. *Prog. Neurobiol.* **2004**, *73* (6), 379–396. <https://doi.org/10.1016/j.pneurobio.2004.06.004>.
- (32) Sweeney, M. I. Neuroprotective Effects of Adenosine in Cerebral Ischemia: Window of Opportunity. *Neurosci. Biobehav. Rev.* **1997**, *21* (2), 207–217. [https://doi.org/10.1016/S0149-7634\(96\)00011-5](https://doi.org/10.1016/S0149-7634(96)00011-5).
- (33) Nguyen, M. D.; Lee, S. T.; Ross, A. E.; Ryals, M.; Choudhry, V. I.; Venton, B. J. Characterization of Spontaneous, Transient Adenosine Release in the Caudate-Putamen and Prefrontal Cortex. *PLOS ONE* **2014**, *9* (1), e87165. <https://doi.org/10.1371/journal.pone.0087165>.
- (34) Paxinos, G.; Watson, C. *The Rat Brain in Stereotaxic Coordinates - 6th Edition*; 1997.
- (35) Shao, Z.; Zhao, H.; Dunham, K. E.; Cao, Q.; Lavrik, N. V.; Venton, B. J. 3D-Printed Carbon Nanoneedle Electrodes for Dopamine Detection in *Drosophila*. *Angew. Chem.* **2024**, *136* (30), e202405634. <https://doi.org/10.1002/ange.202405634>.
- (36) Ferrer, L.; Shamloo, E.; Cisquella Serra, A.; Salazar, A.; Madou, M.; Lee, J. Size-Dependent Electrical and Thermal Conductivities of Electro-Mechanically-Spun Glassy Carbon Wires. *Carbon* **2017**, *130*. <https://doi.org/10.1016/j.carbon.2017.12.113>.
- (37) Uskoković, V. A Historical Review of Glassy Carbon: Synthesis, Structure, Properties and Applications. *Carbon Trends* **2021**, *5*, 100116. <https://doi.org/10.1016/j.cartre.2021.100116>.
- (38) Liger, M.; Harder, T. A.; Tai, Y.-C.; Konishi, S. Parylene-Pyrolyzed Carbon for MEMS Applications. In *17th IEEE International Conference on Micro Electro Mechanical Systems. Maastricht MEMS 2004 Technical Digest*; 2004; pp 161–164. <https://doi.org/10.1109/MEMS.2004.1290547>.
- (39) Song, Z.; Park, J.-H.; Kim, H.-R.; Lee, G.-Y.; Kang, M.-J.; Kim, M.-H.; Pyun, J.-C. Carbon Electrode Obtained via Pyrolysis of Plasma-Deposited Parylene-C for Electrochemical Immunoassays. *Analyst* **2022**, *147* (16), 3783–3794. <https://doi.org/10.1039/D2AN00854H>.
- (40) Yoshioka, K.; Naka, K.; Konishi, S. Promotion Effect of Iodization on Carbonization for MEMS Application. In *2007 IEEE 20th International Conference on Micro Electro Mechanical Systems (MEMS)*; 2007; pp 243–246. <https://doi.org/10.1109/MEMSYS.2007.4433058>.
- (41) Takmakov, P.; Zachek, M. K.; Keithley, R. B.; Walsh, P. L.; Donley, C.; McCarty, G. S.; Wightman, R. M. Carbon Microelectrodes with a Renewable Surface. *Anal. Chem.* **2010**, *82* (5), 2020–2028. <https://doi.org/10.1021/ac902753x>.

- (42) Shao, Z.; Puthongkham, P.; Hu, K. K.; Jia, R.; Mirkin, M. V.; Venton, B. J. Thin Layer Cell Behavior of CNT Yarn and Cavity Carbon Nanopipette Electrodes: Effect on Catecholamine Detection. *Electrochimica Acta* **2020**, *361*, 137032. <https://doi.org/10.1016/j.electacta.2020.137032>.
- (43) Dresselhaus, M. S.; Jorio, A.; Saito, R. Characterizing Graphene, Graphite, and Carbon Nanotubes by Raman Spectroscopy. *Annu. Rev. Condens. Matter Phys.* **2010**, *1* (Volume 1, 2010), 89–108. <https://doi.org/10.1146/annurev-conmatphys-070909-103919>.
- (44) Wang, Y.; Alsmeyer, D. C.; McCreery, R. L. Raman Spectroscopy of Carbon Materials: Structural Basis of Observed Spectra. *Chem. Mater.* **1990**, *2* (5), 557–563. <https://doi.org/10.1021/cm00011a018>.
- (45) Saito, R.; Hofmann, M.; Dresselhaus, G.; Jorio, A.; Dresselhaus, M. S. Raman Spectroscopy of Graphene and Carbon Nanotubes. *Adv. Phys.* **2011**, *60* (3), 413–550. <https://doi.org/10.1080/00018732.2011.582251>.
- (46) Ferrari, A. C.; Robertson, J. Interpretation of Raman Spectra of Disordered and Amorphous Carbon. *Phys. Rev. B* **2000**, *61* (20), 14095–14107. <https://doi.org/10.1103/PhysRevB.61.14095>.
- (47) Lee, Y.-J. The Second Order Raman Spectroscopy in Carbon Crystallinity. *J. Nucl. Mater.* **2004**, *325* (2), 174–179. <https://doi.org/10.1016/j.jnucmat.2003.12.005>.
- (48) Escribano, R.; Sloan, J. J.; Siddique, N.; Sze, N.; Dudev, T. Raman Spectroscopy of Carbon-Containing Particles. *Vib. Spectrosc.* **2001**, *26* (2), 179–186. [https://doi.org/10.1016/S0924-2031\(01\)00106-0](https://doi.org/10.1016/S0924-2031(01)00106-0).
- (49) Piscanec, S.; Cantoro, M.; Ferrari, A. C.; Zapien, J. A.; Lifshitz, Y.; Lee, S. T.; Hofmann, S.; Robertson, J. Raman Spectroscopy of Silicon Nanowires. *Phys. Rev. B* **2003**, *68* (24), 241312. <https://doi.org/10.1103/PhysRevB.68.241312>.
- (50) Pruden, K. G.; Sinclair, K.; Beaudoin, S. Characterization of Parylene-N and Parylene-C Photooxidation. *J. Polym. Sci. Part Polym. Chem.* **2003**, *41* (10), 1486–1496. <https://doi.org/10.1002/pola.10681>.
- (51) Wu, P. K.; Yang, G.-R.; McDonald, J. F.; Lu, T.-M. Surface Reaction and Stability of Parylene N and F Thin Films at Elevated Temperatures. *J. Electron. Mater.* **1995**, *24* (1), 53–58. <https://doi.org/10.1007/BF02659727>.
- (52) Cao, Q.; Puthongkham, P.; Venton, B. J. Review: New Insights into Optimizing Chemical and 3D Surface Structures of Carbon Electrodes for Neurotransmitter Detection. *Anal. Methods* **2019**, *11* (3), 247–261. <https://doi.org/10.1039/C8AY02472C>.
- (53) Swamy, B. E. K.; Venton, B. J. Subsecond Detection of Physiological Adenosine Concentrations Using Fast-Scan Cyclic Voltammetry. *Anal. Chem.* **2007**, *79* (2), 744–750. <https://doi.org/10.1021/ac061820i>.
- (54) Dunham, K. E.; Venton, B. J. Improving Serotonin Fast-Scan Cyclic Voltammetry Detection: New Waveforms to Reduce Electrode Fouling. *Analyst* **2020**, *145* (22), 7437–7446. <https://doi.org/10.1039/D0AN01406K>.
- (55) Jackson, B. P.; Dietz, S. M.; Wightman, R. M. Fast-Scan Cyclic Voltammetry of 5-Hydroxytryptamine. *Anal. Chem.* **1995**, *67* (6), 1115–1120. <https://doi.org/10.1021/ac00102a015>.

- (56) Puthongkham, P.; Venton, B. J. Nanodiamond Coating Improves the Sensitivity and Antifouling Properties of Carbon Fiber Microelectrodes. *ACS Sens.* **2019**, *4* (9), 2403–2411. <https://doi.org/10.1021/acssensors.9b00994>.
- (57) Hashemi, P.; Walsh, P. L.; Guillot, T. S.; Gras-Najjar, J.; Takmakov, P.; Crews, F. T.; Wightman, R. M. Chronically Implanted, Nafion-Coated Ag/AgCl Reference Electrodes for Neurochemical Applications. *ACS Chem. Neurosci.* **2011**, *2* (11), 658–666. <https://doi.org/10.1021/cn2000684>.
- (58) Jang, J.; Cho, H.-U.; Hwang, S.; Kwak, Y.; Kwon, H.; Heien, M. L.; Bennet, K. E.; Oh, Y.; Shin, H.; Lee, K. H.; Jang, D. P. Understanding the Different Effects of Fouling Mechanisms on Working and Reference Electrodes in Fast-Scan Cyclic Voltammetry for Neurotransmitter Detection. *The Analyst* **2024**, *149* (10), 3008–3016. <https://doi.org/10.1039/D3AN02205F>.
- (59) Borgus, J. R.; Puthongkham, P.; Venton, B. J. Complex Sex and Estrous Cycle Differences in Spontaneous Transient Adenosine. *J. Neurochem.* **2020**, *153* (2), 216–229. <https://doi.org/10.1111/jnc.14981>.
- (60) Ganesana, M.; Venton, B. J. Early Changes in Transient Adenosine during Cerebral Ischemia and Reperfusion Injury. *PLOS ONE* **2018**, *13* (5), e0196932. <https://doi.org/10.1371/journal.pone.0196932>.

Chapter 4

Laser-Induced-Graphene Electrodes from Parylene-N: Use of Nanoscribe 3D Printer to Fabricate Carbon Electrodes for Neurotransmitters

Abstract

Laser-induced graphene (LIG) uses the energy of a laser to turn a non-conducting polymer into a graphitic conductor, and LIG is useful for the fabrication of supercapacitors and biosensors. Laser-induced-graphene (LIG) typically usually utilizes polyimide (PI), which is deposited on the substrate via spin coating, but spin coating cannot be used for cylindrical structures such as microelectrodes. Here, we used parylene as a substrate for LIG because it can be deposited in a thin layer on cylindrical microwires via chemical vapor deposition (CVD). Heating to 350 °C increases the light adsorption, and then the laser of Nanoscribe 3D printer was used to carbonize the surface of parylene (PN) to create laser-induced-graphene (LIG-PN). A higher roughness and more oxygen functional groups were present on LIG-PN compared to carbon fiber (CF). Dopamine and serotonin oxidation currents at LIG-PN modified electrodes (LIG-PNMEs) were about 1.50 and 1.30 times higher than carbon fiber (CF). Responses were more reversible due to the surface roughness leading to trapping effects. In addition, LIG-PNMEs possess antifouling and anti-biofouling properties, which enabled stable dopamine detection in the rat brain and serotonin tracking in *Drosophila*. LIG-PN was also combined with microelectromechanical systems (MEMs) to make electrodes on a microdevice for neurochemical detection. The Nanoscribe is an easy way to design shapes from COMSOL for printing carbon electrodes, with micron resolution, enabling the design of electrodes or arrays from a biocompatible parylene structure.

Keywords: Laser-induced-graphene, Parylene-N, Adsorption, *In vivo*, MEMs

4.1 Introduction

Polyimide (PI) is a commercially-available polymer that can withstand high temperature and insulate electronics.¹⁻³ Spin-coated or chemically vapor deposited polyimide (PI) or PI sheets are used for the synthesis of laser-induced-graphene (LIG), which was initially developed by Tour Group.^{4,5} LIG possesses good biocompatibility and electrical conductivity. LIG originated from PI (LIG-PI) is applied for the fabrication of microfluidic devices, supercapacitors, as well as different types of sensors, such as temperature, airflow, and humidity.⁶⁻¹⁰ LIG has also been implemented to develop microelectromechanical systems (MEMs).^{11,12} An alternative insulator for MEMs devices is parylene, as it fully covers surfaces, is impermeable to moisture, has a high dielectric constant, protects from corrosion, and is a good insulator..¹³ Recently, parylene has attracted attention as an alternative polymer for the fabrication of LIG, but microelectrodes for neurotransmitters have not been made with LIG from parylene.¹⁴⁻¹⁶

Medical devices are often insulated with parylene because of its biocompatibility.^{17,18} Parylene, which has many types of derivatives – C, N, D, VT4, and AF4, is a benzene-rich polymer that possesses chemical inertness, flexibility, and optical transparency.¹⁹⁻²¹ Thin-film parylene is deposited on a variety of substrates by chemical vapor deposition (CVD).^{22,23} as Applications of parylene include photooxidation for coating microelectronic and medical devices, cellular co-culture and tissue barrier models, and encapsulation material.^{14,24-27} Pyrolysis of parylene leads to graphitic materials that can be made into electrodes. The Baker group used cyclic voltammetry (CV) to perform electrochemical detection with pyrolyzed parylene-C electrodes.²⁸ Our group developed pyrolyzed parylene-N electrodes, pyrolyzed by rapid thermal processing (RTP), for neurochemical detection with fast-scan cyclic voltammetry (FSCV). Parylene has also been utilized for the formation of LIG and applied for the generation of microsupercapacitors.¹⁴ However, LIG of parylene has not been used to make electrodes for FSCV detection.

Laser-induced graphene is commonly induced using CO₂ infrared (IR) and ultraviolet (UV) lasers, for both polyimide and parylene.^{5,7,29–31} The Nanoscribe 3D printer laser, ~390 nm wavelength, can provide the energy, which should be enough to pyrolyze polymer.³² The Nanoscribe printer is generally utilized for direct laser writing to construct COMSOL-designed 3D-printing structures, with a liquid photoresist that absorbs the laser energy. Our lab has used this method to print micron sized structures that are pyrolyzed to glassy carbon electrodes with rapid thermal processing.^{33–36} The advantages of the Nanoscribe printer is that you use commercial software to make a 3D design, and then the instrument automatically prints it, with resolution of 1 μm. Thus, there is no need for a custom laser set-up. Here, we use the Nanoscribe printer to selectively pyrolyze parylene to make 50-100 μm, while the rest of the PN-coated surface acts as a biocompatible insulator.¹⁶

In this work, we used a Nanoscribe 3D printer to fabricate laser-induced graphite from parylene N, for detection of dopamine and serotonin. Dopamine (DA) regulates nerve function crucial for movement and reward processing,^{37,38} while serotonin (5-HT) is important for mood and is dysregulated in depression. LIG-PN modified electrodes (LIG-PNMEs) have good electrochemical performance for detecting DA, with increased reversibility because the surface roughness helps trap molecules on the electrode surface. Because of the increased level of defect sites, LIG-PNMEs promoted 5-HT adsorption and resists 5-HT polymer fouling and biofouling, originating from the attachment of brain tissue.^{39,40,41} LIG-PN on Nb wires were used to detect dopamine *in vivo* in rats and serotonin in *Drosophila*. We also developed MEMS devices with LIG-PN electrodes to detect DA. Using the Nanoscribe printer to fabricate LIG electrodes in parylene with a resolution, 0.75 μm to 1.50 μm, will enable customized electrode geometries and array designs for MEMS devices and other electrodes in the future.

4.2 Methods and Materials

4.2.1 Chemicals and materials

Dopamine was purchased from ThermoFisher Scientific (Waltham, WA) and serotonin was purchased from Sigma-Aldrich (St. Louis, Missouri). Perchloric acid (0.1M) was used to make stock solutions (10 mM). Stock solutions were diluted by using phosphate-buffered saline (PBS) buffer (1131.5 mM NaCl, 3.25 mM KCl, 1.2 mM CaCl₂, 1.25 mM NaH₂PO₄, 1.2 mM MgCl₂).

4.2.2 Construction of LIG-PNMEs

Nb wires (diameter 50 μm, ESPI Metals, Ashland, OR) were electrically etched to 1 μm in 4 M NaOH with the application of DC voltage 2V. Etched Nb wires were coated with parylene-N by using SCS parylene coater (PDS 2010, IN). The chamber of parylene coater initially vaporizes [2, 2] Paracyclophane, the powdered precursor, at 150°C under vacuum. Then, the temperature is ramped to a high temperature, 650 °C, to cause the pyrolysis of dimer to form the monomer, para-xylene. When the temperature drops back to 25 °C, monomers will be polymerized and deposited on the substrate. The coating rate and thickness is controlled during vapor deposition process by parylene coater. Parylene-coated Nb wires were pre-annealed on the hotplate for shrinkage, by heating from 25°C to 350 °C at 40 °C/min and then holding at 350 °C for 10 min in air atmosphere. Parylene-N-coated Nb wires were further treated with 2-photon laser in Nanoscribe instrument for direct laser writing and air projective (laser wavelength = 390 nm, laser power = 40 mW, scanning speed = 5000 μm/s, hatching distance = 1.0 μm, and slicing distance = 1.0 μm). Nb wires coated with parylene-N, transformed into laser-induced-graphite, were inserted into glass capillaries, and then sealed with 5-min epoxy (J-B weld, Sulphur Springs, TX).

4.2.3 Construction of MEMS

The chips for LIG-MEMs sensors were fabricated using a well-established processing sequence that is based on a combination of wafer-level photolithographic patterning and thin film deposition.^{11,12} More specifically, a liftoff process was used to create metal electrode patterns on 4" diameter fused silica wafers. The processing sequence started with dehydration

of silica wafers on a hot plate at 250°C for at least 30 minutes followed by oxygen plasma treatment for 2 minutes. A double layer resist was deposited on the dehydrated silica wafers by first spin coating liftoff resist (LOR3A, XX Inc.) at 3000 RMP and bake it on a hot plate at 180 °C for 2 min. The second resist layer was a positive tone photoresist SPR 955CM-0.7 (DuPont Inc.) deposited by spin coating at 3000 RPM with a subsequent bake on a hot plate at 90°C for 90 seconds. Wafers with the double-layer resist were exposed on MA6 (spin coating liftoff resist SUSS MicroTec) contact aligner with a mask containing metal electrode patterns. After development in CD26 developer for 60 seconds, rinsing with deionized water, and drying with filtered nitrogen, the wafers were transferred into the chamber of a DC sputter deposition tool and coated with 100 nm Nb. The final steps of the processing sequence were metal lift-off in acetone, followed by soaking in N-methylpyrrolidone (to remove remaining LOR3A resist), rinsing, drying and dicing of the processed wafers into chips.

4.2.4 Construction of CFMEs

Carbon fibers with a diameter of 7 μm (T650-35, Cytec, Woodland Park, NJ) were inserted into glass capillaries. Glass capillaries with CFs were heated by using PE-21 pipette puller (Setagaya-ku, Tokyo, Japan) and then pulled into two needle-shaped microelectrodes. The length of exposed CFs was cut to around 50-100 μm . Epon Resin 828 (Danbury, CT) mixed with 14% (w/w) m-phenylenediamine (Acros Organics, Morris Plains, NJ) was used to seal the tips of microelectrodes with dipping for 30 s. Electrodes were rinsed with acetone for 5 s. CF microelectrodes were cured at room temperature on the benchtop overnight. The electrodes were cured in an oven and set at 100°C for 2 hours and then 150°C overnight.

4.2.5 Instrumentation

FEI Quanta 650 SEM (ThermoFisher Scientific, Waltham, MA) was used to collect images. The accelerating voltage was 2 kV, applied on secondary electron detector. InVia Confocal Raman microscope (Renishaw, Gloucestershire, United Kingdom) was used to obtain

Raman spectra of PN, HP-PN, and LIG-PN. Oxygen and carbon allotropes were characterized with an X-ray photoelectron spectrometer (Physical Electronics, Chanhassen, MN)

ChemClamp potentiostat (Dagan, Minneapolis, MN) with a headstage of 1 M Ω resistance was used to collect FSCV data. The triangular waveform, scanning from -0.4 V to 1.3 V, was used to obtain electrochemical data at a scan rate of 400 V/s and a frequency of 10 Hz. HDCV Analysis Software (Department of Chemistry, University of North Carolina at Chapel Hill) was used to perform data analysis. Silver/silver chloride was used as a reference electrode. Samples were injected through a flow cell at 2 mL/min by using a six-port, stainless steel HPLC loop injector with an air actuator (VICI Valco Instruments, Houston, TX). Electrode capillaries were filled with 1 M KCl to provide electrical connection between the electrode and the silver wire in the electrode holder (Warner Instruments, Holliston, MA).

4.2.6 Background-current subtraction

The scan rate for FSCV is 400 V/s background currents are higher than Faradaic currents. Thus, CVs are background-current subtracted by averaging the background current right before the flow cell injection or stimulus, to remove the background and better visualize the Faradaic current.

4.2.7 *In Vivo* Measurements

All animal experiments were performed as approved by the Animal Care and Use Committee (ACUC) of the University of Virginia. Urethane (5% saline solution, 0.3 mL/100 g i.p.) was used to anesthetize rats (Charles River). Isothermal pad (Delta Phase Pad; Braintree Scientific, Braintree, MA, USA) was used to maintain the temperature of the rectal and core body at 37 °C. Hourly checks (paw pinch) were made of respiration and depth of anesthesia. A local anesthetic (bupivacaine) was applied on exposed skin and muscle tissue during surgery.

A stereotaxic frame was used to hold the rat, and the stimulating electrode, working electrode, and reference electrode were placed into the holes, which were drilled precisely in the skull, according to the atlas of Paxinos and Watson.⁴² The working electrode was lowered

into the NAc core (+1.3 mm anterior-posterior [AP], +2.0 mm medial-lateral [ML], -7.1 mm dorsal-ventral [DV]), The dorsoventral coordinate of the electrodes was adjusted to maximize stimulated dopamine release. . The Ag/AgCl reference electrode was inserted in the contralateral side of the brain. The bipolar metal stimulating electrode was placed in the VTA (-4.7 mm AP, +0.9 mm ML, -8.5 mm DV) (Plastics One, Roanoke, VA, USA). The bipolar stimulating electrode delivered a constant biphasic current stimulus at +300 μ A, 2 ms, 24 pulses to electrically stimulate dopamine. Spontaneous adenosine was recorded with no electrical stimulation applied. Guillotine was used to euthanize animals after each experiment (World Precision Instruments, Sarasota, Florida, USA)

4.3 Results

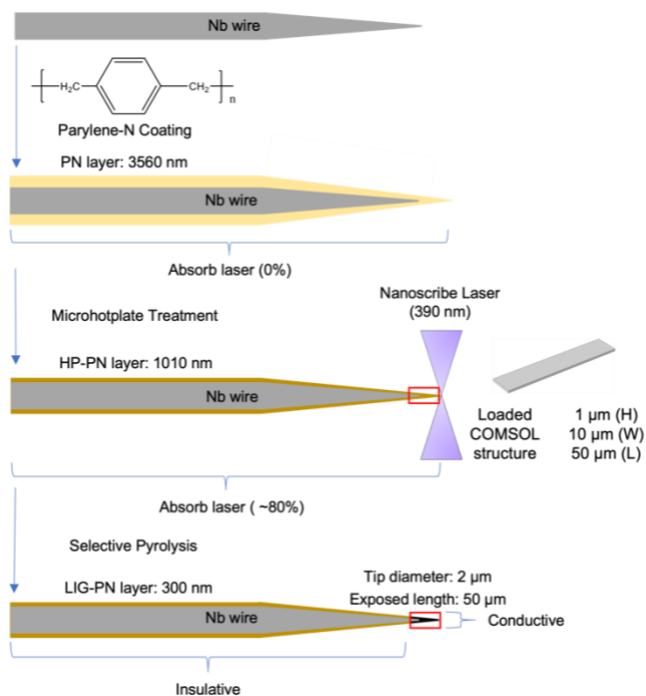


Figure 1. Overview of the fabrication of LIG-PN modified electrode

An overview of the fabrication processes of LIG modified electrode is shown in Figure 1. First, etched Nb wires are coated with parylene-N (PN) coating using vapor deposition. Then, PN-coated Nb wires are pre-annealed on a microhotplate, by raising temperature from 25 °C to 350 °C, to induce coating shrinkage and promote UV light absorption, shown in Table. 1 and Fig. S1 respectively. 12 g was selected as the deposited amount for further graphitization of PN as about the thickness of 1.30 μm remained after pre-annealing. It is expected that, after laser scanning, the thickness of pyrolyzed LIG-PN is enough to transfer electrons and induce electrochemical detection. After microhotplate heating, the light absorbance of PN is increased from 0 % to 80 %, as shown in Fig. 2. Then, the Nanoscribe laser (laser power = 40 mW) is used to selectively scan the surface of PN coating on Nb wires to synthesize laser-induced-graphene (LIG). The Nanoscribe has two lasers at 780 nm, which generate a wavelength of 390 nm when combined, and the energy for carbonization is only high enough where the two lasers meet to carbonize the PN. Thus, the spatial resolution for laser-induced graphitization is high

(the resolution of the printer is 1 μm). Because the lasers can only graphitize the top of the PN, the wires are then flipped 180° and the same scanning process repeated to treat the whole cylindrical surface.

Parylene Type	Mass (g)	Deposited Thickness (nm)	Thickness after hot plate (nm)	Thickness after laser scanning (nm)
N	2	400	108	N/A
N	4	917	350	N/A
N	8	2095	671	N/A
N	12	3560	1010	300

Table 1. PN coating thicknesses with 2g, 4g, 8 g, and 12 g loaded into the parylene coater, before and after microhotplate heating.

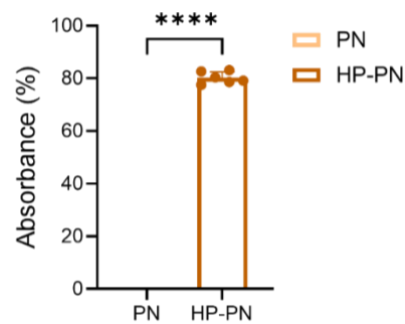


Figure 2. Light absorbance percentage of PN and HP-PN at 390 nm

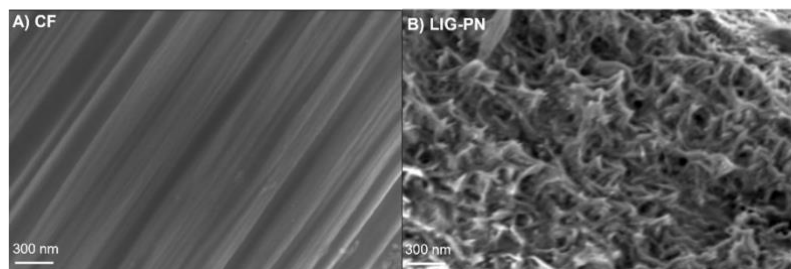


Figure 3. Scanning electron microscopy images of (A) zoomed in surface of CFME (B) zoomed in surface of LIG-PN

The surfaces of LIG from PN (LIG-PN) and CF were characterized by SEM. A smooth surface is observed on CF with some grooves, which does not favor the trapping of analytes. However, LIG-PN has a larger surface roughness, which increases the surface area, could promote the adsorption of analytes, and restrict their diffusion.⁴³ Therefore, LIG is hypothesized to be a favorable carbon surface for electrochemistry.⁴³

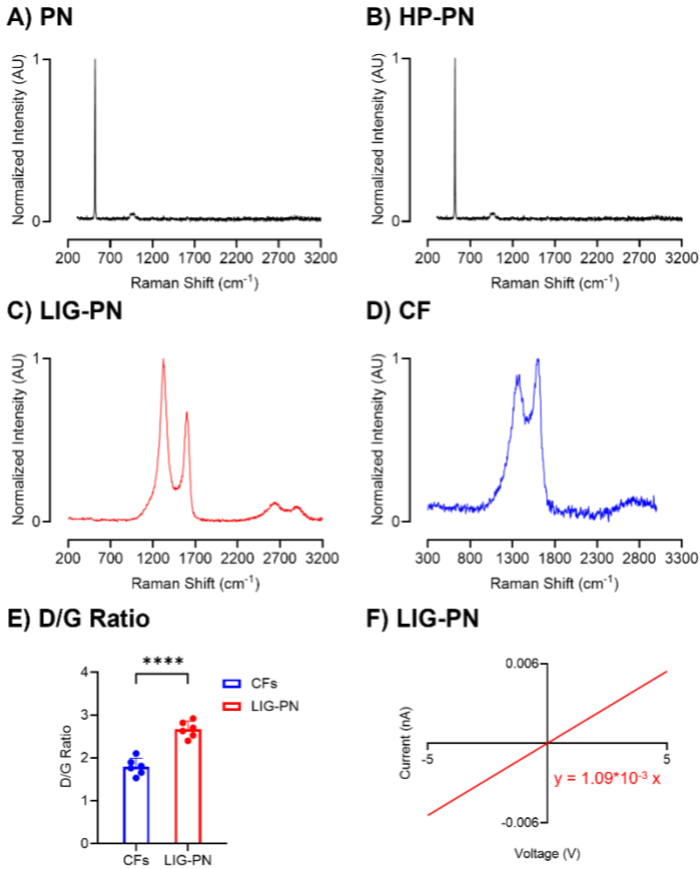


Figure 4. Raman spectra of (A) PN on Si wafer (B) HP-PN on Si wafer (C) LIG-PN on Si wafer and (D) CF. The D peak and G peak are located at 1360 cm^{-1} and 1580 cm^{-1} . (E) Bar graph of D/G ratios for CFs and LIG-PN (unpaired t-test, $n=6$, **** $p<0.0001$) (F) Conductivity test of LIG-PN

We used Raman spectroscopy to study the carbon structures of LIG-PN. A D band ($\sim 1360\text{ cm}^{-1}$) originates from the defects at the boundaries, such as edge plane site or doping, and a G band (1580 cm^{-1}) comes from sp^2 graphitic carbons. The disorder of the carbon material is determined by D/G, the ratio of area under D and G peaks.^{44–46} As Fig. 4 shows, there are no graphitic features or defect sites present in the PN-coating (Fig. 4A) or after microhotplate treatment (Fig. 4B), and only Si peaks, located at 522 cm^{-1} and 961 cm^{-1} , originating from the wafer are present.^{47–48} Therefore, no structural change to graphene was induced in the pre-annealing step. However, after treating PN with Nanoscribe laser writing, D and G peaks are present (Fig. 4C) which confirms the carbon structure as pyrolyzed PN. Defect sites were generated in the process of laser-induced graphitization.^{4,5} The D/G ratio is 2.70 is significantly higher than on the LIG-PN than CF (Fig. 4D), whose D/G ratio is 1.66 (Fig. 4E,

unpaired t-test, $n=6$, $p<0.0001$). Higher defect sites typically promote adsorption to the electrode surface of neurochemicals.⁴⁹ In Fig. 4F, the conductivity is demonstrated, as LIG-PN is applied in a gap in a platinum circuit, and the current-voltage response measured. . There is no response with either PN and HP-PN coated Pt circuits, shown in Fig. 5A and B, but the Nanoscribe laser induced graphitization of PN produces conductive material. The inverse of the slope in Fig. 4F, is the resistance of pyrolyzed PN. Fig. 5C shows the average resistance is 955 Ω . The calculated conductivity of LIG-PN is about 17,452 S/m, which is higher than previously reported RTP-PN (6 g), 3,200 S/m, and similar to glassy carbon 477-18,100 S/m.⁵⁰

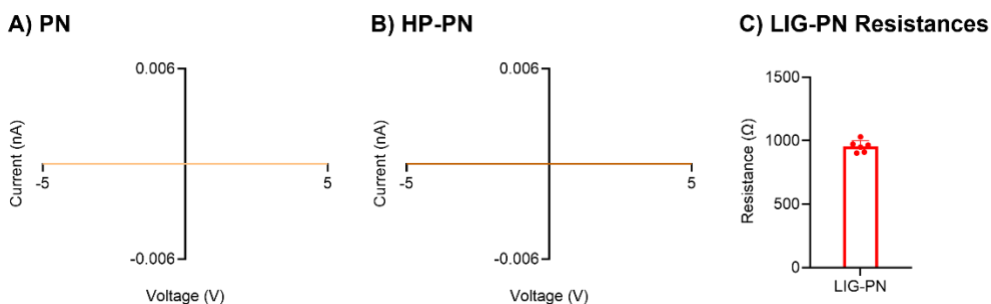


Figure 5. Conductivity tests of (A) PN and (B) HP-PN and (C) LIG-PN resistances

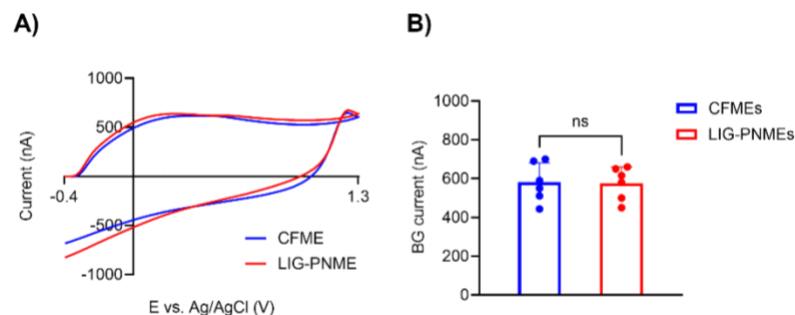


Figure 6. Background responses of CFMEs and LIG-PNME (A) Background CVs of CFME and LIG-PNME (B) Multiple background currents of CFMEs and LIG-PNMEs.

With laser-induced-graphitization of PN on Nb wires, we fabricated LIG-PN modified electrodes (LIG-PNMEs) and compared them to CFMEs for active surface areas. Fig. 6A shows that the background CVs of CFME and LIG-PNME are similar in shape and magnitude. Fig. 6B shows that the average background currents are not significantly different (unpaired t-test, $n=6$). Therefore, CF and LIG-PN have similar surface areas.

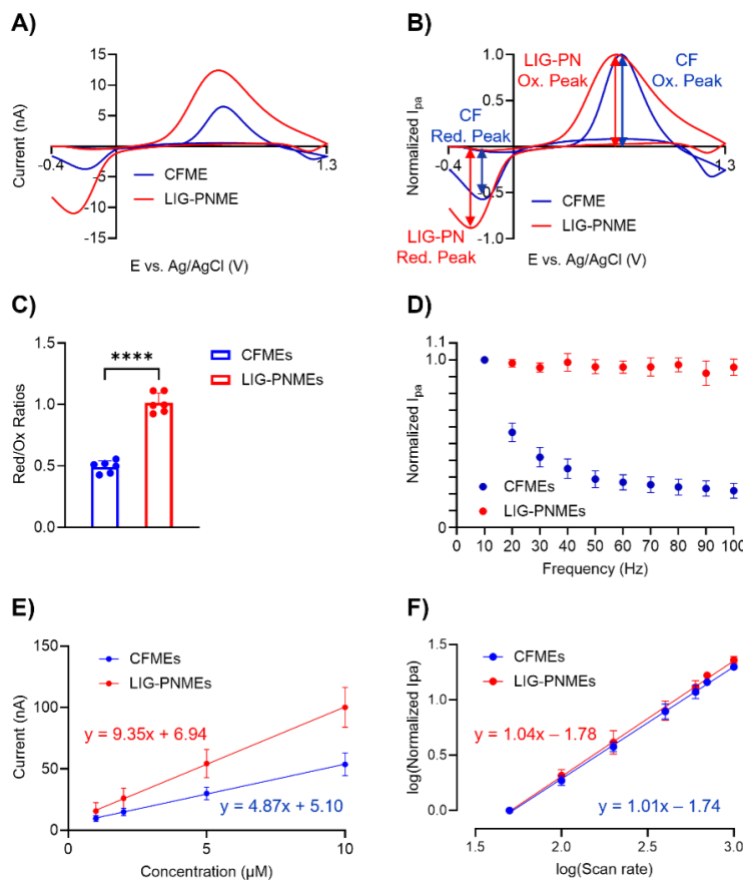


Figure 7. Electrochemical detection of DA at LIG-PN and CFMEs. (A) 1 μM DA CVs (B) Normalized DA CV graphs (C) Bar graph of ratios of reduction and oxidation peaks of 1 μM DA (unpaired t-test, n=6, ****p<0.0001) (D) Frequency tests of 1 μM DA (10-100 Hz) (n=6, Error bars are SEM) (E) DA sensitivity tests (1-10 μM) (n=6, Error bars are SEM) (F) Scan-rate tests (50-1000 V/s) (n=6, Error bars are SEM)

Fig. 7A shows CVs of 1 μM DA at CFME and LIG-PNME and the DA current response is higher at LIG-PNME. When normalizing the Faradaic currents of DA to background currents (Fig. 8A), the sensitivity for the LIG-PNMEs is significantly higher than CFMEs by about 1.50 times (unpaired t-test, p<0.01, n=6). Likely, the increased oxygen functional groups, shown in Fig. 9, and defect sites attract more DA on the surface.⁵¹⁻⁵³

Additionally, we observed the ratio of DA reduction peak to oxidation peak is close to 1 on LIG-PNME, shown in Fig. 7B, after normalizing CV graphs. However, the oxidation peak at CFME is 2-fold larger than the reduction peak as the adsorption coefficient of dopamine-o-quinone (DOQ) is smaller than DA.³⁷ Although oxidation and reduction potentials on LIG-PN shifted compared to CF, no major difference is expected between both ΔE_p.⁵⁴⁻⁵⁶ Fig. 7C shows

that the reduction-to-oxidation peak ratio for LIG-PMMEs is 1.01, while the average ratio at CFMEs is 0.49. More reversible CVs with a reduction-to-oxidation ratio of 1 have been observed in materials with a high surface roughness that momentarily traps dopamine on the timescale of the FSCV experiment.^{43,57-59} Thus, the rough surface of the LIG-PN could trap more dopamine molecules. To further confirm the trapping property of LIG-PNMEs, we performed frequency tests from 10 Hz to 100 Hz, on CFMEs and LIG-PNMEs. When the surface is smooth like CF, increasing frequency reduces the adsorption of DA onto the electrode surface as DA adsorption time is shortened and correspondingly lowers the detection sensitivity, which drops to 21.0% when the frequency is elevated to 100 Hz. However, LIG-PNMEs retained most sensitivity, 95.6%, at 100 Hz. Therefore, the rough surface of LIG-PN promotes the trapping of DA, which can be defined as nearly frequency-independent.

In Fig. 7E, various concentrations (1-10 μM) of DA were tested. The slopes of the concentration curves at LIG-PNMEs, 9.35, are higher than CFMEs, 4.87, for DA. In Fig. 7F, log (normalized I_{pa}) of DA on CFMEs and LIG-PPNMEs was plotted against the log (scan rate). If the slope is equal to 0.5, the detection is defined as diffusion controlled and if the slope is equal to 1, then detection is adsorption controlled.³⁷ The scan-rate slopes, 1.01 and 1.04, confirm that both electrodes are adsorption controlled.

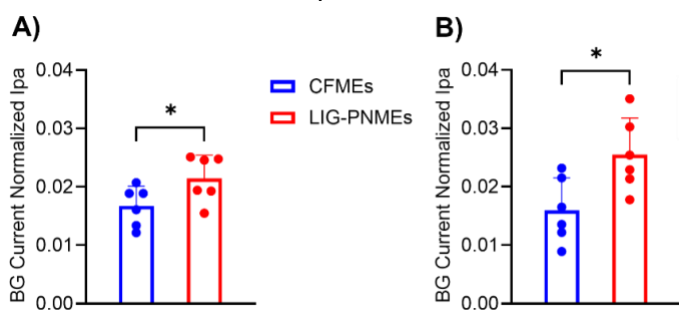


Figure 8. Background normalized currents of (A) 1 μM DA and (B) 1 μM 5-HT on CFMEs and LIG-PNMEs

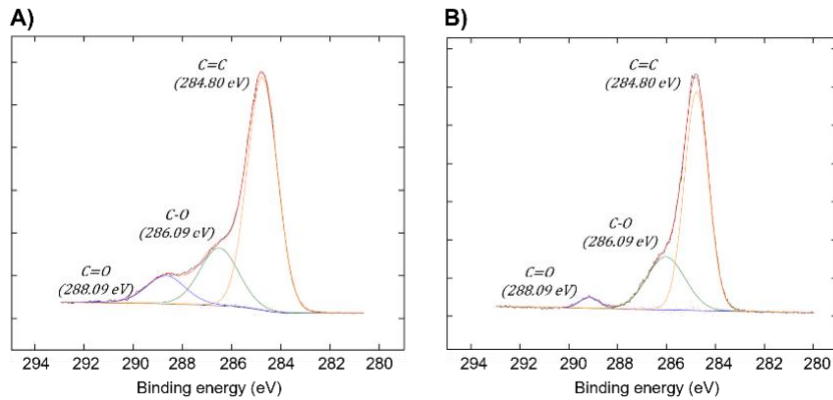


Figure 9. XPS spectra of (A) LIG-PN and (B) CF.

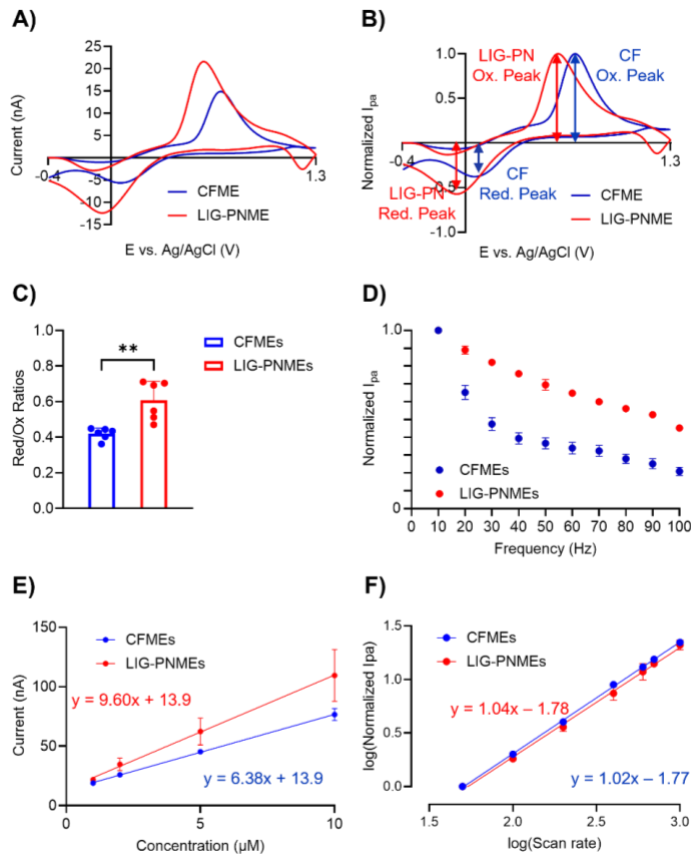


Figure 10. Electrochemical detection of Serotonin at LIG-PN and CFMEs. (A) 1 μM 5-HT CVs (B) Normalized 5-HT CV graphs (B) Bar graph of ratios of reduction and oxidation peaks of 1 μM 5-HT (unpaired t-test, $n=6$, $**p<0.01$) (D) Frequency tests of 1 μM 5-HT (10-100 Hz) ($n=6$, Error bars are SEM) (E) 5-HT sensitivity tests (1-10 μM) ($n=6$, Error bars are SEM) (F) Scan-rate tests (50-1000 V/s) ($n=6$, Error bars are SEM)

Serotonin CVs for CFME and LIG-PNME are shown in Fig. 10A and again the LIG-PNME has a higher current response. With background normalization (Fig. 8B), the 5-HT sensitivity of LIG-PN is about 1.3 times higher than CF, which means LIG-PN surface is more active for serotonin redox. After normalizing CVs, shown in Fig. 10B, normalized 5-HT reduction

peak height obtained on LIG-PN is larger than at CF and both ΔE_p are similar. Fig 10C shows reduction to oxidation at CFMEs and LIG-PNMEs of 0.60 and 0.42, respectively. Serotonin does not show as much of a reversible reaction, which may be due to the downstream polymerization reactions that occur after oxidation.^{39,60} In Fig. 10D, the frequency is raised from 10 Hz to 100 Hz and normalized 5-HT current responses are recorded and then plotted. For CFMEs, the signal dropped to 20% after reaching up to 100 Hz when LIG-PNMEs retained 45%. Even though LIG-PN could not induce 5-HT reduction to oxidation ratios as the same as DA, there are still more molecules that can be trapped onto the electrode surface compared to CF.

Sensitivity tests, 1-10 μM 5-HT, were also conducted on both types of electrodes, shown in Fig. 6E. The LIG-PN has a higher slope and higher sensitivity for serotonin detection. In Fig. 6F, the slopes of the log-log plots for scan rate are both close to 1, 1.04 and 1.02, which means that both detection types on the surface of CF and LIG-PN are adsorption-controlled. Generally, LIG-PNMEs could trap more target analytes than CFMEs because of a higher surface roughness.

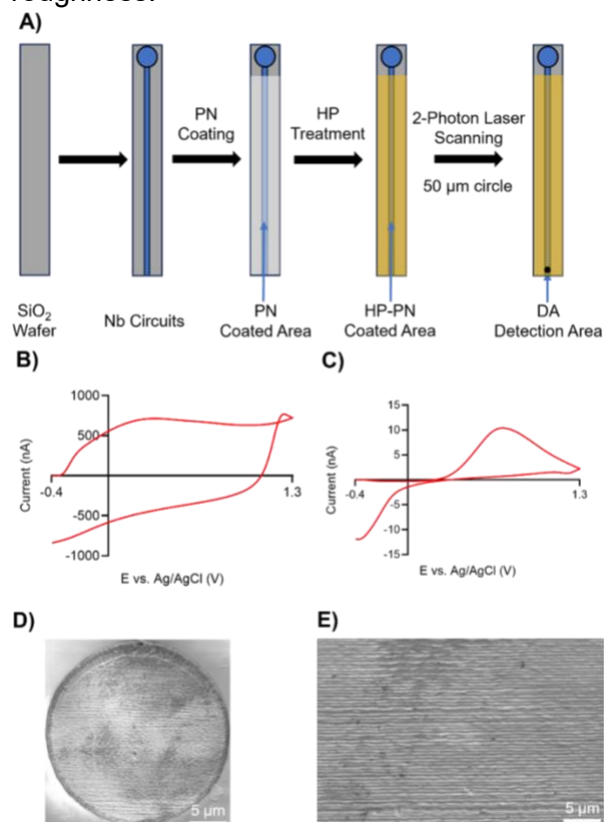


Figure 11. (A) MEMs chip development procedures (B) Background CV of LIG-PN on MEMs chip (C) CV of 1 μM DA on MEMs (D) SEM image of laser-scanned 50 μm circle (E) zoom-in view of laser-scanned circle

As LIG-PN possesses good electrochemical performance, we applied LIG-PN on microelectrochemical systems (MEMs). Fig. 11A illustrates the process of MEMs device development. The SiO_2 wafer was coated with 100 nm Nb to build a single-channel MEMs. The MEMs chip was coated with PN and then treated with microhotplate at 350°C for 10 min. The Nanoscribe laser was utilized to graphitize the selected area, a 50- μm circle. The background current is similar to the wires made of LIG-PN and is dependent on surface area. The LIG-PN MEMs chip was applied for 1 μM DA electrochemical detection, which is shown in Fig. 11C. We characterized the surface of laser-scanned circle for DA detection with SEM, which is shown in Fig. 11D. And then Fig. 11E showed a zoomed-in view of LIG-PN on single-channel MEMs chip to visualize the surface roughness, which helps induce the trapping of dopamine molecules. With the successful development of MEMs with LIG parylene, we could develop multiple-channel, 2, 4, or 6, MEMs chips for simultaneous detection of DA or other neurochemicals in the future.

One important consideration for *in vivo* testing microelectrodes is fouling, both electrochemical fouling and biofouling. Electrochemical fouling in this work originates from the polymerized 5-HT molecules when dopamine waveform was applied. 5-HT polymer can block the active surface area, which reduces the sites for absorbing analytes. Correspondingly, detection sensitivity, which is critical to neurochemical tracking, will majorly decrease. Because of richer defect sites and oxygen functional groups on LIG-PN than CF, it is assumed that LIG-PN will behave better than CF on preventing 5-HT polymer from attaching to the electrode surface. Therefore, 5-HT fouling experiments were conducted on both electrodes.

First, CFMEs and LIG-PNMEs were tested 30 times with 1 μM 5-HT. Multiple currents of 1st and 30th injections for CFME and LIG-PNME are respectively shown in Fig. 12A and B. On CF surface, 5-HT polymerized and covered the active sites, which lowered the sensitivity to

68.0%. However, on LIG-PN surface, less 5-HT polymer attached most sensitivity, 86.7%, was retained. Therefore, it is assumed that LIG-PN could resist the attachment of 5-HT polymer. To further confirm the assumption, long-term fouling experiments were conducted on CFMEs and LIG-PNMEs. Initially, PBS buffer was injected onto the electrode surface for 1hr and then recorded the current responses of 5-HT on CF and LIG-PN. At last, 1 μ M 5-HT solution was continuously injected for 1 hr. 5-HT currents responses were recorded and compared to the currents after 1-hr PBS injection, which are shown in Fig. 12C and D for CFMEs and LIG-PNMEs. It is observed that most active sites were blocked for CF, whose sensitivity reduced to 28.7%, while LIG-PN still got 73.7% sensitivity left. Therefore, it indicates that LIG-PN possesses anti-fouling property.

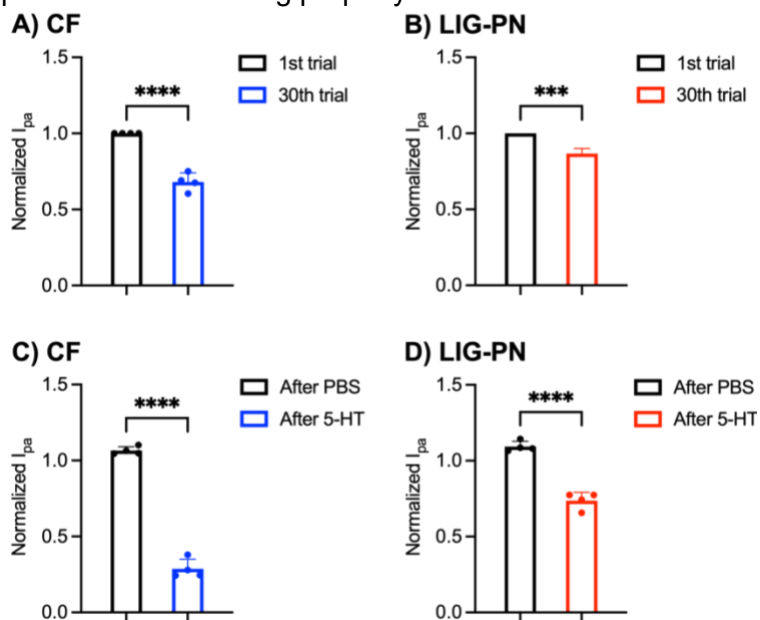


Figure 12. Fouling experiments with CFMEs and LIG-PNMEs. (A) Normalized I_{pa} of 1st and 30th injections of 1 μ M 5-HT on CFMEs (B) Normalized I_{pa} of 1st and 30th injections of 1 μ M 5-HT on LIG-PNMEs (C) Normalized I_{pa} after 1-hr PBS and after 1-hr 1 μ M 5-HT on CFMEs (D) Normalized I_{pa} after 1-hr PBS and after 1-hr 1 μ M 5-HT on LIG-PNMEs (unpaired t-test, n=4, ****p<0.0001, Error bars are SEM)

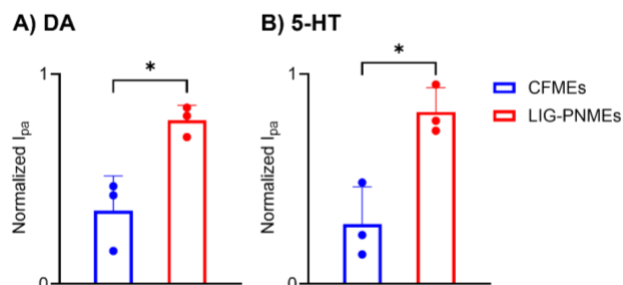


Figure 13. Biofouling experiments with rat brain tissue. Bar graphs of normalized currents of (A) 1 μ M DA and (B) 1 μ M 5HT for CFMEs and LIG-PNMEs after placing electrodes into the brain slice for 1 hr (unpaired t-test, n=3, *p<0.01, Error bars are SEM).

For testing if LIG-PN could resist biofouling, LIG-PNMEs were inserted into the brain slice with the application of dopamine waveform and kept for 1 hr and CFMEs were used as comparison. DA and 5-HT current responses, before and after CFME and LIG-PNME insertion into the brain slices, were respectively shown in Fig. 13. LIG-PNMEs retain most detection sensitivities, and it indicates that LIG-PN can prevent the attachment of protein or brain tissue. Both fouling and biofouling experiments, shown in Fig. 12 and 13, present that LIG-PNMEs possess a better performance on the prevention of 5-HT polymer and protein or brain tissue attachments.

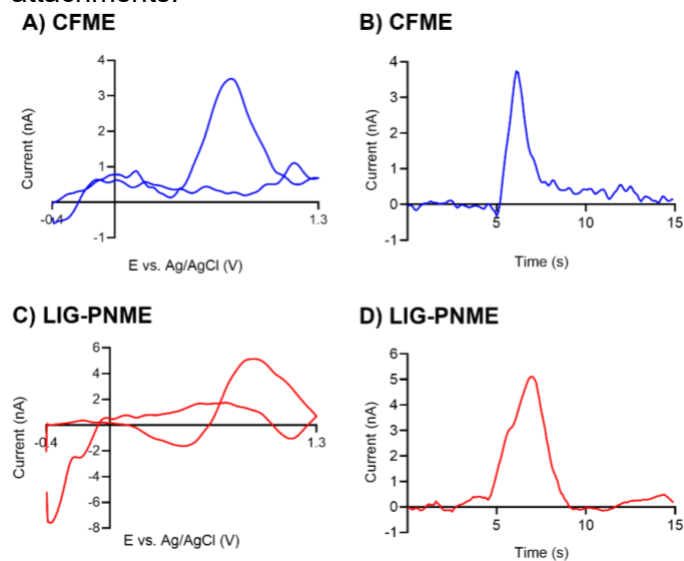


Figure 14 *In vivo* stimulated DA (A) Stimulated DA CV on CFME (B) DA IT curve on CFME (C) Stimulated DA CV on LIG-PNME (D) DA IT curve on LIG-PNME

Therefore, the fabricated electrode was applied *in vivo* to clarify their feasibility in tracking neurochemicals and compared to CFME. For dopamine, the mesolimbic circuit was evaluated by stimulating the ventral tegmental area (VTA) and measuring dopamine in the nucleus accumbens (NAc) of rats. CVs graphs of DA on CF and LIG-PN were shown in Fig. 14A and C respectively. LIG-PNME induced a much higher DA reduction peak than CFME, which nearly tracked no reduction signal. The *i* vs *t* curves in Fig. 14B and D present the peak currents increase with electrical stimulation, which indicates the release of dopamine. Biofouling or

possible background subtraction errors because of ionic changes can cause a bit wider *in vivo* CV.

4.3 Conclusions

Using a Nanoscribe printer to make LIG-PN electrodes allows a new method to make microelectrodes and MEMs devices for neurochemical detection. The size and geometry of the surface can be controlled by the design from the computer-aided system. Additionally, LIG-PN possesses a higher surface roughness than CFMEs, which promotes the trapping of neurochemicals, and behaves as nearly frequency-independent. and enabled LIG-PN to possess antifouling and anti-biofouling properties. Therefore, LIG-PNMEs are appropriately used for animal testing and successfully recorded *in vivo* dopamine and serotonin in *Drosophila*. MEMs chips with LIG-PN will enable new types of devices and arrays for electrochemical detection of neurotransmitters.

References

- (1) Kreuz, J. A.; Edman, J. R. Polyimide Films. *Adv. Mater.* **1998**, *10* (15), 1229–1232. [https://doi.org/10.1002/\(SICI\)1521-4095\(199810\)10:15<1229::AID-ADMA1229>3.0.CO;2-B](https://doi.org/10.1002/(SICI)1521-4095(199810)10:15<1229::AID-ADMA1229>3.0.CO;2-B).
- (2) Metz, S.; Holzer, R.; Renaud, P. Polyimide-Based Microfluidic Devices. *Lab. Chip* **2001**, *1* (1), 29. <https://doi.org/10.1039/b103896f>.
- (3) Rothman, L. B. Properties of Thin Polyimide Films. *J. Electrochem. Soc.* **1980**, *127* (10), 2216. <https://doi.org/10.1149/1.2129377>.
- (4) Lin, J.; Peng, Z.; Liu, Y.; Ruiz-Zepeda, F.; Ye, R.; Samuel, E. L. G.; Yacaman, M. J.; Yakobson, B. I.; Tour, J. M. Laser-Induced Porous Graphene Films from Commercial Polymers. *Nat. Commun.* **2014**, *5* (1), 5714. <https://doi.org/10.1038/ncomms6714>.
- (5) Ye, R.; James, D. K.; Tour, J. M. Laser-Induced Graphene. *Acc. Chem. Res.* **2018**, *51* (7), 1609–1620. <https://doi.org/10.1021/acs.accounts.8b00084>.
- (6) Ohara, K.; Nakashima, R.; Takahashi, H. Airflow Sensor Using Standing Laser-Induced Graphene Cantilevers. *IEEE Sens. J.* **2024**, *24* (7), 9585–9592. <https://doi.org/10.1109/JSEN.2024.3363671>.
- (7) Kulyk, B.; Silva, B. F. R.; Carvalho, A. F.; Barbosa, P.; Girão, A. V.; Deuermeier, J.; Fernandes, A. J. S.; Figueiredo, F. M. L.; Fortunato, E.; Costa, F. M. Laser-Induced Graphene from Paper by Ultraviolet Irradiation: Humidity and Temperature Sensors. *Adv. Mater. Technol.* **2022**, *7* (7), 2101311. <https://doi.org/10.1002/admt.202101311>.
- (8) Yuan, G.; Wan, T.; BaQais, A.; Mu, Y.; Cui, D.; Amin, M. A.; Li, X.; Xu, B. B.; Zhu, X.; Algadi, H.; Li, H.; Wasnik, P.; Lu, N.; Guo, Z.; Wei, H.; Cheng, B. Boron and Fluorine Co-Doped Laser-Induced Graphene towards High-Performance Micro-Supercapacitors. *Carbon* **2023**, *212*, 118101. <https://doi.org/10.1016/j.carbon.2023.118101>.
- (9) Rao, Y.; Yuan, M.; Luo, F.; Wang, Z.; Li, H.; Yu, J.; Chen, X. One-Step Laser Fabrication of Phosphorus-Doped Porous Graphene Electrodes for High-Performance Flexible Microsupercapacitor. *Carbon* **2021**, *180*, 56–66. <https://doi.org/10.1016/j.carbon.2021.05.001>.
- (10) Griesche, C.; Hoecherl, K.; Baeumner, A. J. Substrate-Independent Laser-Induced Graphene Electrodes for Microfluidic Electroanalytical Systems. *ACS Appl. Nano Mater.* **2021**, *4* (3), 3114–3121. <https://doi.org/10.1021/acsnm.1c00299>.
- (11) Nakashima, R.; Takahashi, H. Triaxial Tactile Sensor Utilizing Standing Laser-Induced Graphene Cantilevers on Polyimide Film. *Sens. Actuators Phys.* **2024**, *365*, 114919. <https://doi.org/10.1016/j.sna.2023.114919>.
- (12) Liu, S.; Chen, R.; Chen, R.; Jiang, C.; Zhang, C.; Chen, D.; Zhou, W.; Chen, S.; Luo, T. Facile and Cost-Effective Fabrication of Highly Sensitive, Fast-Response Flexible Humidity Sensors Enabled by Laser-Induced Graphene. *ACS Appl. Mater. Interfaces* **2023**, *acsami.3c12392*. <https://doi.org/10.1021/acsnm.1c00299>.
- (13) Zhang, H.; Wang, S.; Xu, Y. Study and Applications of a Parylene Self-Sealing Structure. In *19th IEEE International Conference on Micro Electro Mechanical Systems*; 2006; pp 282–285. <https://doi.org/10.1109/MEMSYS.2006.1627791>.
- (14) Correia, R.; Deuermeier, J.; Correia, M. R.; Vaz Pinto, J.; Coelho, J.; Fortunato, E.; Martins, R. Biocompatible Parylene-C Laser-Induced Graphene Electrodes for

Microsupercapacitor Applications. *ACS Appl. Mater. Interfaces* **2022**, *14* (41), 46427–46438. <https://doi.org/10.1021/acsami.2c09667>.

(15) Moon, H.; Ryu, B. Review of Laser-Induced Graphene (LIG) Produced on Eco-Friendly Substrates. *Int. J. Precis. Eng. Manuf.-Green Technol.* **2024**, *11* (4), 1279–1294. <https://doi.org/10.1007/s40684-024-00595-y>.

(16) Kim, B. J.; Meng, E. Micromachining of Parylene C for bioMEMS. *Polym. Adv. Technol.* **2016**, *27* (5), 564–576. <https://doi.org/10.1002/pat.3729>.

(17) Kuo, W.-C.; Wu, T.-C.; Wu, C.-F.; Wang, W.-C. Bioperformance Analysis of Parylene C Coating for Implanted Nickel Titanium Alloy. *Mater. Today Commun.* **2021**, *27*, 102306. <https://doi.org/10.1016/j.mtcomm.2021.102306>.

(18) Seymour, J. P.; Elkasabi, Y. M.; Chen, H.-Y.; Lahann, J.; Kipke, D. R. The Insulation Performance of Reactive Parylene Films in Implantable Electronic Devices. *Biomaterials* **2009**, *30* (31), 6158–6167. <https://doi.org/10.1016/j.biomaterials.2009.07.061>.

(19) Buchwalder, S.; Borzì, A.; Diaz Leon, J. J.; Bourgeois, F.; Nicolier, C.; Nicolay, S.; Neels, A.; Zywitzki, O.; Hogg, A.; Burger, J. Thermal Analysis of Parylene Thin Films for Barrier Layer Applications. *Polymers* **2022**, *14* (17), 3677. <https://doi.org/10.3390/polym14173677>.

(20) Gazicki-Lipman, M. Vapor Deposition Polymerization of Para-Xylylene Derivatives-Mechanism and Applications. *Shinku* **2007**, *50* (10), 601–608. <https://doi.org/10.3131/jvsj.50.601>.

(21) Kim, M. P.; Lee, G.; Noh, B.; Kim, J.; Kwak, M. S.; Lee, K. J.; Ko, H. Enhancing Energy Harvesting Performance of Bilayered Parylene Triboelectric Nanogenerators through Interfacial Polarization. *Nano Energy* **2024**, *119*, 109087. <https://doi.org/10.1016/j.nanoen.2023.109087>.

(22) Gorham, W. F. A New, General Synthetic Method for the Preparation of Linear Poly-p-Xylylenes. *J. Polym. Sci. [A1]* **1966**, *4* (12), 3027–3039. <https://doi.org/10.1002/pol.1966.150041209>.

(23) Fortin, J. B.; Lu, T.-M. A Model for the Chemical Vapor Deposition of Poly(Para - Xylylene) (Parylene) Thin Films. *Chem. Mater.* **2002**, *14* (5), 1945–1949. <https://doi.org/10.1021/cm010454a>.

(24) Gholizadeh, S.; Lincoln, D. M.; Allahyari, Z.; Widom, L. P.; Carter, R. N.; Gaborski, T. R. Optimization of Parylene C and Parylene N Thin Films for Use in Cellular Co-Culture and Tissue Barrier Models. *Sci. Rep.* **2023**, *13* (1), 4262. <https://doi.org/10.1038/s41598-023-31305-4>.

(25) Pruden, K. G.; Sinclair, K.; Beaudoin, S. Characterization of Parylene-N and Parylene-C Photooxidation. *J. Polym. Sci. Part Polym. Chem.* **2003**, *41* (10), 1486–1496. <https://doi.org/10.1002/pola.10681>.

(26) Hassler, C.; von Metzen, R. P.; Ruther, P.; Stieglitz, T. Characterization of Parylene C as an Encapsulation Material for Implanted Neural Prostheses. *J. Biomed. Mater. Res. B Appl. Biomater.* **2010**, *93B* (1), 266–274. <https://doi.org/10.1002/jbm.b.31584>.

(27) Chang, T. Y.; Yadav, V. G.; De Leo, S.; Mohedas, A.; Rajalingam, B.; Chen, C.-L.; Selvarasah, S.; Dokmeci, M. R.; Khademhosseini, A. Cell and Protein Compatibility of Parylene-C Surfaces. *Langmuir* **2007**, *23* (23), 11718–11725. <https://doi.org/10.1021/la7017049>.

- (28) Morton, K. C.; Morris, C. A.; Derylo, M. A.; Thakar, R.; Baker, L. A. Carbon Electrode Fabrication from Pyrolyzed Parylene c. *Anal. Chem.* **2011**, *83* (13), 5447–5452. <https://doi.org/10.1021/ac200885w>.
- (29) Wang, L.; Wang, Z.; Bakhtiyari, A. N.; Zheng, H. A Comparative Study of Laser-Induced Graphene by CO₂ Infrared Laser and 355 Nm Ultraviolet (UV) Laser. *Micromachines* **2020**, *11* (12), 1094. <https://doi.org/10.3390/mi11121094>.
- (30) Ye, R.; James, D. K.; Tour, J. M. Laser-Induced Graphene: From Discovery to Translation. *Adv. Mater.* **2019**, *31* (1), 1803621. <https://doi.org/10.1002/adma.201803621>.
- (31) Santos, N. F.; Pereira, S. O.; Moreira, A.; Girão, A. V.; Carvalho, A. F.; Fernandes, A. J. S.; Costa, F. M. IR and UV Laser-Induced Graphene: Application as Dopamine Electrochemical Sensors. *Adv. Mater. Technol.* **2021**, *6* (6), 2100007. <https://doi.org/10.1002/admt.202100007>.
- (32) Getachew, B. A.; Bergsman, D. S.; Grossman, J. C. Laser-Induced Graphene from Polyimide and Polyethersulfone Precursors as a Sensing Electrode in Anodic Stripping Voltammetry. *ACS Appl. Mater. Interfaces* **2020**, *12* (43), 48511–48517. <https://doi.org/10.1021/acsami.0c11725>.
- (33) Chang, Y.; Cao, Q.; Venton, B. J. 3D Printing for Customized Carbon Electrodes. *Curr. Opin. Electrochem.* **2023**, *38*, 101228. <https://doi.org/10.1016/j.coelec.2023.101228>.
- (34) Yang, C.; Cao, Q.; Puthongkham, P.; Lee, S. T.; Ganesana, M.; Lavrik, N. V.; Venton, B. J. 3D-Printed Carbon Electrodes for Neurotransmitter Detection. *Angew. Chem. Int. Ed.* **2018**, *57* (43), 14255–14259. <https://doi.org/10.1002/anie.201809992>.
- (35) Shao, Z.; Zhao, H.; Dunham, K. E.; Cao, Q.; Lavrik, N. V.; Venton, B. J. 3D-Printed Carbon Nanoneedle Electrodes for Dopamine Detection in *Drosophila*. *Angew. Chem.* **2024**, *136* (30), e202405634. <https://doi.org/10.1002/ange.202405634>.
- (36) Cao, Q.; Shin, M.; Lavrik, N. V.; Venton, B. J. 3D-Printed Carbon Nanoelectrodes for In Vivo Neurotransmitter Sensing. *Nano Lett.* **2020**, *20* (9), 6831–6836. <https://doi.org/10.1021/acs.nanolett.0c02844>.
- (37) *Fundamentals of fast-scan cyclic voltammetry for dopamine detection - Analyst (RSC Publishing)* DOI:10.1039/C9AN01586H. <https://pubs.rsc.org/en/content/articlehtml/2020/an/c9an01586h> (accessed 2022-09-18).
- (38) Zachek, M. K.; Hermans, A.; Wightman, R. M.; McCarty, G. S. Electrochemical Dopamine Detection: Comparing Gold and Carbon Fiber Microelectrodes Using Background Subtracted Fast Scan Cyclic Voltammetry. *J. Electroanal. Chem.* **2008**, *614* (1), 113–120. <https://doi.org/10.1016/j.jelechem.2007.11.007>.
- (39) Sarada, B. V.; Rao, T. N.; Tryk, D. A.; Fujishima, A. Electrochemical Oxidation of Histamine and Serotonin at Highly Boron-Doped Diamond Electrodes. *Anal. Chem.* **2000**, *72* (7), 1632–1638. <https://doi.org/10.1021/ac9908748>.
- (40) E. Dunham, K.; Jill Venton, B. Improving Serotonin Fast-Scan Cyclic Voltammetry Detection: New Waveforms to Reduce Electrode Fouling. *Analyst* **2020**, *145* (22), 7437–7446. <https://doi.org/10.1039/D0AN01406K>.
- (41) Zhao, H.; Shrestha, K.; Hensley, D. K.; Venton, B. J. Carbon Nanospikes Have Improved Sensitivity and Antifouling Properties for Adenosine, Hydrogen Peroxide, and Histamine. *Anal. Bioanal. Chem.* **2023**, *415* (24), 6039–6050. <https://doi.org/10.1007/s00216-023-04875-5>.

- (42) *The Rat Brain in Stereotaxic Coordinates*; 2006.
- (43) Shao, Z.; Puthongkham, P.; Hu, K.; Jia, R.; Mirkin, M. V.; Venton, B. J. Thin Layer Cell Behavior of CNT Yarn and Cavity Carbon Nanopipette Electrodes: Effect on Catecholamine Detection. *Electrochimica Acta* **2020**, *361*, 137032. <https://doi.org/10.1016/j.electacta.2020.137032>.
- (44) Dresselhaus, M. S.; Jorio, A.; Saito, R. Characterizing Graphene, Graphite, and Carbon Nanotubes by Raman Spectroscopy. *Annu. Rev. Condens. Matter Phys.* **2010**, *1* (Volume 1, 2010), 89–108. <https://doi.org/10.1146/annurev-conmatphys-070909-103919>.
- (45) Escribano, R.; Sloan, J. J.; Siddique, N.; Sze, N.; Dudev, T. Raman Spectroscopy of Carbon-Containing Particles. *Vib. Spectrosc.* **2001**, *26* (2), 179–186. [https://doi.org/10.1016/S0924-2031\(01\)00106-0](https://doi.org/10.1016/S0924-2031(01)00106-0).
- (46) Saito, R.; Hofmann, M.; Dresselhaus, G.; Jorio, A.; Dresselhaus, M. S. Raman Spectroscopy of Graphene and Carbon Nanotubes. *Adv. Phys.* **2011**, *60* (3), 413–550. <https://doi.org/10.1080/00018732.2011.582251>.
- (47) Piscanec, S.; Cantoro, M.; Ferrari, A. C.; Zapien, J. A.; Lifshitz, Y.; Lee, S. T.; Hofmann, S.; Robertson, J. Raman Spectroscopy of Silicon Nanowires. *Phys. Rev. B* **2003**, *68* (24), 241312. <https://doi.org/10.1103/PhysRevB.68.241312>.
- (48) Liger, M.; Harder, T. A.; Tai, Y.-C.; Konishi, S. Parylene-Pyrolyzed Carbon for MEMS Applications. In *17th IEEE International Conference on Micro Electro Mechanical Systems. Maastricht MEMS 2004 Technical Digest*; 2004; pp 161–164. <https://doi.org/10.1109/MEMS.2004.1290547>.
- (49) Cao, Q.; Hensley, D. K.; Lavrik, N. V.; Venton, B. J. Carbon Nanospikes Have Better Electrochemical Properties than Carbon Nanotubes Due to Greater Surface Roughness and Defect Sites. *Carbon* **2019**, *155*, 250–257. <https://doi.org/10.1016/j.carbon.2019.08.064>.
- (50) Ferrer, L.; Shamloo, E.; Cisquella Serra, A.; Salazar, A.; Madou, M.; Lee, J. Size-Dependent Electrical and Thermal Conductivities of Electro-Mechanically-Spun Glassy Carbon Wires. *Carbon* **2017**, *130*. <https://doi.org/10.1016/j.carbon.2017.12.113>.
- (51) Jacobs, C. B.; Vickrey, T. L.; Venton, B. J. Functional Groups Modulate the Sensitivity and Electron Transfer Kinetics of Neurochemicals at Carbon Nanotube Modified Microelectrodes. *The Analyst* **2011**, *136* (17), 3557. <https://doi.org/10.1039/c0an00854k>.
- (52) Roberts, J. G.; Moody, B. P.; McCarty, G. S.; Sombers, L. A. Specific Oxygen-Containing Functional Groups on the Carbon Surface Underlie an Enhanced Sensitivity to Dopamine at Electrochemically Pretreated Carbon Fiber Microelectrodes. *Langmuir* **2010**, *26* (11), 9116–9122. <https://doi.org/10.1021/la9048924>.
- (53) Behan, J. A.; Grajkowski, F.; Jayasundara, D. R.; Vilella-Arribas, L.; García-Melchor, M.; Colavita, P. E. Influence of Carbon Nanostructure and Oxygen Moieties on Dopamine Adsorption and Charge Transfer Kinetics at Glassy Carbon Surfaces. *Electrochimica Acta* **2019**, *304*, 221–230. <https://doi.org/10.1016/j.electacta.2019.02.103>.
- (54) Hočevár, S. B.; Wang, J.; Deo, R. P.; Musameh, M.; Ogorevc, B. Carbon Nanotube Modified Microelectrode for Enhanced Voltammetric Detection of Dopamine in the Presence of Ascorbate. *Electroanalysis* **2005**, *17* (5–6), 417–422. <https://doi.org/10.1002/elan.200403175>.

- (55) Mendoza, A.; Asrat, T.; Liu, F.; Wonnenberg, P.; Zestos, A. G. Carbon Nanotube Yarn Microelectrodes Promote High Temporal Measurements of Serotonin Using Fast Scan Cyclic Voltammetry. *Sensors* **2020**, *20* (4), 1173. <https://doi.org/10.3390/s20041173>.
- (56) Schmidt, A. C.; Wang, X.; Zhu, Y.; Sombers, L. A. Carbon Nanotube Yarn Electrodes for Enhanced Detection of Neurotransmitter Dynamics in Live Brain Tissue. *ACS Nano* **2013**, *7* (9), 7864–7873. <https://doi.org/10.1021/nn402857u>.
- (57) Jacobs, C. B.; Ivanov, I. N.; Nguyen, M. D.; Zestos, A. G.; Venton, B. J. High Temporal Resolution Measurements of Dopamine with Carbon Nanotube Yarn Microelectrodes. *Anal. Chem.* **2014**, *86* (12), 5721–5727. <https://doi.org/10.1021/ac404050t>.
- (58) Shao, Z.; Chang, Y.; Venton, B. J. Carbon Microelectrodes with Customized Shapes for Neurotransmitter Detection: A Review. *Anal. Chim. Acta* **2022**, *1223*, 340165. <https://doi.org/10.1016/j.aca.2022.340165>.
- (59) Yang, C.; Hu, K.; Wang, D.; Zubi, Y.; Lee, S. T.; Puthongkham, P.; Mirkin, M. V.; Venton, B. J. Cavity Carbon-Nanopipette Electrodes for Dopamine Detection. *Anal. Chem.* **2019**, *91* (7), 4618–4625. <https://doi.org/10.1021/acs.analchem.8b05885>.
- (60) Dunham, K. E.; Venton, B. J. Improving Serotonin Fast-Scan Cyclic Voltammetry Detection: New Waveforms to Reduce Electrode Fouling. *Analyst* **2020**, *145* (22), 7437–7446. <https://doi.org/10.1039/D0AN01406K>.

Chapter 5

Conclusions and Future Directions

5.1. Contribution of the Dissertation to the Field

5.1.1 Customizable Micro/nano Carbon Sensors

Traditional implantable microelectrodes, CFMEs, facilitate electrochemical detection in the field of neuroscience. However, there are limited fabrication methods for carbon sensors. This thesis investigates methods to fabricate modified electrodes and their applications for *in vivo* neurochemical recording and prevention of fouling and biofouling. Chapters 2-4 clarify ways to achieve nanoscale carbon electrodes. Chapter 2 demonstrates that carbon nanospikes can be deposited on Nb wires with PECVD and then utilized as sensors to test high-potential analytes and applied for puff-on testing in the brain slice. High surface roughness and rich carboxyl groups of nanospikes prevent fouling and biofouling and retain the most sensitivities. Nanolayers of pyrolyzed PN, shown in Chapter 3, were achieved with RTP after undergoing volumetric loss and structural reformation from insulative polymer to conductive graphite. Thus, pyrolyzed PN with RTP is suitable for the electrochemical characterization of neurotransmitters and further *in vivo* tracking. Chapter 4 presents an alternative method to achieve laser-induced-graphene (LIG) from PN instead of PI, with a Nanoscribe laser, which is commonly used for micro/nano 3D printing. LIG-PN possesses good electrochemical performance. We found that pre-heating PN at 350 °C, which changes the absorption property, is essential for the Nanoscribe laser to make LIG from PN. The key point of LIG-PN is that the spatial feature resolution is about 0.75 to 1.50 μm , which makes it feasible for the fabrication of modified electrodes and MEMs devices.

5.1.2 Single-channel MEMs with LIG-PN

The potential of LIG-PN for neurochemical detection is further demonstrated in Chapter 4, which is integrated into a single-channel MEMs chip for dopamine (DA) detection. Therefore, this proof-of-concept suggests scalability toward multiple-channel MEMs chips (e.g., 2, 4, or 6

electrodes) coated with PN and pyrolyzed using a Nanoscribe laser. Such systems could enable the simultaneous detection of multiple neurotransmitters.

The principal contribution of this work lies in developing novel carbon electrode fabrication methods that broaden the scope of neurochemical sensing applications. CNSs investigated in Chapter 2 provide a direction for electrodes that can be used for a stable and long-term *in vivo* neurochemical recording with the most sensitivity retained and prevention of brain tissue or protein attachments. Their high surface roughness and rich oxygen functional groups facilitate the adsorption of both positively charged catecholamines and neutral species, like H₂O₂. Chapter 3 reveals that insulative polymers, parylene, can be thermally converted into conductive graphite, suggesting further exploration of polymer types and geometries for electrode design. While nanolayers of graphite, 194 nm, offer excellent electrochemical performance, 81 nm for graphite thickness generates an extremely high resistance and compromises electrochemical detection. Lastly, Chapter 4 introduces the novel use of a commercially available Nanoscribe printed-commonly employed for photoresist crosslinking-to graphitize solid-state PN. The LIG-PN electrodes are initially demonstrated in a single-channel MEMs chip for neurochemical detection with FSCV, opening pathways for detecting both electroactive and non-electroactive neurotransmitters. Multiple-channel MEMs chips can also be developed to achieve co-detection of various analytes. Thus, the methodology supports future designs of customizable, multi-analyte electrode arrays.

5.2 Challenges and Future Directions

5.2.1 *Synaptic recording with 3D-Printing*

To elucidate the fundamental mechanism of neurochemical communication, it is crucial to develop sensors capable of recording neurotransmitter release at the synaptic level.¹⁻³ In this way, we could determine the neurotransmitter communication at the synapse.⁴⁻⁷ If synapses are not functional, it leads to neurodegenerative disorders, such as Parkinson's or Alzheimer's

disease, and synapses in diseased brains could be examined with 3D-printed nanoelectrodes.⁸⁻

¹¹ However, current 3D printing fabrication methods can obtain micro/nanotips, but the smallest fabricated carbon tip from the most recent method is about 600 nm, which is not feasible for neurochemical tracking in synapses, whose sizes are about 20-40 nm.¹²⁻¹⁴ Therefore, a key future direction involves engineering 3D-printed nanoelectrodes with tip sizes that approach the synaptic scale, allowing precise detection without inflicting damage to the neural architecture.

5.2.2 Shrinking 3D-Printing with Oxygen Plasma Etching

Current 3D-printed models are fabricated on Nb wires using photoresists, such as IP-DIP, or IP-S, and subsequently developed with SU-8 developer. Post-printing, 3D-printed models are exposed to UV light to further induce the crosslinking of photoresist. 350 °C is applied on the micro hotplate to pre-anneal 3D printings and causes the overall size to shrink. A rapid thermal processor (RTP) is utilized to pyrolyze the structures, which are transformed into glassy carbon and will shrink due to weight loss.¹⁵⁻¹⁸ The resulting carbon tip ranges from nanoscale to microscale. All fabricated micro/nanotips can be used to track neurochemical releases in models such as rat or *Drosophila* brains.^{13,14} However, further miniaturization is still needed to further shrink the tip size of 3D printing to match synaptic dimensions. Oxygen plasma etching is a promising technique to achieve this scale, representing a critical step in advancing precision neurochemical detection.

Oxygen plasma is a technique that introduces oxygen gas into a high-energy environment and then oxygen is ionized with high-frequency radio or other resources under vacuum. The ionized oxygen can be used for modifying, cleaning, and etching material surfaces.^{19–22} In this context, we expect oxygen plasma etching to further shrink the tips of 3D-printed carbon structures, bringing them closer to, or even smaller than synapses.

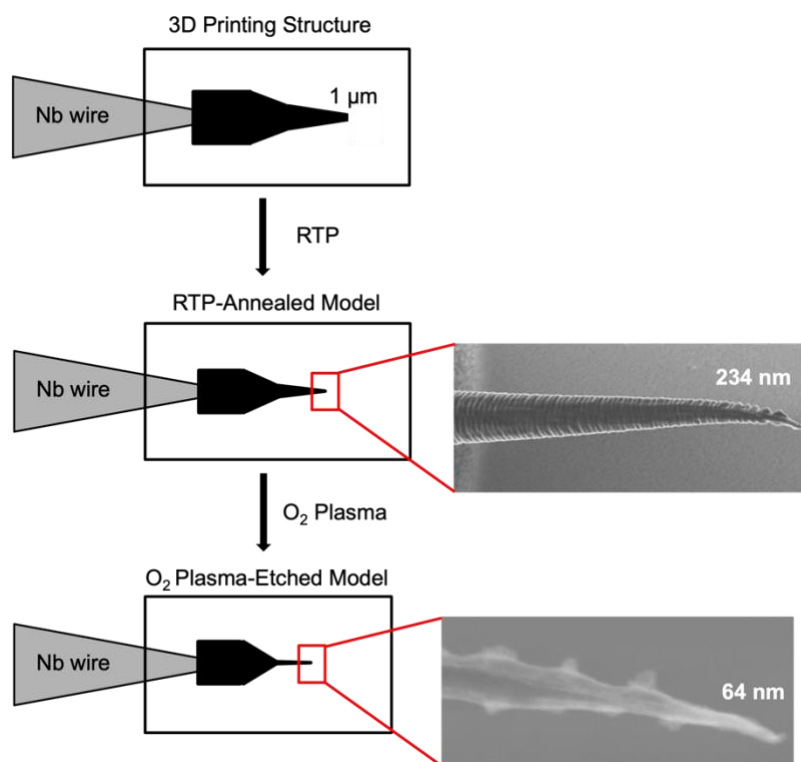


Figure. 5.1 Schematic view of shrunk 3D-printed model by oxygen plasma. The bottom shows sub 100 nm electrodes can be achieved.

5.2.3 Co-detection of Dopamine and Glutamate

Some neurochemicals cannot be oxidized and/or reduced to enable detection. Glutamate, an abundant neurotransmitter mostly distributed in the central nervous system, is non-electroactive.^{23,24} To enable electrochemical detection of glutamate, the enzyme, glutamate oxidase is applied to the electrode, which generates hydrogen peroxide (H₂O₂), which can be electrochemically oxidized.^{25,26} This type of biosensor can be utilized on microelectromechanical systems (MEMS) devices. Silicon nitride (SiN_x) and silicon oxide (SiO_x) are commonly used for the development of cantilevers. Atomic force microscopy (AFM) microelectromechanical

systems (MEMs) devices make wide use of cantilevers.^{27–29} Si-based sensors, shown in Fig. 5.2, are designed for neurochemical detection as well as the species that are not electroactive, such as glutamate. For electrochemical sensors, the working area can be printed with 3D-printed structures. Therefore, high sensitivity can be provided with a carbon sensor. The biocompatibility of carbon sensors also enables sensitive *in vivo* monitoring. On glutamate biosensors, glutamate oxidase will be deposited. With the presence of oxygen, glutamate reacts with glutamate oxidase to produce hydrogen peroxide (H₂O₂), which can be electrochemically detected.^{30,31} The combination of direct electrochemical and glutamate biosensors would enable dual detection of neurochemicals and glutamate. There are many options for the carbon sensor part: (1) carbon nanomaterials (2) pyrolyzed parylene-N with RTP (3) laser-induced-graphene from parylene-N with Nanoscribe laser (4) Trapping 3D-printing electrodes. Multiple-channel MEMs can also be utilized in further co-detection.

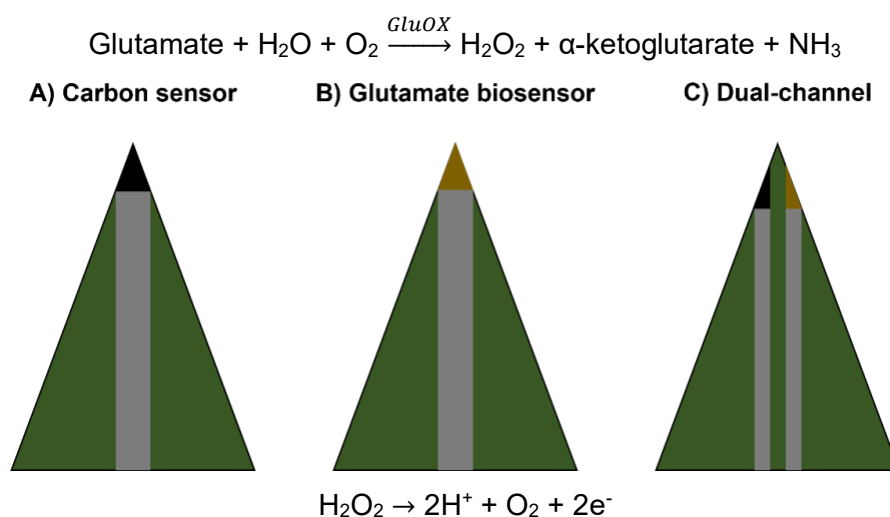


Figure 5.2. Schematic illustration of neurochemical, glutamate, and dual-channel sensors

5.3 Final Remarks

In summary, this dissertation investigates multiple fabrication methods for carbon electrode sensors, emphasizing the creation of novel geometries and surfaces that exhibit high resistance to fouling and biofouling due to high surface roughness, rich defect sites, and oxygen functional groups. Chapter 2 demonstrates a deposition method of carbon nanospikes on Nb wires by PECVD. CNSMEs can be applied to track neurotransmitters in brain slices while retaining high sensitivity. Therefore, CNSMEs can be further utilized for *in vivo* tracking. Chapter 3 presents a method of transforming insulative polymer, deposited by CVD, into conductive graphite via RTP. High temperatures (up to 950 °C) provide enough energy for PN to undergo structural reformation into graphene. Pyrolyzed PN possesses good electrochemical performance and can track stimulated DA and spontaneous AD *in vivo*. An alternative method to fabricate laser-induced-graphene is clarified in Chapter 4. CVD deposits PN on the substrate, and a Nanoscribe two-photon lithography printer is applied to the PN surface to induce graphitization. LIG originating from PN presents an extremely high surface roughness and favors the trapping of target analytes. Both *in vivo* DA and puff-on 5-HT prove that LIG-PNMEs are appropriately used for neurochemical tracking. Therefore, these modified electrode sensors originating from new fabrication methods could be used to record released neurotransmitters in animal models and study neurodegenerative disorders.

References

- (1) Grinvald, A.; Salzberg, B. M.; Lev-Ram, V.; Hildesheim, R. Optical Recording of Synaptic Potentials from Processes of Single Neurons Using Intracellular Potentiometric Dyes. *Biophys. J.* **1987**, *51* (4), 643–651. [https://doi.org/10.1016/S0006-3495\(87\)83389-1](https://doi.org/10.1016/S0006-3495(87)83389-1).
- (2) Trussell, L. O. SYNAPTIC MECHANISMS FOR CODING TIMING IN AUDITORY NEURONS. *Annu. Rev. Physiol.* **1999**, *61* (1), 477–496. <https://doi.org/10.1146/annurev.physiol.61.1.477>.
- (3) Moore, G. P.; Segundo, J. P.; Perkel, D. H.; Levitan, H. Statistical Signs of Synaptic Interaction in Neurons. *Biophys. J.* **1970**, *10* (9), 876–900. [https://doi.org/10.1016/S0006-3495\(70\)86341-X](https://doi.org/10.1016/S0006-3495(70)86341-X).
- (4) Indiveri, G.; Liu, S.-C. Memory and Information Processing in Neuromorphic Systems. *Proc. IEEE* **2015**, *103* (8), 1379–1397. <https://doi.org/10.1109/JPROC.2015.2444094>.
- (5) Markram, H.; Gupta, A.; Uziel, A.; Wang, Y.; Tsodyks, M. Information Processing with Frequency-Dependent Synaptic Connections. *Neurobiol. Learn. Mem.* **1998**, *70* (1), 101–112. <https://doi.org/10.1006/nlme.1998.3841>.
- (6) Wu, G. K.; Tao, H. W.; Zhang, L. I. From Elementary Synaptic Circuits to Information Processing in Primary Auditory Cortex. *Neurosci. Biobehav. Rev.* **2011**, *35* (10), 2094–2104. <https://doi.org/10.1016/j.neubiorev.2011.05.004>.
- (7) Koch, C.; Segev, I. The Role of Single Neurons in Information Processing. *Nat. Neurosci.* **2000**, *3* (S11), 1171–1177. <https://doi.org/10.1038/81444>.
- (8) Tang, J.; Oliveros, A.; Jang, M.-H. Dysfunctional Mitochondrial Bioenergetics and Synaptic Degeneration in Alzheimer Disease. *Int. Neurol. J.* **2019**, *23* (Suppl 1), S5-10. <https://doi.org/10.5213/inj.1938036.018>.
- (9) Bellucci, A.; Mercuri, N. B.; Venneri, A.; Faustini, G.; Longhena, F.; Pizzi, M.; Missale, C.; Spano, P. Review: Parkinson's Disease: From Synaptic Loss to Connectome Dysfunction. *Neuropathol. Appl. Neurobiol.* **2016**, *42* (1), 77–94. <https://doi.org/10.1111/nan.12297>.
- (10) Holmes, S. E.; Honhar, P.; Tinaz, S.; Naganawa, M.; Hilmer, A. T.; Gallezot, J.-D.; Dias, M.; Yang, Y.; Toyonaga, T.; Esterlis, I.; Mecca, A.; Van Dyck, C.; Henry, S.; Ropchan, J.; Nabulsi, N.; Louis, E. D.; Comley, R.; Finnema, S. J.; Carson, R. E.; Matuskey, D. Synaptic Loss and Its Association with Symptom Severity in Parkinson's Disease. *Npj Park. Dis.* **2024**, *10* (1), 1–9. <https://doi.org/10.1038/s41531-024-00655-9>.
- (11) Tzioras, M.; McGeachan, R. I.; Durrant, C. S.; Spires-Jones, T. L. Synaptic Degeneration in Alzheimer Disease. *Nat. Rev. Neurol.* **2023**, *19* (1), 19–38. <https://doi.org/10.1038/s41582-022-00749-z>.
- (12) Yang, C.; Cao, Q.; Puthongkham, P.; Lee, S. T.; Ganesana, M.; Lavrik, N. V.; Venton, B. J. 3D-Printed Carbon Electrodes for Neurotransmitter Detection. *Angew. Chem. Int. Ed.* **2018**, *57* (43), 14255–14259. <https://doi.org/10.1002/anie.201809992>.
- (13) Cao, Q.; Shin, M.; Lavrik, N. V.; Venton, B. J. 3D-Printed Carbon Nanoelectrodes for In Vivo Neurotransmitter Sensing. *Nano Lett.* **2020**, *20* (9), 6831–6836. <https://doi.org/10.1021/acs.nanolett.0c02844>.
- (14) Shao, Z.; Zhao, H.; Dunham, K. E.; Cao, Q.; Lavrik, N. V.; Venton, B. J. 3D-Printed Carbon Nanoneedle Electrodes for Dopamine Detection in *Drosophila*. *Angew. Chem.* **2024**, *136* (30), e202405634. <https://doi.org/10.1002/ange.202405634>.

- (15) Cardenas-Benitez, B.; Eschenbaum, C.; Mager, D.; Korvink, J. G.; Madou, M. J.; Lemmer, U.; Leon, I. D.; Martinez-Chapa, S. O. Pyrolysis-Induced Shrinking of Three-Dimensional Structures Fabricated by Two-Photon Polymerization: Experiment and Theoretical Model. *Microsyst. Nanoeng.* **2019**, *5* (1), 1–13. <https://doi.org/10.1038/s41378-019-0079-9>.
- (16) Sharipova, M. I.; Baluyan, T. G.; Abrashitova, K. A.; Kulagin, G. E.; Petrov, A. K.; Chizhov, A. S.; Shatalova, T. B.; Chubich, D.; Kolymagin, D. A.; Vitukhnovsky, A. G.; Bessonov, V. O.; Fedyanin, A. A. Effect of Pyrolysis on Microstructures Made of Various Photoresists by Two-Photon Polymerization: Comparative Study. *Opt. Mater. Express* **2021**, *11* (2), 371–384. <https://doi.org/10.1364/OME.416457>.
- (17) Abaddi, M. A.; Sasso, L.; Dimaki, M.; Svendsen, W. E. Fabrication of 3D Nano/Microelectrodes via Two-Photon-Polymerization. *Microelectron. Eng.* **2012**, *98*, 378–381. <https://doi.org/10.1016/j.mee.2012.07.015>.
- (18) Yi, W.; Yang, Y.; Hashemi, P.; Cheng, M. M.-C. 3D Carbon Nanofiber Microelectrode Arrays Fabricated by Plasma-Assisted Pyrolysis to Enhance Sensitivity and Stability of Real-Time Dopamine Detection. *Biomed. Microdevices* **2016**, *18* (6), 112. <https://doi.org/10.1007/s10544-016-0136-1>.
- (19) García, A. B.; Martínez-Alonso, A.; Leon y Leon, C. A.; Tascón, J. M. D. Modification of the Surface Properties of an Activated Carbon by Oxygen Plasma Treatment. *Fuel* **1998**, *77* (6), 613–624. [https://doi.org/10.1016/S0016-2361\(97\)00111-7](https://doi.org/10.1016/S0016-2361(97)00111-7).
- (20) Wu, G. M. Oxygen Plasma Treatment of High Performance Fibers for Composites. *Mater. Chem. Phys.* **2004**, *85* (1), 81–87. <https://doi.org/10.1016/j.matchemphys.2003.12.004>.
- (21) Hartney, M. A.; Hess, D. W.; Soane, D. S. Oxygen Plasma Etching for Resist Stripping and Multilayer Lithography. *J. Vac. Sci. Technol. B Microelectron. Process. Phenom.* **1989**, *7* (1), 1–13. <https://doi.org/10.1116/1.584440>.
- (22) Gokus, T.; Nair, R. R.; Bonetti, A.; Böhmeler, M.; Lombardo, A.; Novoselov, K. S.; Geim, A. K.; Ferrari, A. C.; Hartschuh, A. Making Graphene Luminescent by Oxygen Plasma Treatment. *ACS Nano* **2009**, *3* (12), 3963–3968. <https://doi.org/10.1021/nn9012753>.
- (23) Sano, C. History of Glutamate Production. *Am. J. Clin. Nutr.* **2009**, *90* (3), 728S–732S. <https://doi.org/10.3945/ajcn.2009.27462F>.
- (24) Vandenberg, R. J.; Ryan, R. M. Mechanisms of Glutamate Transport. *Physiol. Rev.* **2013**, *93* (4), 1621–1657. <https://doi.org/10.1152/physrev.00007.2013>.
- (25) Ryan, M. R.; Lowry, J. P.; O'Neill, R. D. Biosensor for Neurotransmitter L-Glutamic Acid Designed for Efficient Use of L-Glutamate Oxidase and Effective Rejection of Interference. *The Analyst* **1997**, *122* (11), 1419–1424. <https://doi.org/10.1039/a704508e>.
- (26) Kimble, L. C.; Twiddy, J. S.; Berger, J. M.; Forderhase, A. G.; McCarty, G. S.; Meitzen, J.; Sombers, L. A. Simultaneous, Real-Time Detection of Glutamate and Dopamine in Rat Striatum Using Fast-Scan Cyclic Voltammetry. *ACS Sens.* **2023**, *8* (11), 4091–4100. <https://doi.org/10.1021/acssensors.3c01267>.
- (27) Alvarez, M.; Zinoviev, K.; Moreno, M.; Lechuga, L. M. CANTILEVER BIOSENSORS. *Opt. Biosens.* **2008**, 419–452. <https://doi.org/10.1016/B978-044453125-4.50012-7>.
- (28) Basu, A. K.; Basu, A.; Bhattacharya, S. Micro/Nano Fabricated Cantilever Based Biosensor Platform: A Review and Recent Progress. *Enzyme Microb. Technol.* **2020**, *139*, 109558. <https://doi.org/10.1016/j.enzmictec.2020.109558>.

- (29) Boisen, A.; Thundat, T. Design & Fabrication of Cantilever Array Biosensors. *Mater. Today* **2009**, *12* (9), 32–38. [https://doi.org/10.1016/S1369-7021\(09\)70249-4](https://doi.org/10.1016/S1369-7021(09)70249-4).
- (30) Soldatkina, O. V.; Soldatkin, O. O.; Kasap, B. O.; Kucherenko, D. Yu.; Kucherenko, I. S.; Kurc, B. A.; Dzyadevych, S. V. A Novel Amperometric Glutamate Biosensor Based on Glutamate Oxidase Adsorbed on Silicalite. *Nanoscale Res. Lett.* **2017**, *12* (1), 260. <https://doi.org/10.1186/s11671-017-2026-8>.
- (31) Özel, R. E.; Ispas, C.; Ganesana, M.; Leiter, J. C.; Andreescu, S. Glutamate Oxidase Biosensor Based on Mixed Ceria and Titania Nanoparticles for the Detection of Glutamate in Hypoxic Environments. *Biosens. Bioelectron.* **2014**, *52*, 10.1016/j.bios.2013.08.054. <https://doi.org/10.1016/j.bios.2013.08.054>.

Appendix

- (1) **Zhao, H.**; Shrestha, K.; Hensley, D. K.; Venton, B. J. Carbon Nanospikes Have Improved Sensitivity and Antifouling Properties for Adenosine, Hydrogen Peroxide, and Histamine. *Anal. Bioanal. Chem.* 2023, 415 (24), 6039–6050. <https://doi.org/10.1007/s00216-023-04875-5>.
- (2) Hanser, S. M.; Shao, Z.; **Zhao, H.**; Venton, B. J. Electrochemical Treatment in KOH Improves Carbon Nanomaterial Performance to Multiple Neurochemicals. *The Analyst* 2023, 149 (2), 457–466. <https://doi.org/10.1039/d3an01710a>.
- (3) Shao, Z.; **Zhao, H.**; Dunham, K. E.; Cao, Q.; Lavrik, N. V.; Venton, B. J. 3D-Printed Carbon Nanoneedle Electrodes for Dopamine Detection in *Drosophila*. *Angewandte Chemie* 2024, 136 (30). <https://doi.org/10.1002/ange.202405634>.
- (4) **Zhao, H.**; Markow, O.; Greatness Olaitan; Donarski, E. D.; Lester, K. C.; Lavrik, N. V.; Venton, B. J. Pyrolyzed Parylene-N for *in Vivo* Electrochemical Detection of Neurotransmitters. *ACS electrochemistry*. 2025. <https://doi.org/10.1021/acselectrochem.4c00180>.